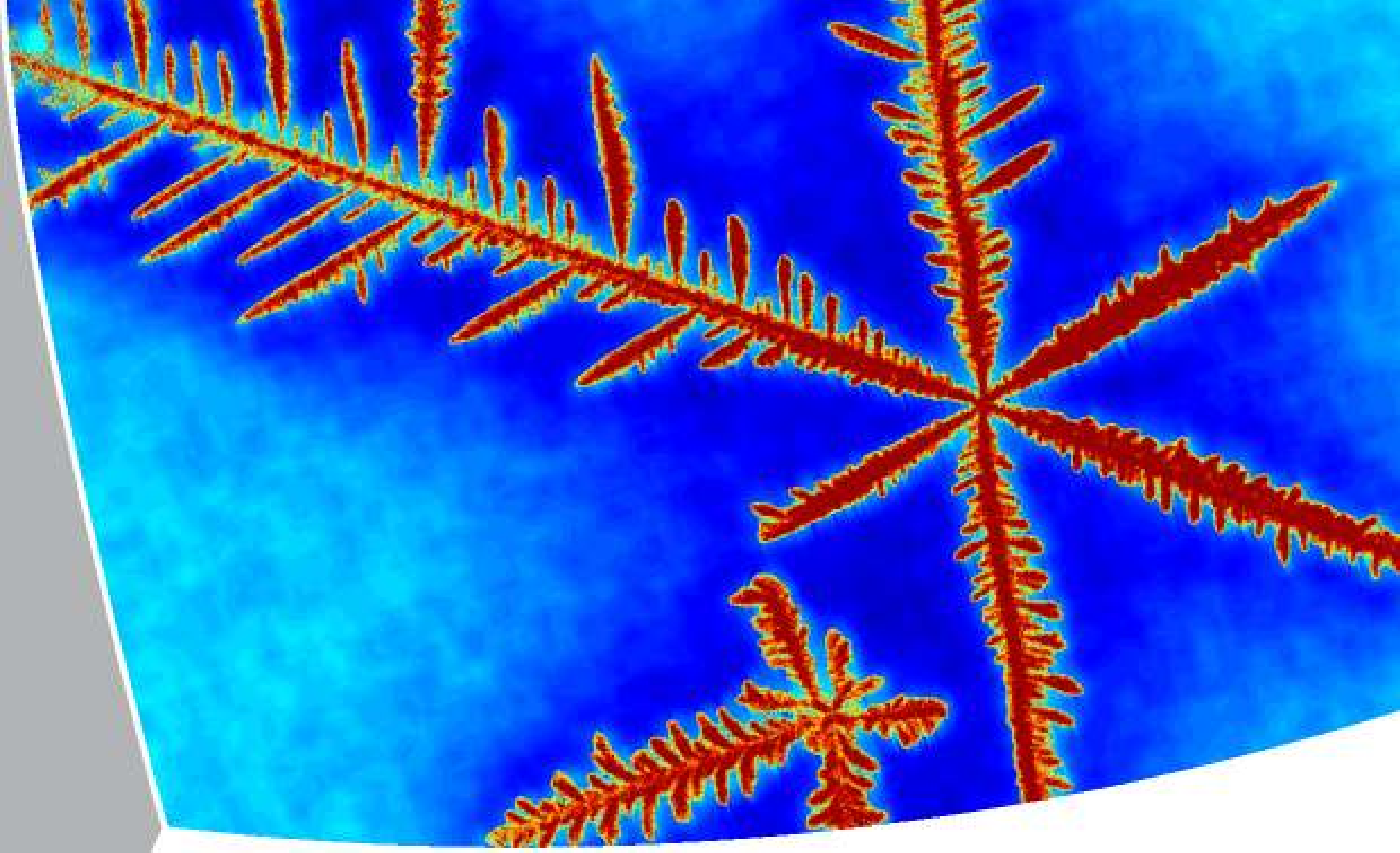

Institut für Materialphysik im Weltraum

Annual Report 2017

DLR

Institut für Materialphysik im Weltraum

Deutsches Zentrum für Luft- und Raumfahrt

Annual Report 2017

Impressum:
Institut für Materialphysik im Weltraum
Deutsches Zentrum für Luft- und Raumfahrt (DLR)
51170 Köln

Tel. +49 2203 601 2331
Fax: +49 2203 61768
e-mail: materialphysik@dlr.de

Cover image: The radiography image shows two equiaxed Al-dendrites growing in an Al-46wt.% Ge melt. The contrast between the solid dendrites (colored in red) and the melt (colored in blue) results from the different X-ray attenuations of aluminum and germanium. The 200 u m thin sample is monitored in-situ during cooling with a constant rate. Due to the real-time observation of the solidification process, we can analyze the evolution of the growing dendrites to derive important growth characteristics. The different blue tones of the melt provide information on the composition changes in the extra-dendritic liquid. This information is crucial for a proper experiment to model comparison.

Contents

1 Reports **1**

1.1 Methods Development 1

TEMPUS Parabolic Flight Campaign September 2017 2

RAMSES – a sounding rocket module for investigation the dynamic clustering of self-propelled particles in microgravity 3

EML Experiments onboard the ISS 4

Plasmakristall-4: Complex Plasma Laboratory on the International Space Station 5

Ekoplasma / Plasmalab 6

New radio-frequency setup for studying large 2D complex plasma crystals 7

Activated adsorption of water affects photosynthesis 8

Comparison of Viscosity Data on Liquid $Ni_{66.7}B_{33.3}$ measured with Oscillating Cup and Oscillating Drop Method 9

1.2 Liquid and Melt Properties 10

Electrical resistivity and thermal expansion of liquid metals and semiconductors 11

Atomic dynamics in glass-forming Hf-Ni melts 12

Mixing effects in a ternary Hf-Zr-Ni metallic melt 13

Combined Interdiffusion and Self- Diffusion Analysis in Al-Cu Liquid Diffusion Couple 14

Mismatch of viscosity in bulk metallic forming melts 15

Industrial grade versus scientific pure: Influence on melt properties 16

1.3 Solidification, Nucleation and Growth 17

Transient nucleation and microstructural design in flash-annealed bulk metallic glasses 18

Metastable phase formation in undercooled Nd-Fe-B alloy melts processed by electromagnetic levitation on ground and on board the ISS 19

Drendrite growth kinetics of fcc and bcc structured phases in undercooled melts 20

Solidification velocity and delay time of undercooled Fe-Ni alloys 21

The poisoning mechanism of Germanium on the grain refiner system Al-5Ti-1B 22

Morphological transition of Al-dendrites in Al-Ge 23

The ZrNi droptube experiment 24

Microstructure characterization of $CoCrFeNiMnPd_x$ eutectic high-entropy alloys 25

1.4 Granular Matter and Related 26

Influence of Mineral Composition on Sintering Lunar Regolith 27

Statistical nature of granular tribocharging 28

Approaching jamming in microgravity and on ground 29

THz transmission of dense granular media 30

Rheology of Granular Fluids 31

Rheology of Hertzian Spheres 32

1.5 Complex Plasmas 33

Instabilities in bilayer complex plasmas: Wake-induced mode coupling 34

Coupling of Noncrossing Wave Modes in a Two-Dimensional Plasma Crystal 35

Spinning particle pairs in a single-layer complex plasma crystal 36

Photophoretic force on microparticles in complex plasmas 37

Moment fluid equations for ions in weakly ionized plasma 38

Momentum transfer cross-section for ion scattering on dust particles 39

Influence of microparticles on rf plasmas: experiments and simulation 40
Wake-mediated propulsion of an upstream particle in two-dimensional plasma crystals 41
Density waves at the interface of a binary complex plasma 42
Observation of metallic sphere – complex plasma interactions in microgravity 43
Instability onset and scaling laws of an auto-oscillating turbulent flow in a complex plasma 44
Fingerprints of different interaction mechanisms on the collective modes in complex (dusty) plasmas 45
Thermodynamics of two-dimensional Yukawa systems across coupling regimes 46
Grüneisen parameter for strongly coupled Yukawa systems 47
Collective modes in simple melts: Transition from soft spheres to the hard sphere limit 48

1.6 Theory and Simulation 49
Crystal Growth under Fluid Flow 50
Model for the Chemotactic Motion of a Random Walker in a Porous Medium 51
Mode Coupling Theory of Active Brownian Particles 52
Active Brownian Particles in Crowded Media 53
Mode-Coupling Theory for Active Brownian Particles: Anisotropic and Sheared Systems 54
Glassy dynamics in highly asymmetric binary mixtures of hard-spheres 55
Glass-Transitions in Dipolar Fluids 56
On the generalized generalized Langevin equation 57

2 Publications and Patents **59**

2.1 Peer-Reviewed Publications 59
2.2 Books and Book Chapters 60
2.3 Other Publications 60

3 Presentations **61**

3.1 Institute Seminar 61
3.2 Talks given by institute members 62
3.3 Doktorandenrunde 64

4 Lecture Courses and Lectures **65**

5 Graduations **65**

6 Awards **66**

7 Fellows **66**

8 Events and Campaigns **66**

9 Workshops organized by the institute **67**

10 Third-Party Funding **68**

11 Author Index **73**

1 Reports

1.1 Methods Development

TEMPUS Parabolic Flight Campaign September 2017

D. Bräuer,* M. Balter, M. Engelhardt, D. Heuskin, G. Lohöfer, K. Prochnow, J. Schmitz, S. Schneider, and M. Wegener

Institut für Materialphysik im Weltraum, Deutsches Zentrum für Luft- und Raumfahrt (DLR), 51170 Köln, Germany

The TEMPUS facility (Containerless Electro-Magnetic Processing Under Microgravity Conditions) allows processing of electrically conductive samples of alloy systems in microgravity. Without contact to any container, samples are positioned and heated by electromagnetic fields generated by a coil of 18 mm in diameter. First, the sample is positioned, melted and heated up to a predefined temperature. While the positioning field is still active, the heater field is switched off. As a result, the sample cools down and remains liquid (and in most cases undercools below its melting point) until it solidifies. Before solidification, stimuli can be applied while diagnostic tools monitor the temperature and capture videos. From this data, thermophysical properties of the examined sample, like surface tension, thermal expansion, or viscosity can be determined. For the latter measurements the oscillating droplet method is used, where surface oscillations are triggered by pulses of the heater field. From the dampening of these oscillations the viscosity can be deduced and from their frequency the surface tension can be calculated. The rapid advancement of phases solidifying and microstructures forming out of the undercooled melt are captured by a high speed camera with up to 40000 frames per second.

In September 2017, a parabolic flight of the TEMPUS facility has been performed as part of the 30th DLR parabolic flight campaign. The TEMPUS facility preparation and operation, as well as the experiment preparation and operations program was led by DLR-MP. The facility was operated on four days with 31 parabolas each. Experiments from 15 proposals (DLR-RD and DLR-MP) were conducted and 19 samples were processed. Most of the experiments used the oscillating droplet method. In addition three high speed solidification and two Chill Cooling samples (FIG. 1) were processed.

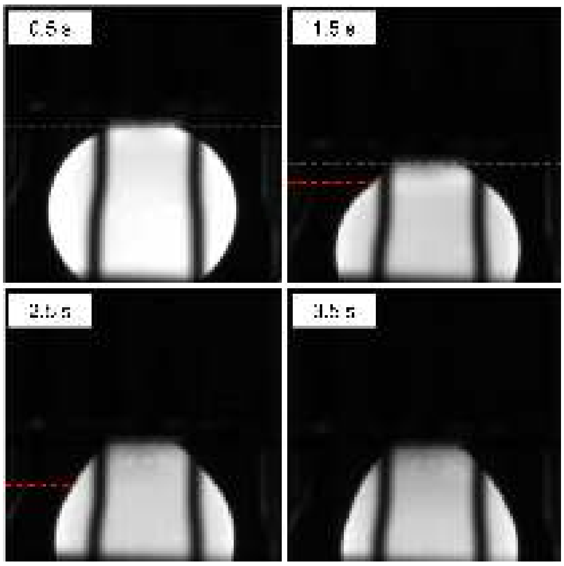

FIG. 1: Chill Cooling of Fe-0.9C-0.2Si. The blue line indicates the cooling plate. The red line shows the current solidification front at the given time after touching the cooling plate. (picture by T. Volkmann, DLR-MP)

Besides the scientific aims:

- Measurement of thermophysical properties
- Measurement of growth velocities
- Measurement of the sample electrical conductivities with the sample coupling electronics

the campaign had technical aims in addition:

- Test of different modulation profiles
- Influence of different sample holders on cooling mechanisms

On the 3rd flight day five parabolas were used to perform a test of a modified Knudsen-Cell. An Ag sample was levitated and heated to determine the vapor pressure under reduced gravity conditions. Therefore the TEMPUS facility was modified to provide the necessary mechanical and electrical interfaces.

The preparation for the parabolic flights include the physical characterization of the samples (material data compilation, emissivity and coupling data determination). The TEMPUS facility can be used to determine those parameters on ground which are used to develop settings for the parabolic flight. Based on this data, experiment operations were planned together with the scientific investigators. A flight schedule for the campaign was iterated and final operation procedures were developed. During the campaign, DLR-MP lead the experiment operations. On-line quick-loop analysis of experiments enabled to apply modifications to the experiment settings during flight. Lessons learned were implemented into the subsequent flight day operations plan in coordination with the investigators and the flight operations team.

After the flight, the respective facility-, experiment- and video-data were distributed to the scientists. All flight data (raw data, processed data and campaign information) will be long-term archived in the MUSC Hypertest system, which is online and accessible via Internet.

---

[*] Corresponding author: `dirk.braeuer@dlr.de`

RAMSES – a sounding rocket module for investigation the dynamic clustering of self-propelled particles in microgravity

R. Kessler,[1,*] P. Born,[1] C. Lozano,[2,3] C. Bechinger,[2,3] and Th. Voigtmann[1,4]

[1]Institut für Materialphysik im Weltraum, Deutsches Zentrum für Luft- und Raumfahrt (DLR), 51170 Köln, Germany
[2]2. Physikalisches Institut, Universität Stuttgart, Pfaffenwaldring 57, 70569 Stuttgart, Germany
[3]Max-Planck-Institute for Intelligent Systems, Heisenbergstraße 3, 70569 Stuttgart, Germany
[4]Institut für Physik, Heinrich-Heine Universität Düsseldorf, Universitätsstraße 1, 40225 Düsseldorf, Germany

Microscopic creatures like bacteria and cells have evolved survival-relevant capabilities to orient and move themselves to adapt to food and environmental conditions. To understand the physical principles of the active motion of microswimmers and their possible application in medicine, biology and engineering, simplified models are created. With the use of colloidal Janus particles dissolved in a water-lutidine mixture, active motion can be achieved with illumination [1]. The particles are beads of SiO_2 with a diameter of $d_p = 2\,\mu$m, with one hemisphere coated by a thin carbon layer. The particles are suspended in a water-2,6 lutidine mixture close to the lower critical point of demixing. At the critical demixing temperature of $T_c = 34°$C the solution changes to an emulsion. Upon setting a process temperature to $T_p = 28°$C $\pm\, 0.1\,$K and illumination with intensive light, local demixing sets in close to the dark hemispheres of the particles. The thus generated concentration gradient causes a flow around the particle and by that their self-propolsion. In addition, the particles undergo translational and rotational Brownian motion. Depending on particle concentration and self-propulsion speed (controlled by the illumination intensity), the systems undergo a transition from a homogeneous phase to a phase where dynamical clusters of different sizes are formed. The transition has been termed motility-induced phase separation (MIPS).

Investigations on Earth are limited to the quasi-two-dimensional case, because the sedimentation is dominant compared to the propulsion forces. Simulations suggest a dependence of MIPS on spatial dimension. Experiments in microgravity offer the possibility to study the behavior in three dimensions without the effects of boundaries.

RAMSES (Random motion of microswimmers-experiment in space) is designed to investigate the collective motion of artificial microswimmers in three dimensions. The experiment module is scheduled to fly on the sounding rocket MAPHEUS 7. It contains ten sample cells in two compartments, to allow a variation of parameters.

For each cell, propulsion is generated by seven high-power LEDs and an optical system of eight lenses and one cone. The LEDs emit light with a dominant wavelength of $\lambda = 532\,$nm that is strongly absorbed by the carbon layers. The light is collimated and bundled by lenses. To homogenize the light intensity across the sample-cell surface of $d_{\text{cell}} = 2\,$mm, a fiber-optic cone is used.

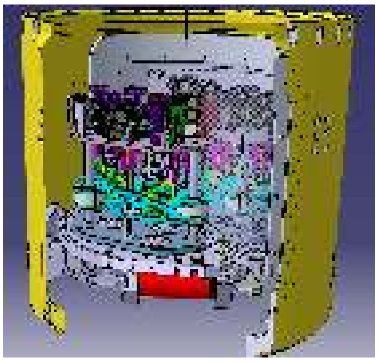

FIG. 1: Sectional view of the module

The sample cells are cylinders of diameter $2\,$mm and height $1\,$mm and consist of glass cover plates that are hydrophobically coated, separated by a spacer. After filling the cells with the suspension, the cavity is closed with a screwlock. The cells are mounted on a rotatable deflection mechanism to counteract centrifugal forces due to the rotation of the rocket during the launch phase. Entering the μg phase, a spindle motor lifts the illumination system and thereby locks the cells in place.

The process temperature is controlled by Peltier elements embedded in the receptor. The receptor is also equipped with an eccentric motor and Piezo crystals generating ultrasonic waves. Running the eccentric motor generates a flow inside the suspension to lift particles from the cell surface when they are stuck after the launch. In combination with ultrasonic agitation, agglomerations can be destroyed to create homogeneou initial conditions at beginning of microgravity.

All controls and recordings run on a Raspberry Pi 3B with the Pi camera module combined with a microscope lense. A small magnification of about 1.8 enables a depth of field of about $0.4\,$mm. Image sequences are stored on an SD card and processes post-flight.

Due to the limited stability of the suspensions, the two compartments are inserted in late access and fixed by appropriate guide rails and locking pins. A LAN connection enables direct communication with the ground PC during the launch procedure, so all systems can be checked for functionality and controlled prior to lift-off.

---

[*] Corresponding author: `raphael.kessler@dlr.de`

[1] J. R. Gomez-Solano, S. Samin, C. Lozano, P. Ruedas-Batuecas, R. van Roij, and C. Bechinger, *Tuning the motility and directionality of self-propelled colloids*, arXiv:1709.06339 (2017).

EML Experiments onboard the ISS

S. Schneider,* J. Schmitz, M. Engelhardt, and M. Lammel

Institut für Materialphysik im Weltraum, Deutsches Zentrum für Luft- und Raumfahrt (DLR), 51170 Köln, Germany

EML is an electromagnetic levitation facility, which is able to process liquid metallic samples without direct containment under reduced gravity conditions. In 2014 it was installed in the European drawer rack (EDR) in the Columbus module on the ISS. After a commissioning phase in 2014 & 2015 first experiments were performed in 2015. The complete Batch 1 (first sample chamber) was finished in 2016. Beginning of 2017 the sample coupling electronics (SCE) was installed and successfully commissioned. This device allows for a measurement of the electrical resistivity of a levitated sample. Subsequently, the sample chamber for the second Batch of EML operations was attached to the facility. After another successful Facility Checkout Experiment (FCE) the first subsets of Batch 2 experiments were performed. In this series of operations doped semiconductors, Ge and SiGe alloys, were processed for the first time in EML. The experiments on Batch 2 samples will be continued in 2018.

Several scientific measurements were performed:

- Surface tension and viscosity using the oscillating drop method
- Specific heat using modulation calorimetry
- Growth velocity of the solidification with the high speed video camera
- Influence of electromagnetic stirring on solidification and surface tension & viscosity
- Solidification and time to crystallization
- Measurement of electrical resistivity

Due to the facility's complexity an extensive ground support program is performed at the DLR Institute of Materials Physics in Space prior to any experiment runs:

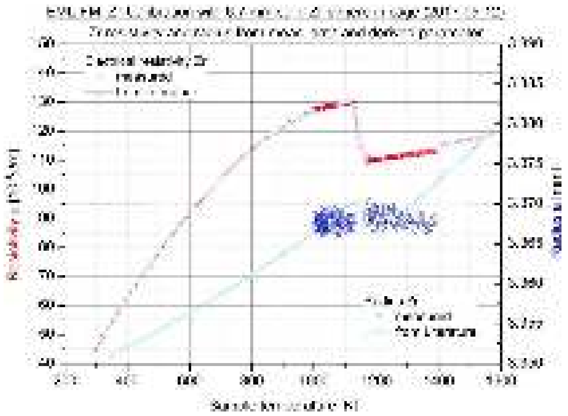

FIG. 1: SCE Measurement of the electrical resistivity of Zr.

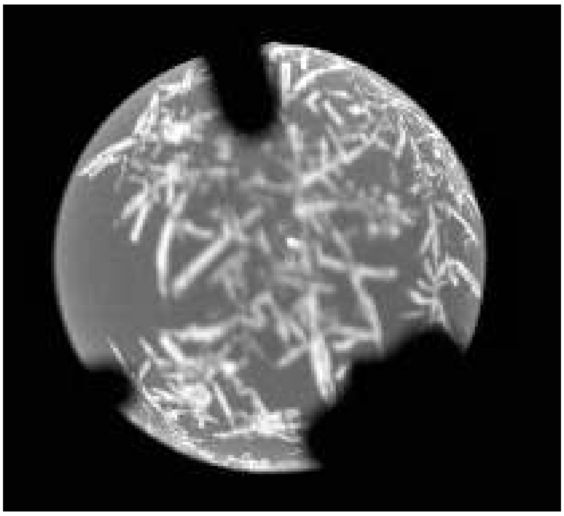

FIG. 2: Screenshot of SiGe during solidification: In Batch 2, a doped semiconductor was processed for the first time.

The samples for EML are characterized, the experiment is planned and in detail laid down as a sequence which runs semi-automatically on ISS. Camera control files and safety measures need to be implemented. This is done in cooperation with the responsible scientists (PIs). Prior to on-orbit performance, the experiment is simulated by a special software and tested on a ground based EML facility, the operational model. During this validation, a flawless progression of the developed parameters and the reactions of all subsystems are verified. Only after that, the experiment can be converted and uploaded to the flight model on ISS.

During the remotely-controlled experiment performance at MUSC, MP personnel supports the PI by giving advice on running the experiment, interaction options and optimization of experiment parameters. Temperatures can be adapted, modulation frequencies optimized etc., which enables the PI to react on the recent experiment results in near real time (overheating can be adapted to observed undercooling, pulse distribution adapted to undercooling, recalescence detection parameters optimized etc.).

Due to this extensive preparation the operational performance was very successful and almost all experiments could be performed as planned. Already during the experiment performance the house keeping data were made available at the Hypertest archive. As video data have to be downloaded during the following day(s) these data were available after a short time.

The next experiment series of EML – Batch 1.3 & 2.3 – shall be processed in summer 2018.

---

* Corresponding author: `stephan.schneider@dlr.de`

Plasmakristall-4: Complex Plasma Laboratory on the International Space Station

M. Y. Pustylnik,[1,*] T. Hagl,[1] T. Antonova,[1] V. Nosenko,[1] H.M. Thomas,[1] A.M. Lipaev,[2] A.V. Zobnin,[2] A.V. Usachev,[2] V.M. Molotkov,[2] M. Kretschmer,[3] and M.H. Thoma[3]

[1] Institut für Materialphysik im Weltraum, Deutsches Zentrum für Luft- und Raumfahrt (DLR), 82234 Wesseling, Germany
[2] Joint Institute for High Temperatures, Russian Academy of Sciences, 125412 Moscow, Russia
[3] I. Physikalisches Institut, Justus-Liebig-Universität Gießen, 35392 Gießen, Germany

Plasmakristall-4 [1] is an International-Space-Station-based facility for the investigation of complex plasmas. Dusty plasmas are electrically quasi-neutral media, containing together with electrons, ions, neutral molecules and radiation also solid microparticles. Complex plasmas are a very special subdivision of dusty plasmas: They are created in purpose to study generic phenomena occurring in liquids and solids [2]. Coupling between the microparticles might be so strong that their subsystem undergoes a phase transition and solidifies forming a so-called plasma crystal. Microgravity is an essential condition in principle allowing to obtain unstressed 3D complex plasmas.

PK-4 is designed to study flowing complex plasmas. The heart of the experiment is a cylindrical glass plasma chamber of 3 cm diameter and about 20 cm working area length. The discharge is created and supported by a power supply in the current source regime with 3 mA maximal current and 3 kV maximal voltage. The polarity of the discharge can be switched with the frequency up to 5 kHz. Polarity switching function allows to trap the microparticles within the working area of the chamber since, starting from the frequency of several hundred Hz, the microparticles (plastic microspheres 1-10 μm diameter) are insensitive to the discharge polarity switching. Microparticle flow velocity can be precisely controlled by the duty cycle of the polarity switching. Other manipulation devices like RF-coils (for local plasma density increase), infrared manipulation laser, thermal manipulator are also available.

PK-4 is accommodated in the Columbus module of the International Space Station inside the European Physiology Module rack. It is operated jointly by ground operators in the control center CADMOS (Toulouse, France) and by the Russian ISS crew members on board. The PK-4 science team contains scientists from 11 countries.

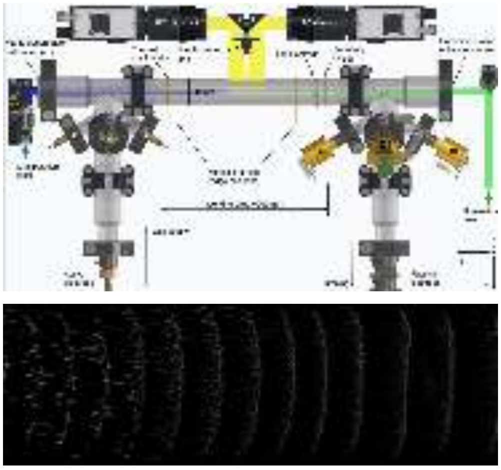

FIG. 1: Schematic of the PK-4 experiment [1] and an image of dust acoustic wave instability recorded during the campaign 4 in February 2017.

PK-4 was launched in October 2014 and commissioned in June 2015. Since that time, four scientific campaigns have been conducted.

In February 2017, campaign 4 was conducted. The following experiments have been planned and executed:

- Microparticle charge and ion drag force measurement
- 3D structure of shear flow
- Density wave generation by the manipulation laser
- Observation of the lane formation
- Phase transition between string and normal fluid

The preparation of the campaign included the development, test, validation and delivery (to CADMOS) of the experiment scripts. The above-mentioned experiments were executed within three experimental days. Data from campaign 4 have been delivered to the scientists. Data analysis is ongoing.

In May 2017, ESA decided to suspend scientific operations of PK-4 due to the discovered transient overvoltage of the cameras. Loss of a camera on board would result in a significant reduction of the PK-4 scientific performance. Additional hardware is being developed to resolve this issue. It is expected to resume the scientific operations of PK-4 in October 2017.

In December 2017, Institute for Material Physics in Space hosted a PK-4 Facility Science Team Meating meeting, which was attended by more then 30 scientists from Europe, Russia, USA and Japan.

All authors greatly acknowledge the joint ESA-Roscosmos "Experiment Plasmakristall-4" on board the International Space Station and support from DLR/BMWi under grant FKZ 50WM1441.

---

* Corresponding author: `mikhail.pustylnik@dlr.de`

[1] M.Y. Pustylnik, M.A. Fink, V.N. Nosenko et.al., Rev. Sci. Instrum. **87**, 093505 (2016).

[2] A. Ivlev, H. Löwen, G. Morfill, C.P. Royall, *Complex plasmas and Colloidal Dispersions: Particle-resolved Studies of Classical Liquid and Solids* (World Scientific, Singapore, 2012)

Ekoplasma / Plasmalab

C. A. Knapek,* P. Huber, D. P. Mohr, S. Peralta Friedburg, J. G. Prell, A. Börngen, H. M. Thomas, E. Zähringer, C. George, and T. Hagl

Institut für Materialphysik im Weltraum, Deutsches Zentrum für Luft- und Raumfahrt (DLR), 82234 Wesseling, Germany

The Ekoplasma/Plasmalab project is the development of the future multi-purpose laboratory for research on complex plasmas in microgravity on the International Space Station (ISS). The project is performed in cooperation with the Joint Institute for High Temperatures (JIHT) of the Russian Academy of Sciences, Moscow, and will be accommodated on the Russian Science Energy Module (SEM), in cooperation between German and Russian space agencies.

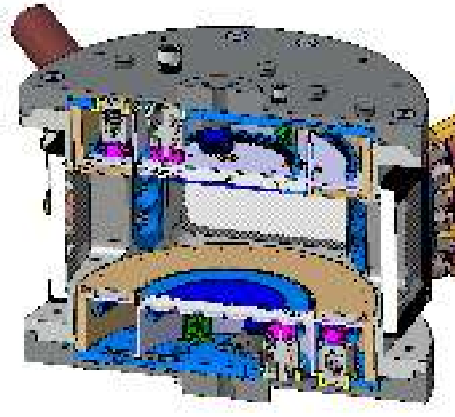

FIG. 1: New design of the Zyflex plasma chamber for the bread-board model.

The core of the experimental apparatus is the newly developed "Zyflex" plasma chamber. In 2017, the design of a bread-board model started, based on the pre-development chamber which has been used successfully during the last years in the laboratory and on 5 parabolic flight campaigns. The bread-board design is shown in Fig. 1. It features an improved and robust electrode motion system, a symmetric gas in- and outflow, space for up to 12 particle dispensers, and a complex design for gas distribution and accommodation of the internal harness. An electronic for experiment control has been developed and is in its test phase, providing several digital and analog channels, a highly configurable output array, and using PTP (precision time protocol) for time synchronization. The requirements for a bread-board model of the 4-channel hf-generator for plasma generation were identified and a requirements document was prepared. Further, an optimization of the design of the particle dispensers to provide larger amounts of particles was started. A target design for the calibration of the 3D stereoscopic camera setup was developed, and the experiment control software was optimized and adapted to the new electronics.

Scientific results from parabolic flight campaigns and experimental laboratory work were presented on 3 conferences by the team members, in 4 talks and 3 posters. 4 contributions were accepted for publication in AIP conference proceedings (in press) for the 8th International Conference on the Physics of Dusty Plasmas (ICPDP). One publication (E. Zähringer) is in preparation to be sent to Physics of Plasmas.

An accommodation study was performed by the company OHB Munich on behalf of DLR-MP in 2017. The study output were two reports: a technical assessment and planning report with a detailed architectural proposal (see. e.g. Fig. 2), and a managerial report giving a cost and resources estimate and the schedule with all work packages necessary to complete Phases A-D, for both space industry and DLR-MP, which will be responsible for development of the core experiment hardware and software. The study outcome shows a feasible project for an accommodation on SEM, with a launch in spring 2023. In May 2017, the joint scientific protocol between JIHT and DLR-MP was signed by both parties, emphasizing the cooperation on the scientific side. A letter of intent, signed by DLR and the Russian Space Agency Roscosmos in July 2017, emphasizes the strong wish on both sides for proceeding with the project as a joint German-Russian cooperation. The preparation of a specific agreement between Russian and German space agencies was brought on its way in November 2017.

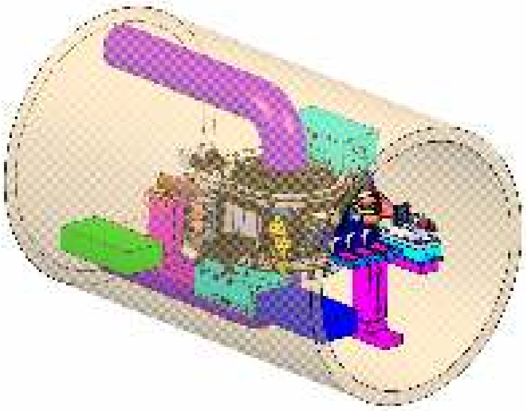

FIG. 2: Proposed container for parts of the experimental hardware to be launched to the ISS.

The PlasmaLab/Ekoplasma project is funded by DLR/BMWi under grant FKZ 50WM1441, and by the Bavarian Ministry of Economic Affairs and Media, Energy and Technology (StMWi).

* Corresponding author: `christina.knapek@dlr.de`

New radio-frequency setup for studying large 2D complex plasma crystals

V. Nosenko,* J. Meyer, S. K. Zhdanov, and H. M. Thomas

Institut für Materialphysik im Weltraum, Deutsches Zentrum für Luft- und Raumfahrt (DLR), 82234 Wesseling, Germany

Complex, or dusty plasmas are suspensions of fine solid particles in a weakly ionized gas. The particles charge up by collecting electrons and ions from plasma and can be confined in the plasma regions where their weight is balanced by other forces, e.g. electrostatic force. Due to the interplay between their mutual interactions and external confinement, the particles can form various structures which are often strongly coupled and possess liquid-like or even solid-like order. The crystalline phase of complex plasma is called the plasma crystal. In laboratory experiments with monodisperse particles, single-layer (2D) plasma crystals can be obtained. Complex plasmas are popular versatile model systems that are used to simulate the structure and dynamic processes in regular liquids and solids. With microparticles serving as proxy “atoms,” they offer the benefit of real-time direct imaging of various processes at the “atomistic” level. Examples include the studies of waves, phase transitions, and transport phenomena in complex plasmas.

There is a growing body of evidence that many properties of complex plasmas, such as thermal conductivity and diffusion coefficient may be system-size dependent. To test this assumption, experiments are needed where the size of a complex plasma can be varied in a wide range. So far, the existing experimental setups (based on various modifications of the GEC rf reference cell) allowed the maximum size of a high-quality 2D plasma crystal of about $6-7$ cm. To obtain a much larger uniform 2D plasma crystal, a larger setup is necessary. In this presentation, we report on the new radio-frequency setup that has been built and is now operational in the research group on complex plasmas, see Fig. 1. It is based on a relatively large (90 cm in diameter) vacuum chamber. A radio-frequency (rf) discharge at 13.56 MHz is created between the lower electrode and the grounded chamber walls; dust particles levitate in the plasma (pre)sheath above the electrode and are observed through the large top glass window and through the side windows.

FIG. 1: Experimental setup for studying large 2D complex plasma crystals. Argon plasma is created in the vacuum chamber which is a stainless-steel cylinder 90 cm in diameter and 34 cm in height with ports for imaging and measurements. The powered rf electrode is a 85 cm diameter aluminium-alloy disc with the chamber walls serving as the grounded electrode. Micron size particles are suspended in the plasma (pre)sheath above the rf electrode. The particles are illuminated with lasers and imaged from the top and from the side with fast video cameras.

The ultimate base pressure in the chamber is 9×10^{-4} Pa when only the smaller of the two turbo pumps available is used. The practical range of the gas pressure for plasma operation is $p_{\rm Ar}=0.1-20$ Pa. The practical range of the rf power supplied by the generator is $P_{\rm rf}=5-350$ W. Melamine formaldehyde microspheres with a diameter of 9.19 ± 0.09 μm are currently used.

To test the experimental setup, capacitively coupled rf discharge in argon at $p_{\rm Ar}=0.4$ Pa and $P_{\rm rf}=150$ W was used. Dust particles introduced into the plasma were suspended in the plasma (pre)sheath at the height of 1.5 cm above the rf electrode. The horizontal confinement of the particles was provided by a (temporarily used for test purposes) aluminium-alloy ring with the internal diameter of 30 cm placed on the rf electrode. The particles self-organized into a single-layer plasma crystal with a diameter of ≈ 28 cm. The total number of particles in it was ≈ 15000, they were arranged in a highly regular triangular lattice with hexagonal symmetry. Further testing showed that stable 2D plasma crystals can be suspended in argon plasma at the pressure as low as $p_{\rm Ar}=0.1$ Pa. The Epstein neutral gas damping rate for the particles in these experimental conditions is $\nu_E=0.13\ {\rm s}^{-1}$. This is a small fraction (less than 1%) of the complex plasma’s Einstein frequency. Therefore, virtually undamped dynamics of the complex plasma can be studied.

Using the new setup, the coupling of the transverse vertical and longitudinal in-plane dust-lattice wave modes in a 2D complex plasma crystal in the absence of mode crossing was experimentally observed for the first time [1]. This observation was facilitated by the small damping rate for particles due to the low gas pressure, high quality of the plasma crystal, and presumably large plasma wake parameter.

We thank Heinrich Huber, Hermann Kronbauer, Johannes Prell, Alexander Börngen, Sebastian Peralta Friedburg, and Claudius George for their valuable help in designing and building the experimental setup reported in this contribution.

* Corresponding author: `V.Nosenko@dlr.de`

[1] J. K. Meyer, I. Laut, S. K. Zhdanov, V. Nosenko, H. M. Thomas, Phys. Rev. Lett. (2017), accepted.

Activated adsorption of water affects photosynthesis

Dietmar Neuhaus*
Institut für Materialphysik im Weltraum, Deutsches Zentrum für Luft- und Raumfahrt (DLR), 51170 Köln, Germany

Years ago it was discovered, that cycles of adsorption and desorption of water on surfaces causes an increase of the maximum of adsorbed water on surfaces [1]. The observed effect was called activated adsorption of water. Several applications of this effect are in discussion [2]. For example it was proposed to use the effect for the irrigation of plants in greenhouses over the gas phase of water [3]. New investigations on the activated adsorption of water on leaves have shown now, that the activation process itself influences the photosynthesis of leaves.

In figure 1 the object of investigation, a part of a bush bean leave, is shown. Leaves of bush beans were selected for the investigations because of the quite thin wax layer (cuticula) on the surface of these leaves, so that the chloroplasts, which are the parts of a leave where photosynthesis occurs, are easy to observe.

The photosynthesis system of the bush bean leaves were tested with the fluorometry method. In this method a fluorescence curve is measured, when, after the leaves are kept for a certain time in darkness, the leaves are illuminated and fluorescence light emitted from the leaves is measured. Fluorescence light was measured after activation with 400 nm light around 675 nm wavelength, a wavelength range where it is known that chloroplasts emit flourescence light if activated. In figure 2 a typical fluorescence curve is shown. After starting the illumination with constant power, fluorescence light emission is immediately observed, whose intensity increases rapidly, goes through a maximum and decays to reach steady state conditions.

The time dependent intensity of the fluorescence light has its origin in the photosystem II complexes (PSII) located in membranes of the chloroplasts. PSII collects and absorbs photons necessary for the decomposition of water in oxygen, electrons and protons needed for the photosynthesis, and emits fluorescence light if this process is blocked. Blocking occurs, if subsequent processes are not able to take the electrons produced. The quenching of the fluorescence light indicates that electrons produced in PSII are increasingly absorbed by subsequent processes to finalize photosynthesis. In this context the fluorescence quenching rate is taken as a measure for the vitality of the investigated leaves. A high quenching rate is typical for a vital leave.

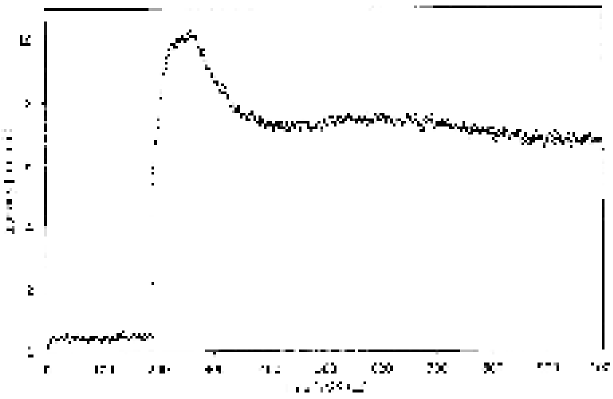

FIG. 2: Fluorescence curve (emission at 675 nm) of a bush bean leave. Illumination with blue light (400 nm) starts at 4 s.

FIG. 1: Detail of a bush bean leave, the object of the investigations on the activated adsorption of water on leaves.

Experiments were performed on single bush bean plants by selecting leaves of the plant which were treated with different atmospheres. By selecting mainly the three leaves at a single leaf stalk of a bush bean, leaves of the plant were investigated that are as similar as possible to make the results comparable. One of the three leaves was not treated as a reference. The others were treated by an atmosphere with high relative humidity or cycles of high and low relative humidity atmospheres, necessary for the mentioned activation. Series of experiments with different leaves were performed. We find that the activation cycles increase the quenching rate of the fluorescence light. This means that the application of activation cycles on bush bean plants increases the vitality of this plants, which supports plant protection [4]. Plant protection will become increasingly important, considering that plant production has to double in the period from 2005 to 2050 to feed world population, according to an estimation of the FAO of the United Nations.

* author: `Dietmar.Neuhaus@dlr.de`

[1] D. Neuhaus, Adsorption, 19, (2013), p. 1127-1135
[2] D. Neuhaus, Patent DE 10 2010 026 591.8
[3] D. Neuhaus, Patent DE 10 2012 220 111.4
[4] D. Neuhaus Patent application DE 10 2017 215818.2

Comparison of Viscosity Data on Liquid $Ni_{66.7}B_{33.3}$ measured with Oscillating Cup and Oscillating Drop Method

S. Zimmermann,* F. Yang, and A. Meyer

Institut für Materialphysik im Weltraum, Deutsches Zentrum für Luft- und Raumfahrt (DLR), 51170 Köln, Germany

The viscosity η describes the macroscopic transport of momentum by the collective motion of the particles in a liquid. Conventionally, the techniques used for measuring the viscosity of liquids are container-based. These techniques are especially applicable to chemically inert liquids. Due to high melting temperatures and the chemical reactivities of metallic melts the measured data become unreliable, if e.g. possible reactions between the melt and the container influence the experimental results. This depends on the temperature and the sample/crucible material used for the measurement [1].

One possibility to circumvent this problem is the use of containerless investigation techniques such as levitation. Electrostatic levitation (ESL) in combination with the so called oscillating drop method (ODM) is one of the techniques to measure the viscosity of levitated liquid droplets. With this method, reliable viscosity data can be obtained as long as a single oscillation mode dominates viscous damping [2]. Heintzmann et al. [2] showed for ZrNi that this is the case for data in the viscosity range of 10 mPas to 250 mPas using sample masses below 100 mg [2], where the measurement results show no sample mass dependence.

In this work, this was proven for the liquid alloy $Ni_{66.7}B_{33.3}$ by measuring different sample masses via ODM combined with ESL. Fig. 1 presents the measured results, which show no sample mass dependence.

Liquid $Ni_{66.7}B_{33.3}$ has been chosen, because it is a low viscosity system, which is on the one hand suitable for levitation methods, so that its viscosity can be measured using ODM combined with ESL. On the other hand, $Ni_{66.7}B_{33.3}$ is a chemically inert metallic melt, which can be observed also via the container-based oscillating cup method (OCM). Measuring the viscosity via OCM is necessary since the ODM provides no longer reliable data for viscosities below 10 mPas [2].

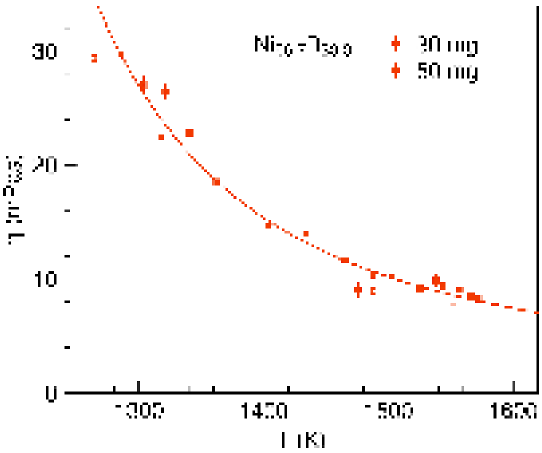

FIG. 1: Melt viscosity determined by electrostatic levitation combined with the oscillating drop method. Different sample masses of 30 mg (full symbols) and 50 mg, (hollow symbols) show no mass dependence for the viscosities.

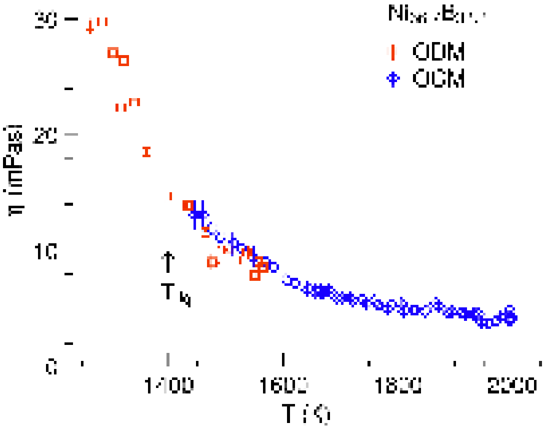

FIG. 2: Viscosity of $Ni_{66.7}B_{33.3}$ versus temperature. Blue diamonds represent η measured with the oscillating cup method. The red squares correspond to data measured by using oscillating drop method in combination with electrostatic levitation.

Fig. 2 shows the temperature dependent melt viscosity of $Ni_{66.7}B_{33.3}$ measured under different experimental conditions. First, the viscosity of $Ni_{66.7}B_{33.3}$ was measured in a temperature range of around 325 K from about 1250 K to about 1575 K and a viscosity range of 8 mPas to 30 mPas using the ODM in combination with ESL. The results are shown in Fig. 2 by red squares. Furthermore, we were also able to investigate the viscosity of $Ni_{66.7}B_{33.3}$ in a low viscosity range below 10 mPas. Therefore we used the OCM. The results are shown in dependence of the temperature in Fig. 2 by blue diamonds. Here, the data cover a temperature range of around 550 K from about 1450 K to about 2000 K and a viscosity range from about 4 mPas to 13 mPas. In comparison, the results obtained by the two methods agree within measurement errors.

By combining both methods (ODM with ESL and OCM), it was possible to measure reliable viscosity data over a wide temperature range of more than 700 K. This allows the verification of relations like e.g. the Stokes-Einstein relation.

---

[*] Corresponding author: `sarah.zimmermann@dlr.de`

[1] I. Jonas et al., Appl. Phys. Lett. to be published 2018.

[2] P. Heintzmann et al., Appl. Phys. Lett. **108**, 241908 (2016).

1.2 Liquid and Melt Properties

Electrical resistivity and thermal expansion of liquid metals and semiconductors

G. Lohöfer*

Institut für Materialphysik im Weltraum, Deutsches Zentrum für Luft- und Raumfahrt (DLR), 51170 Köln, Germany

The temperature-dependent electrical resistivity $\rho(T)$ of liquid metals or semiconductors has great relevance in technical applications. Besides of this aspect $\rho(T)$ is also a sensitive indicator for structural changes in the melt. In metallic liquids and liquid semiconductors at high temperatures the electrical resistivity results from the scattering of the free conduction electrons at the randomly fluctuating metal ions. This assumption explains also very well the usually observed linear increase of $\rho(T)$ with increasing temperature T and thus increasing kinetic energy of the atomic density fluctuations.

At lower temperatures of the melt the attractive forces between the atoms become more and more important. In an alloy with two or more components the different interatomic forces between the different species may lead to a chemical short range ordering of the atoms and thus to a formation of small structures in the melt, which should increase the scattering cross section for the conduction electrons and thus also the electrical resistivity. Consequently, the onset of ordering phenomena with decreasing temperature should lead to a deviation of $\rho(T)$ from the typical linear temperature dependence. The lower the temperature of the melt is, the more pronounced this effect should show. This fact makes a measurement of ρ interesting in particular in the undercooled melt, i.e., in the liquid state below the melting temperature T_m.

To enter its undercooled state the melt has to be handled containerlessly and any measurement has to be performed contactlessly. EML is a microgravity electromagnetic levitation facility onboard the "International Space Station" (ISS), which handles well conducting liquids containerlessly and without the strong disturbances which electromagnetic levitated melts experience normally on earth. The newly integrated measurement electronics (SCE) enables now also an inductive and thus contactless measurement of the electrical resistivity and thermal expansion of the levitated melt. Since its installation in early 2017 several samples have been processed in the EML and measured by the SCE. In the following we show the received temperature dependent electrical resistivity of the liquid semiconductor $Si_{50}Ge_{50}$ as well as resistivity and thermal expansion of the metallic glass forming system $Zr_{64}Ni_{36}$ in its liquid and solid state.

The diagram for the liquid semiconductor $Si_{50}Ge_{50}$, see Fig. 1, shows exemplarily the above discussed deviation of the electrical resistivity $\rho(T)$ from the typical linear temperature dependence at deeper temperatures, which indicates an increasing formation of atomic structures in the melt with decreasing temperature T. In the deep undercooled state the increasing negative slope of $\rho(T)$ suggests that the formed structures even dominate more and more the electron scattering. This hypothesis is also supported by X-ray diffraction measurements on aerodynamically levitated and laser heated liquid droplets [1].

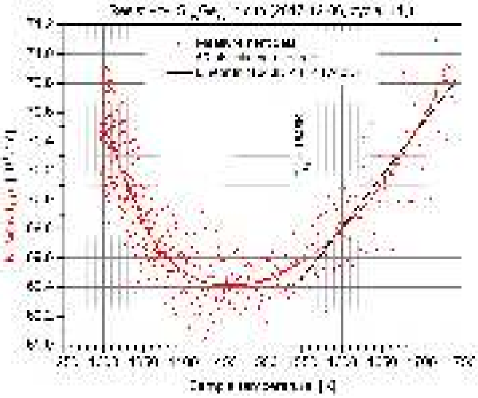

FIG. 1: Electrical resistivity of a $Si_{50}Ge_{50}$ melt above and below its melting temperature at 1548K (red dots) together with a sliding average of the data points (red line) and a linear fit to the data points above the melting temperature.

An example for a metallic melt in which the scattering of the free conduction electrons seems completely to be dominated by atomic structures in the melt is the glass forming system $Zr_{64}Ni_{36}$, see Fig. 2. Whereas the solid material shows the expected linear behavior of $\rho(T)$, which results from the scattering of the electrons at the lattice phonons, the electrical resistivity of the liquid material shows practically no dependence on the temperature.

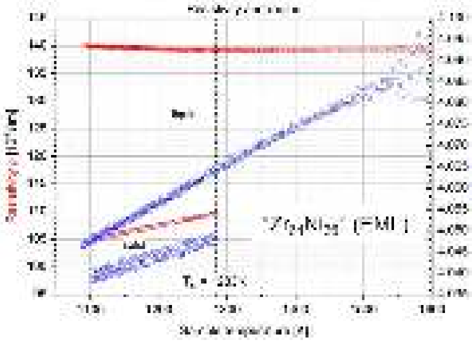

FIG. 2: Electrical resistivity (red dots) and radius (blue dots) of a levitated $Zr_{64}Ni_{36}$ sphere in the liquid state above and below its melting temperature at 1283K and in the solid state.

---

* Corresponding author: `Georg.Lohoefer@dlr.de`

[1] S. Krishnan et al., Journal of Non-Crystalline Solids **353**, 2975 (2007).

Atomic dynamics in glass-forming Hf-Ni melts

D. Holland-Moritz,[1,*] B. Nowak,[1] F. Yang,[1] Th. Voigtmann,[1] Z. Evenson,[2] and A. Meyer[1]

[1] *Institut für Materialphysik im Weltraum, Deutsches Zentrum für Luft- und Raumfahrt (DLR), 51170 Köln, Germany*
[2] *Heinz Maier-Leibnitz Zentrum (MLZ) and Physik Department, Technische Universität München, 85748 Garching, Germany*

The atomic dynamics in the liquid state is one of the key parameters in order to understand glass-formation processes. While the atomic dynamics in Zr-based glass-forming melts has been intensively studied in preceding investigations [1–5], here we present neutron scattering experiments on the atomic dynamics of glass-forming Hf-Ni alloy melts, for which the early transition metal component (Zr) is replaced by Hf.

In order to avoid possible reactions of the melts with crucible materials and in order to reduce background scattering at materials in the vicinity of the sample, the liquids are containerlessly processed under high vacuum by employing a compact electrostatic levitator specially developed for performing scattering experiments [3]. Self-diffusion coefficients were determined by quasielastic neutron scattering (QENS) at the time-of-flight spectrometer TOFTOF at the FRM-II.

The measured self-diffusion coefficients for $\mathrm{Hf_{35}{}^{nat}Ni_{65}}$ (blue crosses), $\mathrm{Hf_{35}{}^{60}Ni_{65}}$ (pink triangles), and $\mathrm{Zr_{36}Ni_{64}}$ [2] (red circles) are shown in Fig. 1. The Ni/Hf self-diffusion coefficient weighted by concentration and incoherent scattering cross sections measured for $\mathrm{Hf_{35}\,{}^{nat}Ni_{65}}$ is about a factor of 1.5 (1600 K) or 1.7 (1470 K), respectively, larger compared to the pure Hf self-diffusion coefficient measured for $\mathrm{Hf_{35}{}^{60}Ni_{65}}$. Since the Hf contribution ($\approx 20\%$) reduces the mean Ni/Hf self-diffusion coefficient of the measurement with $\mathrm{Hf_{35}\,{}^{nat}Ni_{65}}$, the pure Ni self-diffusion is faster by roughly a factor of 2 compared to the Hf self-diffusion. Such a dynamical decoupling has recently been observed in radiotracer measurements for binary $\mathrm{Zr_{36}Ni_{64}}$ melts [4].

The dashed lines in Fig. 1 represent an Arrhenius fit $D(T) = D_0\exp[-E_\mathrm{A}/(k_\mathrm{B}T)]$ to the data, where D_0 is the diffusivity at infinite temperatures, k_B is the Boltzmann constant, and E_A is the activation energy. For $\mathrm{Hf_{35}{}^{nat}Ni_{65}}$ we obtain an E_A for the mean Ni/Hf self-diffusion of (1.31 $\pm$ 0.06) eV. This value is nearly twice as large as for $\mathrm{Zr_{36}Ni_{64}}$, which exhibits an E_A for Ni self-diffusion of (0.76 $\pm$ 0.11) eV [2].

In order to analyze the structure-dynamics relation in more detail, the partial static structure factors of $\mathrm{Hf_{35}Ni_{65}}$ at 1510 and 1615 K (see ref. [6]) were used as an input for mode coupling theory (MCT) to calculate Hf and Ni self-diffusion coefficients (green full symbols in Fig. 1) [6]. The deviation of MCT from the QENS results on the absolute scale is a result of the fact that the temperature enters only as an indirect parameter in MCT calculations. This has been discussed in Ref. [5] in detail for $\mathrm{Zr_{50}Ni_{50}}$. Remarkably, MCT and QENS results for $\mathrm{Hf_{35}Ni_{65}}$ in Fig. 1 show a similar temperature dependence and thus a roughly identical E_A.

Despite very small changes in the partial static structure factors caused by the temperature increase of about 105 K, MCT can accurately reproduce the activation energy of the diffusion coefficients. The remarkably good agreement of activation energies between QENS and MCT results has also been observed for $\mathrm{Zr_{50}Ni_{50}}$ by a temperature increase over 220 K [5]. Moreover, the dynamical decoupling observed by QENS, i.e., Ni atoms diffuse faster than Hf atoms, can be reproduced by the MCT calculations as well (see Fig. 1). The decoupling found in the MCT results ($D_\mathrm{Ni}/D_\mathrm{Hf}$ = 1.8) is close to the experimental QENS results, which reveal a decoupling of roughly a factor of 2. From this we conclude that although static partial structure factors only provide space- and time-averaged structural information of the alloy melt, they are sufficient to reveal the dynamical decoupling of the diffusion coefficients as well as the activation energy for self-diffusion when serving as an input for MCT.

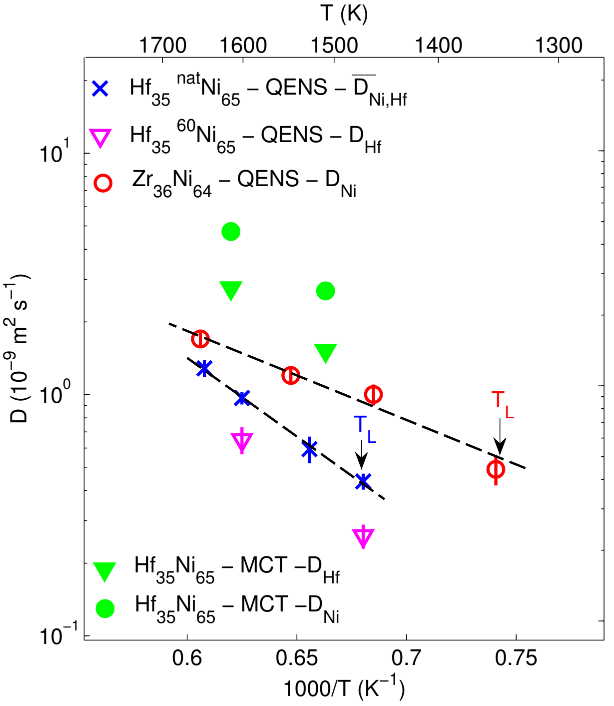

FIG. 1: Hf and Ni self-diffusion coefficients of liquid $\mathrm{Hf_{35}Ni_{65}}$ [6] and $\mathrm{Zr_{36}Ni_{64}}$ [2] determined by QENS or calculated from measured partial structure factors by using MCT [6].

* Corresponding author: `dirk.holland-moritz@dlr.de`

[1] D. Holland-Moritz et al., PRB **79**, 064204 (2009).
[2] D. Holland-Moritz et al., J. Phys. Conf. Ser. **144**, 012119 (2009).
[3] T. Kordel et al., PRB **83**, 104205 (2011).
[4] S. W. Kordel et al., PRB **95**, 024301 (2017).
[5] B. Nowak et al., Phys. Rev. Materials **1**, 025603 (2017).
[6] B. Nowak et al., PRB **96**, 054201 (2017).

Mixing effects in a ternary Hf-Zr-Ni metallic melt

B. Nowak,[1],* D. Holland-Moritz,[1] F. Yang,[1] Z. Evenson,[2] and A. Meyer[1]

[1]Institut für Materialphysik im Weltraum, Deutsches Zentrum für Luft- und Raumfahrt (DLR), 51170 Köln, Germany
[2]Heinz Maier-Leibnitz Zentrum (MLZ) and Physik Department, Technische Universität München, 85748 Garching, Germany

The glass-formation process in metallic melts is controlled by many physical properties such as atomic size differences, packing fractions and competing chemical interactions. In order to investigate the impact of these features on the dynamical behavior, which is also a key paramter for the glass-formation process, we studied the ternary melt $\mathrm{Hf}_{10}\mathrm{Zr}_{25}\mathrm{Ni}_{65}$ through measurements of self-diffusion coefficients as well as viscosity. The results are compared to those for the binary melts $\mathrm{Hf}_{35}\mathrm{Ni}_{65}$ and $\mathrm{Zr}_{36}\mathrm{Ni}_{64}$ [1, 2]. The advantage of investigating binary/ternary Hf-/Zr-Ni melts is that we are able to analyze the impact of addition of alloy components on the dynamical behavior at nearly constant measured packing fraction, consequently reducing the number of different physical parameters under consideration. We substitute only small amounts of melt components that are characterized by a nearly identical atomic size (Zr by Hf), but are known to have different chemical interactions with the smaller Ni atoms, as evidenced by the different chemical short-range order present in the constituent binary systems [1].

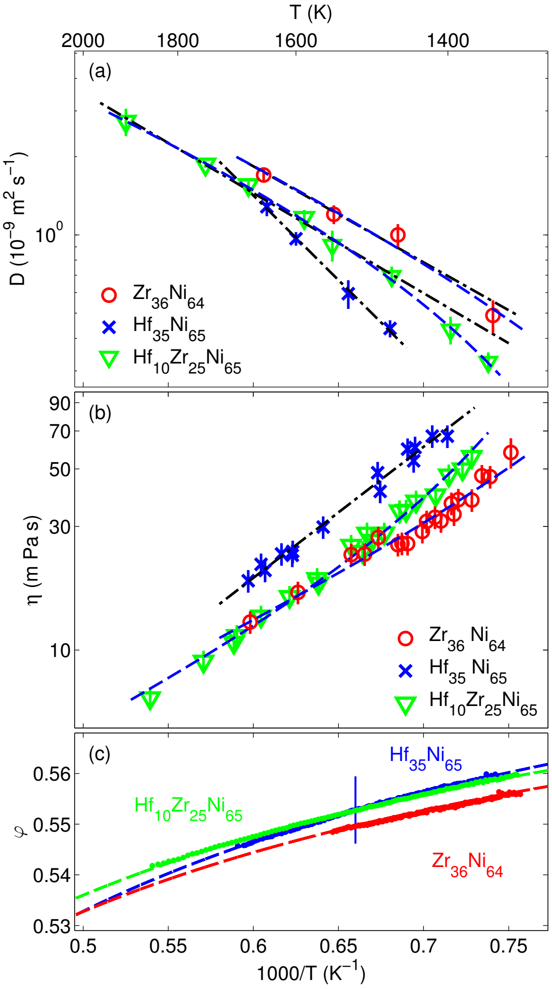

FIG. 1: (a) Self-diffusion coefficients for $\mathrm{Hf}_{35}\mathrm{Ni}_{65}$ [1], $\mathrm{Zr}_{36}\mathrm{Ni}_{64}$ [2] and $\mathrm{Hf}_{10}\mathrm{Zr}_{25}\mathrm{Ni}_{65}$ measured by quasielastic neutron scattering (QENS). The black dashed-dotted lines represent the Arrhenius fit and the blue dashed lines the scaling law fit of MCT. (b) Measured viscosity for $\mathrm{Zr}_{36}\mathrm{Ni}_{64}$ [3], $\mathrm{Hf}_{35}\mathrm{Ni}_{65}$ and $\mathrm{Hf}_{10}\mathrm{Zr}_{25}\mathrm{Ni}_{65}$ by using the oscillating drop technique in an electrostatic levitator. The black dashed-dotted line represents the Arrhenius fit and the blue lines the scaling law fit of MCT. (c) Packing fraction for $\mathrm{Zr}_{36}\mathrm{Ni}_{64}$, $\mathrm{Hf}_{35}\mathrm{Ni}_{65}$ [1] and $\mathrm{Hf}_{10}\mathrm{Zr}_{25}\mathrm{Ni}_{65}$. The blue vertical line reflects the experimental error of the measurement.

As a result of the incremental substitution of Zr by Hf, we identified a reduced measured self-diffusion coefficient and a higher melt viscosity (see Fig. 1 (a) and (b)). The self-diffusion coefficient of ternary $\mathrm{Hf}_{10}\mathrm{Zr}_{25}\mathrm{Ni}_{65}$ melt, which exhibits a deviation from Arrhenius behavior $D(T) = D_0 \exp[-E_A/(k_B T)]$ over a studied temperature range of 550 K (black dashed-dotted line in panel (a)), can be accurately described by the scaling-law of mode-coupling theory (MCT) of the glass-transition $D(T) \propto [(T-T_c)/T_c]^\gamma$ with the critical exponent $\gamma_D^{\mathrm{Hf}_{10}\mathrm{Zr}_{25}\mathrm{Ni}_{65}} = 1.6 \pm 0.2$ and the critical temperatur $T_c^{textHf_{10}\mathrm{Zr}_{25}\mathrm{Ni}_{65}} = 1165$ K. The measured viscosities follow a MCT scaling-law with almost equal parameters as for the self-diffusion ($\gamma_\eta^{\mathrm{Hf}_{10}\mathrm{Zr}_{25}\mathrm{Ni}_{65}} = 1.77 \pm 0.03$) (blue dashed lines in panel (a) and (b)). Although we only substitute alloy components with a nearly equal atomic size and the measured overall packing fraction remains almost unchanged (see Fig. 1 (c)), the dynamics in $\mathrm{Hf}_{10}\mathrm{Zr}_{25}\mathrm{Ni}_{65}$ are slower compared to $\mathrm{Zr}_{36}\mathrm{Ni}_{64}$ at lower temperatures. This corresponds also to a higher critical temperature T_c for $\mathrm{Hf}_{10}\mathrm{Zr}_{25}\mathrm{Ni}_{65}$ in comparison to $\mathrm{Zr}_{36}\mathrm{Ni}_{64}$ ($T_c^{\mathrm{Zr}_{36}\mathrm{Ni}_{64}} \approx 1000$ K) and might be induced by additional chemical interactions in the melt. Since in the past a higher reduced glass transition temperature T_{rg}=T_{g}/T_{textL} has been positively correlated to the glass-forming ability [4], we have calculated a reduced critical temperature T_{textrc}=T_c/T_{textL} while assuming, in a first approximation, a linear relation between T_c and T_{g}. As a result of the significantly smaller difference between liquidus and critical temperature $\Delta T_{\mathrm{LC}} = T_{\mathrm{L}} - T_c$ for the ternary melt in comparison with $\mathrm{Zr}_{36}\mathrm{Ni}_{64}$, T_{rc} increases from $T_{\mathrm{rc}}^{\mathrm{Zr}_{36}\mathrm{Ni}_{64}}$=0.75 to $T_{\mathrm{rc}}^{\mathrm{Hf}_{10}\mathrm{Zr}_{25}\mathrm{Ni}_{65}}$=0.83, which may favor the glass-formation in the $\mathrm{Hf}_{10}\mathrm{Zr}_{25}\mathrm{Ni}_{65}$ melt [5].

---

* Corresponding author: `benedikt.nowak@dlr.de`

[1] B. Nowak et al., PRB **96**, 054201 (2017).
[2] D. Holland-Moritz et al., J. Phys. Conf. Ser. **144**, 012119 (2009).
[3] P. Heintzmann et al., APL **108**, 241908 (2016).
[4] A. Peker et al., APL **63**, 2342 (1993).
[5] B. Nowak et al., submitted to PRB.

Combined Interdiffusion and Self- Diffusion Analysis in Al-Cu Liquid Diffusion Couple

I.V. Belova,[1] D. Heuskin,[2] E. Sondermann,[2,*] B. Ignatzi,[2] F. Kargl,[2] G.E. Murch,[1] and A. Meyer[2]

[1] *University of Newcastle, Australia*

[2] *Institut für Materialphysik im Weltraum, Deutsches Zentrum für Luft- und Raumfahrt (DLR), 51170 Köln, Germany*

Recently, a combined isotope (tracer) and interdiffusion theoretical approach was developed [1] for application to solid state interdiffusion couples with an addition of an enriched isotope layer in a sandwich-type configuration. The resulting expressions allow for obtaining the self (tracer) diffusion coefficients of the atomic components corresponding to the enriched isotopes. Importantly, these diffusion coefficients are obtained as functions of composition in the diffusion zone. This analysis has been adapted to the case of liquid alloys.

Shear-cell interdiffusion experiments with a layer enriched in ^{65}Cu sandwiched between the interdiffusion couple ends have been performed on liquid Al-Cu that is suitable for demonstration of the application of this analysis. (Note that the analysis is not limited to the use of the shear-cell technique.)

The shear-cell experimental set up in a high temperature isothermal furnace (details are given in [3]) was designed to capture the simultaneous isotope diffusion and interdiffusion process in a liquid Al-Cu diffusion couple. The combined, sandwich type, sequence of phases in the initial state was: Al-Cu10at% - Al-^{65}Cu12.5at% - Al-Cu15at%. This sequence ensures a stable density layering which reduces convective flow.

In total, three experiments have been performed at a target temperature of 973 K. The self diffusion coefficient of copper in a Al-Cu alloy at compositions between 10at% and 15at% of Cu was analysed by using the following equation:

$$D^*_{Cu} = -\left(\frac{(x+a)}{2t} + \tilde{D}\frac{dlnc_A}{dx}\right) / \left(\frac{dln(c_{A1}/c_A)}{dx}\right) \tag{1}$$

Here, D^*_{Cu} is the self diffusion coefficent of copper and $\tilde{D}$ the interdiffusion coefficient, x denotes the position, c_A the concentration of component A and c_{A1} the excess of isotopes A1 above the natural occurrence.

Fig. 1 shows results of the application of Eq. 1 to the interdiffusion profiles and the ratios $(c_{^{65}Cu} - kc_{\mathrm{Cu}})/c_{\mathrm{Cu}}$. For all three experiments the resulting self-diffusion coefficients, shown by solid lines, slightly decrease with an increase in concentration.

Exp 1 was considered to have been the best one from an experimental point of view. The best fit of the interdiffusion profile was achieved with $\tilde{D} = 2.5 \times 10^{-9}$m^2/s. Due to uncertainties in concentration measurements, there is a large uncertainty of up to $\pm 1.6 \times 10^{-9}$m^2/s for the interdiffusion coefficients. The results for the concentration-dependent self-diffusion of Exp 1 give a very good agreement with the independently measured self-diffusion coefficient of AlCu12.5at%.

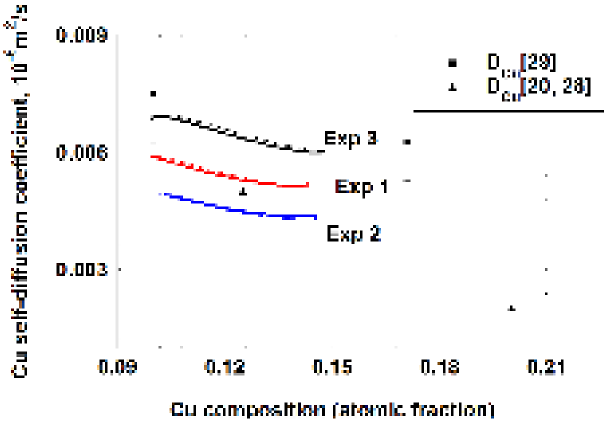

FIG. 1: Results of combined isotopic and interdiffusion analysis where a constant interdiffusion coefficient and corresponding error function for the interdiffusion profile were assumed. The Cu self-diffusion coefficient was calculated for all three experiments as a function of composition. The triangles represent results of independent QENS measurements on AlCu12.5at% and AlCu20at%. The squares represent results of QENS measurements by Dahlborg et al. Numbers in brackets denote references as given in [2].

The self-diffusion coefficients calculated as functions of composition have characteristic initial downward and final upward curvatures. This is usually accepted as the indication that the diffusion coefficient is becoming less reliable. This happens at the tails of the corresponding composition profiles where the intrinsic experimental error is the highest.

Remarkably, despite large uncertainties in the interdiffusion coefficients, uncertainties between the three experiments in the resulting self-diffusion coefficients are small, with a maximum of about 17%. In addition, the new analysis were found to be in good agreement with independently measured Cu self (tracer) diffusion coefficient at two compositions. It can then be further concluded that the accuracy of the newly developed analysis is higher than its interdiffusion part.This should encourage application of the analysis to experiments in liquids where an isotope-enriched layer is combined with a concentration gradient to reduce convective flow.

---

[*] Corresponding author: `elke.sondermann@dlr.de`

[1] I.V. Belova, Y.H. Sohn and G.E. Murch, Phil. Mag. Lett. **95**, 416 (2015).

[2] I.V. Belova, D. Heuskin, E. Sondermann, B. Ignatzi, F. Kargl, G.E. Murch and A. Meyer, Scripta Mater. **143**, 40 (2018).

[3] D. Heuskin, F. Kargl, A. Griesche, Ch. Stenzel, D. Mitschke, D. Brauer and A. Meyer, J. Phys. Conf. Ser. **327**, 012053 (2011).

Mismatch of viscosity in bulk metallic forming melts

I. Jonas,[1] F. Yang,[1,*] W. Hembree,[2] R. Busch,[2] and A. Meyer[1]

[1]*Institut für Materialphysik im Weltraum, Deutsches Zentrum für Luft- und Raumfahrt (DLR), 51170 Köln, Germany*
[2]*Chair of Metallic Materials, Saarland University, 66123 Saarbrücken, Germany*

Knowledge of the temperature dependent dynamics of glass forming liquids, particularly over a large temperature interval, is not only important for many physical phenomena in liquids, but also for manufacturing processes of these materials. One of the most commonly probed thermophysical properties reflecting the liquid dynamics is the melt viscosity. The sensitivity of the dynamics of different melts with respect to temperature changes can be therefore compared semi-quantitatively, using a modification of the empirically Vogel-Fulcher-Tammann (VFT) equation as:

$$\eta(T) = \eta_0 \exp(\frac{D^* T_0}{T - T_0}), \tag{1}$$

where η_0 is the viscosity at infinitely high temperature, D^* is the fragility parameter, and T_0 is the VFT-temperature at which the viscosity diverges.

The origin of different fragility is not well understood so far. Moreover, it has been observed recently in a number of bulk metallic glass (BMG) forming melts that, even in the same liquid the fragility parameter can change depending on the temperature. Such fragile-to-strong (F-S) crossover has been associated with a liquid-liquid transition, which has been proposed to be a general feature of BMG or even of the liquid state.

Systematic investigation of such F-S crossover requires reliable viscosity measurements covering large temperature range. Thus, we investigated a series of ternary, quaternary, and five-component Zr-based glass forming alloys $Zr_{60}Cu_{25}Al_{15}$ (Inoue3), $Zr_{65}Cu_{17.5}Ni_{10}Al_{7.5}$ (Inoue4), $Zr_{52.5}Cu_{17.9}Ni_{14.6}Al_{10}Ti_5$ (Vit105), $Zr_{57}Cu_{15.4}Ni_{14.6}Al_{10}Nb_5$ (Vit106), $Zr_{58.5}Cu_{15.6}Ni_{12.8}Al_{10.3}Nb_{2.8}$ (Vit106a), as well as a Ti-Cu based metallic glass former $Ti_{34}Zr_{11}Cu_{47}Ni_8$ (Vit101). High temperature viscosity in the range of about T_l±200 K has been measurement employing electrostatic levitation (ESL) using oscillating droplet techniques, which allows accessing the undercooled state. Low temperature viscosity close to the glass transition temperature (T_g) has been obtained via three-point beam bending method. The results are shown in Fig. 1 on a reduced temperature scale T_g/T (Angell plot [1]). For comparison, the melt viscosity of the Vit1 ($Zr_{41.2}Ti_{13.8}Cu_{12.5}Ni_{10}Be_{22.5}$) and Vit4 ($Zr_{46.8}Ti_{8.2}Cu_{7.5}Ni_{10}Be_{27.5}$) alloys are shown as well. Particularly in the case of Vit1 a F-S transition has been observed previously in the equilibrium melt viscosity, measured by Couette rheometer [2].

The low temperature viscosities of all the studied alloys fall almost on top of each other when scaled with the corresponding T_g. This shows that the sensitivities of the liquid viscosity against temperature change are very similar for these melts, including the TiCu-based composition Vit101 (solid line in Fig. 1). Indeed, the obtained low temperature fragility parameters D^* vary only within a narrow range. In the high temperature regime close to the liquidus temperature the composition dependence of the melt viscosity is more pronounced. The span of the viscosity on the T_g/T scale is larger, particularly the viscosity of the Vit101 alloy is about a factor of 2 lower.

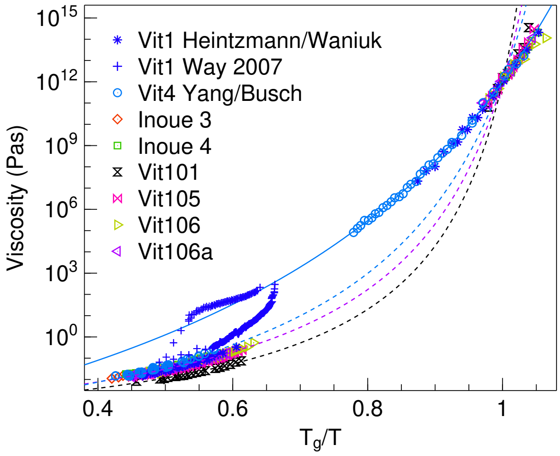

FIG. 1: Temperature dependent liquid viscosity of the studied metallic glass forming alloys including both the high temperature and low temperature regimes. The viscosity of the Be-containing alloy Vit1 and Vit4 are also shown for comparison [2–4]. Solid and dashed lines are fit curves according to eq. 1

Independent of the composition dependence, it can be seen that for the alloys studied, if the low temperature viscosity is extrapolated to high temperature, it overestimates the high temperature viscosity by more than one order of magnitude. Similarly trend can be observed for the low temperature viscosity (dashed lines in Fig. 1). Although there might be measurement techniques dependent deviations between the results of the Couette rheometer and ESL, the mismatch between the two temperature regime is considerably larger than that. Apparently, even for alloys like Vit4 where no F-S crossover has been reported, such phenomena seem to be rather common for metallic glass forming melts.

[*] Corresponding author: `fan.yang@dlr.de`

[1] C. A. Angell, Science, **267**, 1924 (1995)
[2] C. Way, P. Wadhwa, R. Busch, Acta Mater., **55**, 2977, (2007)
[3] P. Heintzmann, F. Yang, S. Schneider, G. Lohöfer, A. Meyer, Appl. Phys. Lett., **108**, 241908 (2016); T. A. Waniuk, R. Busch, A. Masuhr, W. L. Johnson, Acta Mater., **46**, 5229 (1998)
[4] F. Yang, T. Unruh, A. Meyer, Europhys. Lett., **107**, 26001 (2014); R. Busch, E. Bakke, W. L. Johnson, Acta Mater., **46**, 4725 (1998)

Industrial grade versus scientific pure: Influence on melt properties

I. Jonas,[1,*] W. Hembree,[2] R. Busch,[2] and A. Meyer[1]

[1] *Institut für Materialphysik im Weltraum, Deutsches Zentrum für Luft- und Raumfahrt (DLR), 51170 Köln, Germany*
[2] *Chair of Metallic Materials, Saarland University, 66123 Saarbrücken, Germany*

Fundamental research on bulk metallic glasses (BMGs) emanates mostly from high purity starting materials. However, the purity of the starting materials is an important cost driver for applications. Industrial grade metals are usually inexpensive, but contain substantially more impurities [1]. For industrial applications of BMGs it is thus important to find out whether using starting materials containing a higher amount of impurities and in particular oxygen affects the properties of the melt and thus influences the production process.

In order to gain insight into this issue we studied two different degrees of purity of the bulk metallic glass AMZ4. High purity AMZ4 ($Zr_{59.3}Cu_{28.8}Al_{10.4}Nb_{1.5}$) was processed from 99.9 % to 99.99 % pure metals, while industrial AMZ4 ($Zr705_{60.8}Cu_{20.8}Al_{10.4}$) replaces the high purity Zirconium and Niobium with the inexpensive industrial grade pre-alloy Zr R60705 [2], which consists of 95.5 % Zirconium and Hafnium (with a maximum of 4.5 % Hafnium). Additionally this pre-alloy contains approximately 1 at% oxygen [3].

In order to investigate the influence of impurities and in particular that of oxygen in starting materials viscosity measurements were performed using different measurement methods. These methods are Couette rheometry, electrostatic and electromagnetic levitation (ESL and EML) experiments in combination with the oscillating drop technique. The EML measurements were conducted under reduced gravity (μg) conditions in the TEMPUS facility. Results are shown in figure 1.

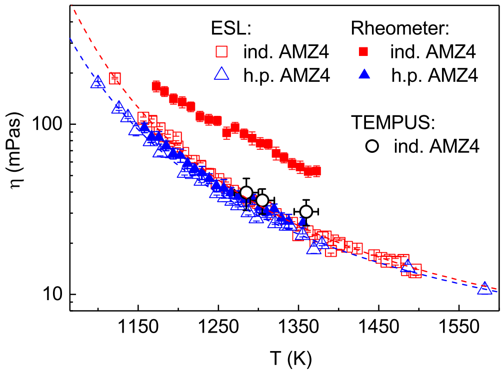

FIG. 1: Melt viscosities of industrial and high purity AMZ4 determined by Couette rheometry as well as by electrostatic and electromagnetic levitation in combination with the oscillating drop technique and the latter under reduced gravity conditions in the TEMPUS facility.

Couette rheometer results cover a temperature range of around 200K and a viscosity range of 20mPas to 175mPas. Industrial and high purity AMZ4 differ in absolute viscosity by a factor of approximately 2. ESL results cover a temperature range of around 400K and a viscosity range from 15mPas to 200mPas. Within the ESL results only a small difference between the viscosity of industrial and high purity AMZ4 is found in contrast to Couette rheometer results. Couette and ESL data for high purity AMZ4 coincide with each other. Viscosity data for industrial AMZ4 obtained in the TEMPUS facility coincides with ESL data.

ESL measuring artefacts can be ruled out because individual measurements consist of different sample masses between 50 mg and 100 mg and artefacts would become visible in a mass dependency. Additional TEMPUS data measured on a 1.5 g sample confirm that even a mass variation over an order of magnitude gives identical results. Couette rheometer data showed no systematic difference in viscosity at different shear rates, therefore only data measured at 456 s^{-1} are displayed.

Yet, viscosities determined by rheometry crucially depend on interactions between melt and container material. It is known that if a graphite crucible is used, usually a stable zirconium carbide (ZrC) layer forms at the interface between melt and the shear cell [4], which remains stable at thicknesses below 10 μm and acts as diffusion barrier [4] so that no further melt reactions take place. It is likely that in the case of industrial AMZ4, oxygen dissolved in the melt affects the stability of this ZrC layer and thus modifies the diffusion behavior. Observations by the authors, where pieces of ZrC were entrained within the melt after the experiment support the assumption that the ZrC layer was not sufficiently stable at a relatively high oxygen content. Moreover, the presence of impurities and oxygen might also change the wetting behavior of the melt and thus, affect the measurement results. For high purity AMZ4 such a reaction is less problematic since the alloy contains less oxygen. Thus, the higher viscosity of industrial AMZ4 measured by Couette rheometer is an artefact of the measurement and attributed to reactions between melt and shear cell. However, our ESL and TEMPUS measurements show that oxygen, even at a level of 1 at% does not significantly alter the melt property viscosity of the BMG AMZ4. Therefore, special care must be taken when using conventional measurement methods to determine melt properties of bulk metallic glass forming alloys.

We gratefully acknowledge the Deutsche Forschungsgemeinschaft (DFG) for funding through grant No. ME 1958/11-2 and BU 2276/6-2.

---

[*] Corresponding author: `isabell.jonas@dlr.de`

[1] D.V. Louzguine-Luzgin, Intermetallics **18**, 1531 (2010)
[2] J. Heinrich et al., Appl. Phys. Lett. **100**, 071909 (2012)
[3] J. Heinrich et al., Intermetallics **25**, 1-4 (2012)
[4] C. Way et al., Acta Mat. **55**, 2977 (2007)

1.3 Solidification, Nucleation and Growth

Transient nucleation and microstructural design in flash-annealed bulk metallic glasses

K. Kosiba,[1] S. Scudino,[1] R. Kobold,[2,*] U. Kühn,[1] A.L. Greer,[3] J. Eckert,[1,4] and S. Pauly[1]

[1]*IFW Dresden, Institut für Komplexe Materialien, Helmholtzstraße 20, 01069 Dresden, Germany*
[2]*Institut für Materialphysik im Weltraum, Deutsches Zentrum für Luft- und Raumfahrt (DLR), 51170 Köln, Germany*
[3]*Department of Materials Science and Metallurgy, 27 Charles Babbage Road, University of Cambridge, Cambridge CB3 0FS, United Kingdom*
[4]*TU Dresden, Institut für Werkstoffwissenschaft, Helmholtzstraße 7, 01069 Dresden, Germany*

The high cooling rates required for vitrification of metallic melts guarantee that the structure of the liquid is preserved while the melt gradually transforms into a solid [1]. Due to their inherent metastability, metallic glasses crystallize upon thermal activation, which involves nucleation and growth. It is debatable, however, whether steady-state kinetics of crystal nucleation and growth apply when glasses are heated quickly. While transient nucleation is known to occur in metallic glasses during isothermal annealing [2], theoretical considerations predict a heating-rate dependent transient nucleation phenomenon during fast isochronal heating based on the dissolution of subcritical clusters.

The present experiments were conducted to (i) analyze heating-rate-dependent transient effects in metallic glasses heated at high rates and to (ii) assess the potential of flash-annealing for optimizing composite microstructures and thereby the resulting deformation behaviour.

Cu-Zr-based bulk metallic glasses (BMGs) were partially devitrified by flash-annealing at heating rates ranging from $0.08 - 180\,\mathrm{K\,s^{-1}}$. Immediate quenching after heating to predefined temperatures preserves the partially transformed microstructure and allows direct observation of crystallite sizes and numbers. The phase formation changes from eutectic to polymorphic at high heating rates due to kinetic constraints and uniformly dispersed metastable B2 CuZr crystals precipitate in the glass at heating rates faster than $16\,\mathrm{K\,s^{-1}}$ (Fig. 1). A beneficial side effect of this partially crystalline microstructure is a strongly enhanced room-temperature deformability. The analysis of crystal populations suggests that the nucleation rate of very fast heated supercooled liquids ($> 100\,\mathrm{K\,s^{-1}}$) is effectively lower than in the steady state. Transient effects slow down the nucleation kinetics and reduce the density of B2 CuZr crystals in the glass (Fig. 1). At a later stage of crystallization a distinct thermal front traverses the flash-annealed specimens. This front cannot be attributed to the movement of a crystal-liquid interface as is the case for electrostatic levitated supercooled liquids. It arises due to the concerted growth of crystals in a restricted volume accompanied by thermal diffusion. Flash-annealing of BMGs not only permits to tailor the microstructure of BMG-composites in order to overcome their intrinsic brittleness, but also to study fundamental crystallization processes in highly undercooled melts.

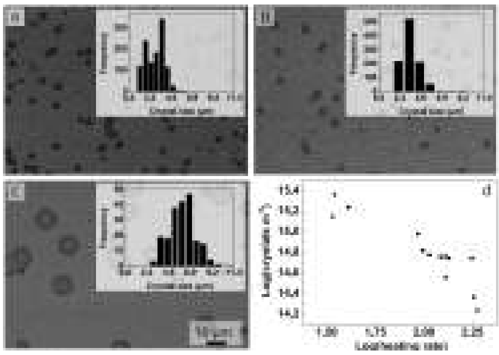

FIG. 1: Microstructural analysis of $\mathrm{Cu_{44}Zr_{44}Al_8Hf_2Co_2}$ glass flash-annealed under different conditions. The SEM-micrographs were obtained after flash-annealing at rates of a: $\varphi = 35\,\mathrm{K\,s^{-1}}$, ejection temperature $T_{ej} = 910\,\mathrm{K}$; b: $\varphi = 129\,\mathrm{K\,s^{-1}}$, $T_{ej} = 927\,\mathrm{K}$ and c: $\varphi = 181\,\mathrm{K\,s^{-1}}$, $T_{ej} = 949\,\mathrm{K}$. The insets show the respective crystal diameter distributions; d: Crystal population density as a function of the heating rate. At higher φ, fewer crystals precipitate than expected for a steady-state nucleation process.

Since the composite microstructures obtainable by flash-annealing are highly reproducible, ultrafast thermal treatment of metallic glasses opens up new vistas for improving the damage tolerance of monolithic glasses. Detailed investigations on the effect of crystal size and crystal distribution on the deformation mechanism of the composite and the martensitic transformation in the B2 crystals [3] now become feasible. Even beyond the present alloy system, many interesting questions emerge: Can the microstructure of Ti-based or Zr-based BMGs, which form composites upon quenching, controlled in a similar manner? Can other families of materials, such as age-hardenable alloys in which nucleation and growth processes determine the microstructure and properties be optimized as well by flash-annealing? Ultrafast annealing of metastable alloys followed by immediate quenching generally appears as an interesting field of research with the potential to manipulate and tailor microstructures and properties in an unprecedented manner.

The authors thank B. Escher, I. Kaban, J. Orava, C. Rentenberger, K. K. Song, G.Wang, J. Wright and especially H. Wendrock and W. Loeser are thanked for stimulating discussions. This work was financed by the German Science Foundation (DFG) (grant PA 2275/ 2-1) and the Leibniz Program (grant EC 111/26-1).

* Corresponding author: `raphael.kobold@dlr.de`

[1] H.S. Chen et al., Rep. Prog. Phys., **43**, 353 (1980).
[2] K.F. Kelton et al., Solid State Phys., **45**, 75 (1991).
[3] T. Waitz et al., Acta Mater. , **52**, 5461 (2004)

Metastable phase formation in undercooled Nd-Fe-B alloy melts processed by electromagnetic levitation on ground and on board the ISS

T. Volkmann,[1,*] C. Kreischer,[1] J. Strohmenger,[1] D. Simons,[1] C. Karrasch,[2] J. Gao,[3] O. Shuleshova,[4] and W. Löser[4]

[1] *Institut für Materialphysik im Weltraum, Deutsches Zentrum für Luft- und Raumfahrt (DLR), 51170 Köln, Germany*
[2] *Raumfahrtmanagement, Deutsches Zentrum für Luft- und Raumfahrt (DLR), 53227 Bonn, Germany*
[3] *Key Lab of Electromagnetic Processing of Materials, Northeastern University, Shenyang, China*
[4] *Institut für Festkörperforschung, IFW Dresden, Dresden, Germany*

Nd-Fe-B alloys are used for the development of high-performance permanent magnets. The properties are based on the magnetically anisotropic ϕ-phase of the stoichiometric composition $Nd_2Fe_{14}B_1$ (see e. g. review article [1]). However, a metastable χ-phase of the composition $Nd_2Fe_{17}B_x$ (x ≈ 1) plays an important role during solidification and microstructural evolution. In undercooled $Nd_{18}Fe_{73}B_9$ alloy melts the primary crystallizing phase changes from stable ϕ-phase to metastable χ-phase with rising undercooling [2], which is due to a higher nucleation rate of the metastable phase above a critical undercooling level [3]. Due to the different compositions of the solid and the liquid formation of both ϕ- and χ-phase require distinct solute redistribution, i. e. mass transport in the liquid. Phase selection and the effect of melt convection have been investigated by electromagnetic levitation experiments and comparative tests under microgravity using the EML facility on board the ISS. Processing under normal gravity on ground requires strong levitation forces, which leads to strong turbulent fluid flow due to electromagnetic stirring. Microgravity allows to reduce electromagnetically induced fluid flow by one order of magnitude.

At small undercoolings the temperature-time profile of a sample processed under microgravity reveals two recalesence events, which are due to primary solidification of stable ϕ-phase followed by the stable η-phase ($Nd_1Fe_4B_4$) as expected from the equilibrium phase diagram [2] (Fig. 1). As the undercooling is increased solidification is initiated by the metastable χ-phase. The stable ϕ-phase is formed subsequently after a delay time of typically 5 s. Primary solidification of the metastable phase in the same sample processed on ground was observed at a much smaller undercooling as demonstrated in the left curve (black) in Fig. 1.

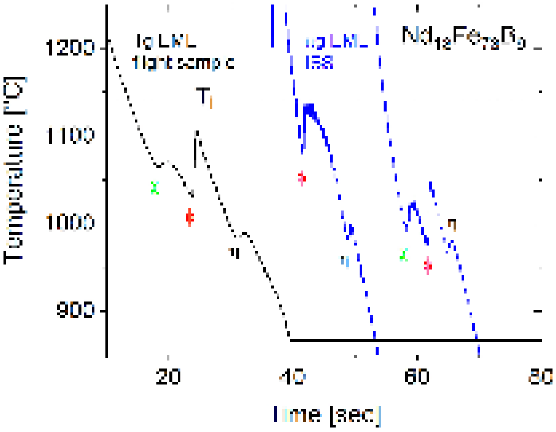

FIG. 1: Temperature-time profiles during solidification of the same $Nd_{18}Fe_{73}B_9$ sample processed on ground (black curve) and under microgravity in EML on board ISS (blue curves).

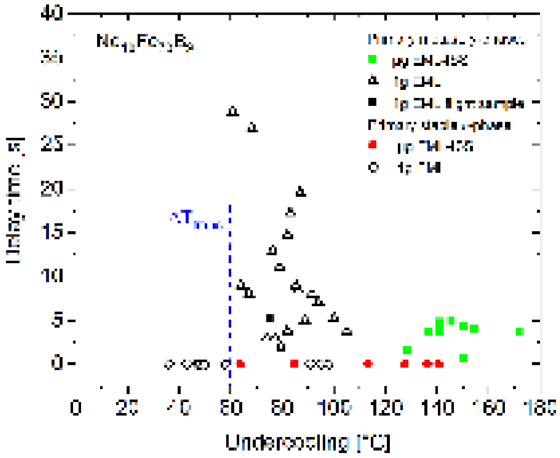

FIG. 2: Delay time between formation of metastable χ and stable ϕ-phase as function of undercooling measured in 1g EML and μg EML on board ISS.Recalescence events with primary stable ϕ-phase formation are indicated by a delay time of $\delta t = 0$. The critical undercooling ΔT_{trans} for the transition from primary stable ϕ to metastable χ-phase solidification is marked by vertical dashed lines. The data point (black, closed symbol) for the flight sample processed on ground is also included.

The plot of the delay time vs. undercooling measured in samples processed on ground yields a critical undercooling ΔT_{trans} of about 60 °C for the transition to metastable χ-phase solidification as displayed in Fig. 2. In the sample levitated under microgravity the transition occured at $\Delta T_{trans} \approx 130$ °C. Moreover, maximum undercooling of the melt prior to solidification was found to be 100 °C and 170 °C for 1g and μg EML tests, respectively. The phase selection behaviour observed under different fluid flow conditions on ground and in space is assumed to originate from the effect of concentrational exchange on the nucleation rate [4].

Financial support by ESA is gratefully acknowledged (project MAGNEPHAS, contract no. 4200014980).

---

[*] Corresponding author: `thomas.volkmann@dlr.de`

[1] R. F. Herbst, Rev. Mod. Phys. **63**, 819 (1991).
[2] G. Schneider, E. T. Henig, G. Petzow and H. H. Stadelmaier, Z. Metallkd. **77**, 755 (1987).
[3] J. Gao, T. Volkmann and D. M. Herlach, J. Alloys Compd. **350**, 344 (2003).
[4] K. F. Kelton Acta Mater. **48**, 1967 (2000).

Drendrite growth kinetics of fcc and bcc structured phases in undercooled melts

C. Kreischer,[1,*] C. Karrasch,[2] and T. Volkmann[1]

[1]*Institut für Materialphysik im Weltraum, Deutsches Zentrum für Luft- und Raumfahrt (DLR), 51170 Köln, Germany*
[2]*Raumfahrtmanagement, Deutsches Zentrum für Luft- und Raumfahrt (DLR), 53227 Bonn, Germany*

Dendritic growth is one of the most important crystal growth modes controlling the evolution of the microstructure and, therefore, the materials properties in metallic alloys [1]. Key factors dominating both growth kinetics and dendritic morphology are the interface mobility and the dimensionless stability parameter σ^* that determines the dendrite tip radius. The interface mobility μ, also called kinetic coefficient, describes the atomic attachment rate defined by $v = \mu \cdot \Delta T_k$ where v is the normal velocity of the interface and $\Delta T_k = T_m - T_i$ (T_m: melting temperature, T_i: interface temperature) is the kinetic undercooling. Generally, the kinetic coefficient reveals a cristalline anisotropy, i.e. it depends on the crystal plane adjacent to the liquid. The stability parameter is determined by the anisotropy of the interfacial energy and the kinetic anisotropy as well.

In order to analyze the effect of crystal structure growth velocities in undercooled melts of pure Ni and Co, which solidify in fcc structure, and Fe melts forming a bcc structured phase, have been measured by electromagnetic levitation processing in combination with a high-speed video camera. Undercooled Fe-Co melts can solidify alternatively either into the stable fcc or the metastable bcc phase, which offers the opportunity to analyze growth kinetics of different crystallographic phases at the same alloy composition without chemical effects.

For calculation of the dendrite growth velocities by the LKT model [2] thermophysical data were taken from literature, whereas σ^* and μ were adjusted to the experiments. The slope of the $v(\Delta T)$ curve at low undercoolings sensitively depends on the choice of the stability constant whereas at large undercoolings the slope is dominated by the kinetic coefficient. It is derived that the stability constant σ* and the kinetic coefficient μ for Fe are distinct smaller than that for the fcc metals (Fig. 1). Similary, the interface mobility of the bcc phase in Fe-Co is more sluggish than that of the fcc phase (Fig. 2). However, with rising undercooling the measured growth velocities for Ni and Co exhibit a break at which the data deviate significantly from the model. Furthermore, a change of morphology of the macroscopic growth front from an angular shape, which is expected for dendritic growth, to a spherical shape is observed in the high-speed videos for Ni, Co and the fcc phase in Fe$_{40}$Co$_{60}$. A possible explanation is a transition from stable dendritic growth to a tip-splitting morphology at a critical velocity according to Bragard et al. [6]. However, change of both growth law and morphology was not detected for Fe and the bcc phase in Fe-Co alloys.

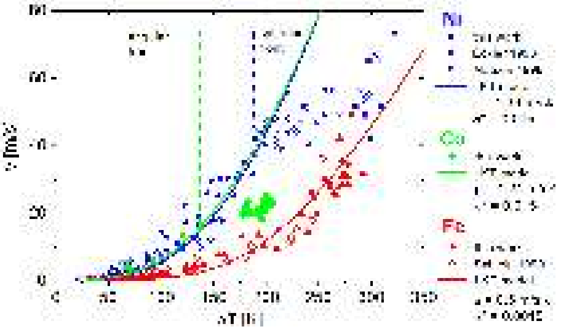

FIG. 1: Measured dendrite growth velocities of Ni, Co and Fe as function of undercooling together with calculated velocities according to the LKT model. The values for σ^* and μ used for modelling are included. Experimental data for Ni by Eckler et al. [3] and Matson [5] and data for Fe obtained by Schleip [4] are shown for comparison. The dashed lines mark the transition from angular to spherical growth front morphology for Ni (blue) and Co (green).

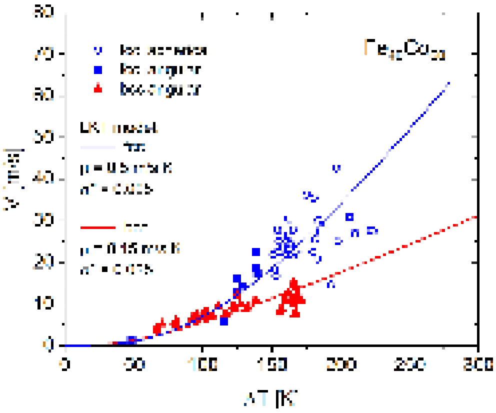

FIG. 2: Dendrite growth velocities of stable fcc and metastable bcc phase as a function of undercooling with respect to the corresponding liquidus temperature T$_L$(fcc) or T$_L$(bcc) in Fe$_{40}$Co$_{60}$ alloy melts.

Financial support by ESA is gratefully acknowledged (contract nos. 4200014980 and 4200020277).

* Corresponding author: `carolina.kreischer@dlr.de`

[1] W. Boettinger, S. R. Coriell, A. L. Greer, A. Karma, W. Kurz, M. Rappaz, and R. Trivedi, Acta Mater. **48**, 43 (2000).
[2] J. Lipton, W. Kurz, and R. Trivedi, Acta metall. **35**, 957 (1987).
[3] K. Eckler and D. M. Herlach, Mat. Sci. Eng. **A178**, 159 (1994).
[4] E. Schleip, PhD thesis, Ruhr University of Bochum, Bochum, Germany
[5] D.M. Matson, in: *Solidification 1998*, The Minerals, Metals & Materials Society (1998) pp. 233-244.
[6] J. Bragard, A. Karma, Y. H. Lee, and M. Plapp, Interface Sci. **10**, 121 (2002).

Solidification velocity and delay time of undercooled Fe-Ni alloys

C. Kreischer* and T. Volkmann

Institut für Materialphysik im Weltraum, Deutsches Zentrum für Luft- und Raumfahrt (DLR), 51170 Köln, Germany

To study the solidification process of a metallic alloy is the precondition to be able to understand, predict and influence the materials properties. The solidification process of Fe-Ni alloys is very similar to the one of Fe-Co [1] or Fe-Cr-Ni [2]: In all systems crystallization evolves via a double-step process if starting from an undercooled melt. A metastable δ-phase (bcc structure) can be formed prior to the equilibrium γ-phase (fcc structure). The two parameters that determine the solidification process are the dendrite tip growth velocities and the delay time between the nucleation of the metastable and the stable phase.

We measured growth velocities and the delay time of $Fe_{90}Ni_{10}$ with the electromagnetic levitator (EML). Samples of 6.5 mm diameter were melted, undercooled and solidified. Videos of the solidification were recorded by a high-speed camera with 75000 fps.

We analyzed three different growth velocities, namely the one of the metastable δ-phase, the one of the stable γ-phase growing in the mushy zone of δ and the one of the stable phase growing into the undercooled melt. They are shown in Fig.1 as a function of the undercooling with respect to the equilibrium liquidus temperature.

The driving force for crystallization is the undercooling with respect to the liquidus temperature T_L of the crystallizing phase. Since T_L of the metastable phase is always smaller, the effective undercooling and the growth velocity of the δ-phase is smaller. In the mushy zone the temperature is constant at $T_{L(\text{metastable})}$, independent of the primary undercooling. Consequently, γ always grows with the same velocity within the mushy zone of δ.

The delay time between the nucleation of the δ- and the γ-phase is displayed in Fig.2 with a logarithmic scale in dependence of the primary undercooling. The delay time lies in the range of milliseconds and decreases with increasing undercooling. This behavior was unexpected since γ nucleates in the mushy zone where the thermodynamic driving force for nucleation is constant. Other catalytic effects such as the dendrite shape or the amount of dislocation in the preexisting solid are possible reasons for the dependence of the primary undercooling of the delay time.

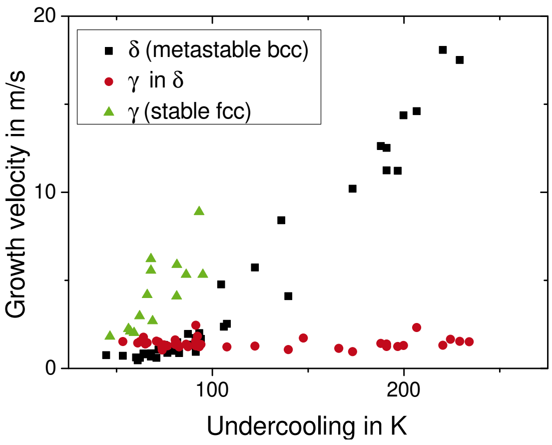

FIG. 1: Measured growth velocities of $Fe_{90}Ni_{10}$ in dependence of undercooling with respect to the equilibrium melting temperature.

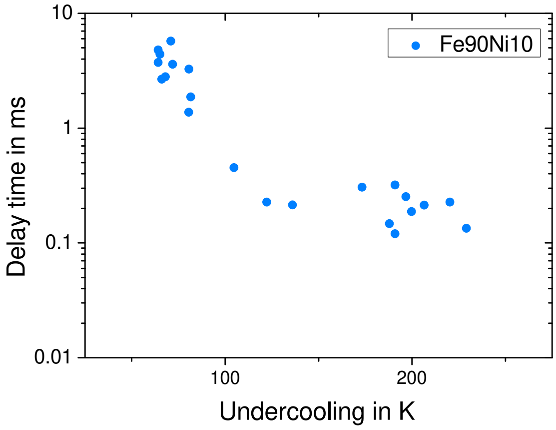

FIG. 2: The delay time of $Fe_{90}Ni_{10}$ in dependence of undercooling with respect to the equilibrium melting temperature.

To sum it up, the growth velocities of the δ- and the γ-phase in the melt as well as the delay time depend on the primary undercooling. The processes within the mushy zone, namely the nucleation of the the γ-phase which determines the delay time and the growth velocity of the γ-phase in the mushy zone show contrary behaviour: Whereas the growth velocity of the γ-phase in the mushy zone is independent of the primary undercooling, the delay time varies with the undercooling. The same behaviour was observed for Fe-Co alloys.

Obviously the described solidification process with double step recalescence is common among different sample systems. It lastly influences the microstructure and the materials properties. It is crucial to study this process in order to transfer knowledge to more complicated alloys, e.g. steels used in industry.

Financially support by the European Space Agency within the project "Magnephas" under contract no. 4200014980 is gratefully acknowledged.

* Corresponding author: `carolina.kreischer@dlr.de`

[1] J. Rodriguez, C. Kreischer, T. Volkmann and D. Matson, Acta Mater. **122**, 431 (2017).

[2] T. Volkmann, W. Löser and D.M. Herlach Met. Mat. Trans. A **28A**, 469 (1997).

The poisoning mechanism of Germanium on the grain refiner system Al-5Ti-1B

Mareike Wegener,* M. Kolbe, M. Becker, and F. Kargl
Institut für Materialphysik im Weltraum, Deutsches Zentrum für Luft- und Raumfahrt (DLR), 51170 Köln, Germany

Grain refinement in Aluminum and its alloys has been widely studied over the last years. The understanding of the effectiveness of the grain refiner is one of the key questions to control the microstructure and predict chemical or mechanical material properties. A common method is the inoculation of the melt with Ti-B particles as heterogeneous nuclei [1]. However the efficiency of the so-called Al-Ti-B master alloys is strongly depending on the Aluminum alloy [2].

We use in-situ X-ray radiography to analyze the behavior of Al-5Ti-1B grain refiner in Aluminum based alloys, with a focus on the system Al-Ge. Thin Al-Ge samples, inoculated with different amount of Al-5Ti-1B grain refiner, have been solidified at different cooling rates between 0.1K/min and 15K/min. The in-situ X-ray radiography measurement technique enables the investigation of the grain density according to the cooling rate and the grain refiner potency. Microstructures were analyzed post-mortem by EDX and EBSD on a LEO 1530 VP scanning microscope.

The efficiency of the grain refiner increase with the cooling rate. With a higher cooling rate more inoculated particle get activated and a finer microstructure in the sample arises. For hypo-eutectic alloys of the system Al-Ge, similar to the system Al-Si [2] [3] ,a poisoning effect occurs, which means the grain refiner is less effective. Less particles provide nuclei for the growing grain. The poisoning effect increases with the added amount of Germanium. However, the grain refinement response of Al-Ge can be improved with greater additions of the Al-5Ti-1B master alloy [Fig. 1.]

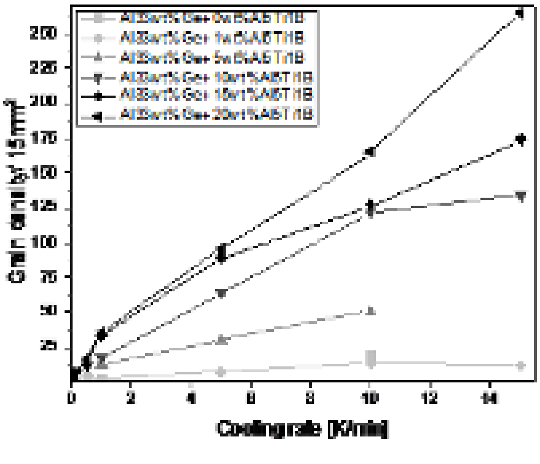

FIG. 1: Grain density as function of cooling rate. The results from in-situ experiments, performed using the near- isothermal furnace setup [4], measured after solidification, show that the grain density depends on the undercooling and the amount of added grain refiner.

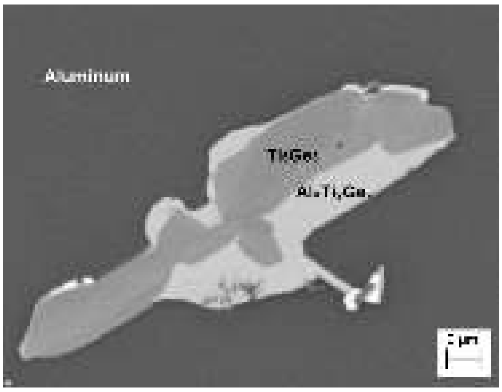

FIG. 2: SEM analysis of the grain refiner particles, embedded in the Al-based matrix. Different grey values indicate different Al-Ti-Ge-B layers. However not all layers could have been characterized with the EBSD analysis.

For a better understanding of this poisoning effect, the morphology of the grain refiner particle embedded in the Al-based matrix was studied. Different stable layers of Al-Ti-B-Ge with distinct crystal structures have been found and characterized [Fig. 2.] Usually the TiB_2 particle with a hexagonal crystal structure is coated by a Al_3Ti layer with a tetragonal crystal structure, allowing the cubic aluminum crystal to grow epitactically on the particle surface. With the increase of Germanium in the melt the formation of a Ti_5Ge_3 phase with hexagonal crystal structure and stoichiometric similar compositions with distinct crystal structures becomes more probable. Germanium replaces the aluminum in the coating layer more and more. The crystallographic interface matching between those layers and the aluminum melt is far from good. Hence, the grain refiner does not work very effectively, which is the so-called poisoning effect.

Further investigations on Al-Nb-B as master alloy are planned as recent studies [5] have shown that Al-Nb-B is an efficient inoculation alternative for the system Al-Si and show promising results for Al-Ge as well.

* Corresponding author: `mareike.wegener@dlr.de`

[1] A.L. Greer, P.S. Cooper, M.W. Meredtith, W. Schneider, P. Schumacher, J.A. Spittle and A. Tronche, Advanced Engineering Materials (2003).
[2] D. Qui, J.A. Taylor, M.X. Zhang, P.M. Kelly, Acta Materialia (2006).
[3] P. Schumacher, B.J. MCKay, Journal of Non-Crystal Solids 317 123-128 (2003).
[4] M. Becker, F. Kargl, D. Dreissigacker, S. Klein, Review of Scientific Instruments, 86 (2015).
[5] L. Bolzoni, N.H. Babu, Applied Materials Today, 5, 255-259 (2016).

Morphological transition of Al-dendrites in Al-Ge

M. Becker,[1,*] S.T. Wiese,[2] M. Kolbe,[1] and F. Kargl[1]

[1] *Institut für Materialphysik im Weltraum, Deutsches Zentrum für Luft- und Raumfahrt (DLR), 51170 Köln, Germany*
[2] *Gießerei-Institut, RWTH Aachen University, Intzestraße 5, 52072 Aachen, Germany*

Dendritic structures are very common in metallic metals produced by solidification. Most dendritic structures grow along directions corresponding to low index crystal axes, e.g. $\langle 100\rangle$, $\langle 110\rangle$ or $\langle 111\rangle$. Growth along different crystallographic directions results in variable dendrite morphologies which influences the solidification characteristics of a casting. To reliable predict microstrucutres, it is crucial to understand the selection principles governing dendritic growth patterns.

Cubic metals like fcc-aluminium usually grow along the crystallographic $\langle 100\rangle$ direction. However, in aluminium alloys variations in the primary fcc-aluminium growth directions are common [1]. These variations result from the weak anisotropy of the solid-liquid interfacial energy γ_{sl} of aluminium (about 1 %). Alloying elements with a different crystal structure can easily perturb the interfacial energy of aluminium that governs the crystal morphology for near-equilibrium solidification.

We focus on the Al-Ge system to investigate the influence of germanium-content on the morphology of Al-dendrites [2]. Germanium has a diamond crystal structure and a high anisotropy of the interfacial energy compared to aluminium. To ensure near-equlibrium solidification, we perform near-isothermal solidification experiments with a slow cooling rate of 1 °C/min. Thin samples ($\sim$200 μm) with germanium compostions of 10, 20, 25, 29 and 46 wt.% are investigated. We monitor the solidification process in-situ with X-ray radiography and determine the grain orientations using post-mortem electron-backscattered diffraction (EBSD).

We find three main primary dendrite arm growth directions: a) $\langle 100\rangle$, b) $\langle 110\rangle$ and c) a combination of both directions. Dendrite arms in the 20 wt.% Ge alloy grow exclusively along the crystallographic $\langle 100\rangle$ direction, whereas dendrite arms in the 46 wt.% Ge alloy grow along the crystallographic $\langle 110\rangle$ direction. These results indicate that a dendrite orientation transition (DOT) takes place in the Al-Ge system. The alloys of intermediate germanium concentrations show a variety of dendrite growth directions. Dendrites growing in the Al-25 wt.% Ge alloy most commonly show a combination of $\langle 100\rangle$ and $\langle 110\rangle$ growth directions. In the Al-29 wt.% Ge alloys the dendrites tend to grow along the $\langle 110\rangle$ crystallographic direction. In Fig. 1 a radiograph of an Al-29 wt.% Ge alloy is depicted showing dendrite growth directions of type b) and c).

We conclude that the DOT is not abrupt and that a transition zone over a wide range of compositions exists. This finding is in line with studies on the Al-Zn system, where a transition from the $\langle 100\rangle$ to the $\langle 110\rangle$ direction was found between an alloy composition of 20 wt.% Zn and 55 wt.% Zn [3]. However, with increasing Zn-content the dendrite growth directions changes continously between $\langle 100\rangle$ and $\langle 110\rangle$ which is different to our findings. As the studies on Al-Zn base on directional solidification experiments, the comparability to our study is, however, limited.

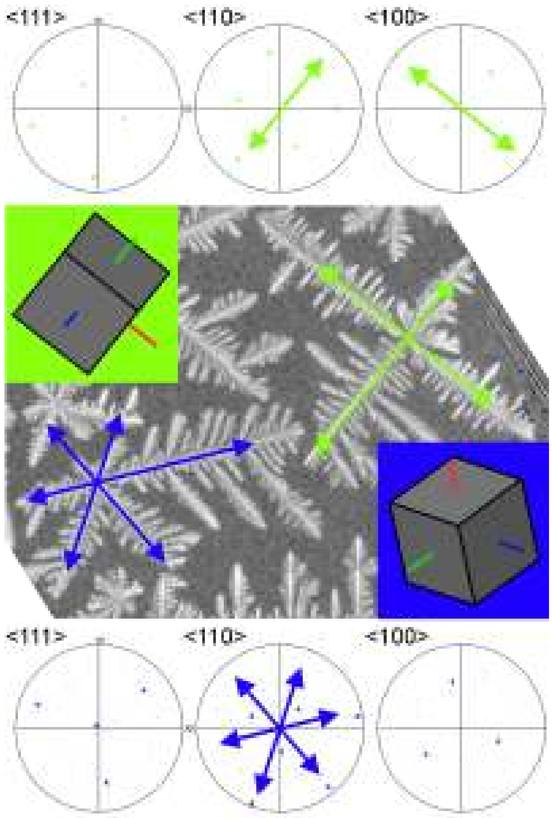

FIG. 1: X-ray radiography image of an Al-29 wt.% Ge alloy. In the 2D-projection dendrites with four and six primary arms develop. EBSD pole figures show the crystal orientations of the dendrites. The arrows indicate the crystallogrpahic growth directions of the primary dendrite arms.

In the Al-10 wt.% Ge alloy dendrites with variable growth directions are observed. This growth behaviour is unexpected and further studies are planned to find an explanation. Additionally, the influence of undercooling on the dendrite morphology must be investigated as a dependence on growth rates is suspected.

[*] Corresponding author: `maike.becker@dlr.de`

[1] S. Henry, T. Minghetti, M. Rappaz, Acta Mater. **46**, 6431-6443 (1998)

[2] S.T. Wiese, Morphologischer Dendriten Übergang von Al-Ge Legierungen, Bachelor Thesis, RWTH Aachen University (2017)

[3] J. Friedli, J. Fife, D. Di Napoli, M. Rappaz, Metall. Mater. Trans. A **44**, 5522-5531 (2013)

The ZrNi droptube experiment

P. Fopp,* R. Kobold, M. Kolbe, W. Hornfeck, and F. Kargl
Institut für Materialphysik im Weltraum, Deutsches Zentrum für Luft- und Raumfahrt (DLR), 51170 Köln, Germany

Intermetallic alloys have many industrial applications as high temperature materials, e. g. TiAl and NiAl in turbine blades or turbo chargers, respectively. A typical property of an intermetallic alloy is their, compared to pure metals, complicated crystallographic structure. Whereas Nickel and Copper are cubic face centered and Iron cubic face centered or cubic body centered depending on alloying elements, many intermetallic alloys have non-cubic structures. This has consequences for the solid state properties of the alloys as well as for their solidification. A very interesting alloy is the intermetallic phase $Zr_{50}Ni_{50}$. It is studied as a glass forming material, but it has as well a rare behavior in solidification. In ESL experiments with $Zr_{50}Ni_{50}$ we observed the growth of a solidification front with 10-fold symmetry (Fig. 1) at an undercooling temperature of 300 K and a cooling rate of 53 K/s. Microstructure analysis reflected the 10-fold symmetry and showed ten twins with strong correlation among each other. It seems that this structure was spanned by cooperative dendrite growth [1]. Interestingly, a similar 10-fold structure has been found by [2] in a rapidly quenched $Zr_{50}Ni_{50}$ alloy. The successful finding of this 10-fold structure in $Zr_{50}Ni_{50}$ raises the question about its further formation conditions.

The droptube experiment differs from a classical ESL experiment such that in tube the warmth is passed away so fast that it does not heat up significantly when it solidifies. In ESL the sample solidifies from the undercooled melt and its temperature rises up to liquidus temperature during recalescence. Possible cooling rates are of serveral hundred $\frac{K}{s}$. In the droptube experiment samples of sizes between 1 mm to 50 µm can be quenched with cooling rates between 1000 to 100 000 $\frac{K}{s}$, which can lead to different solidification behaviours and microstructures.

A ZrNi sample of 6mm diameter is prepared and placed in a Zirkonoxid crucible. The crucible has a pinhole of 0.2 to 0.4 mm diameter at its bottom and surrounded by an EML coil which heats the sample inside the crucible slowly to the molten state. Then Argon gas is injected into the coil to press the melt through the pinhole. The melt pours out into the roughly 10 m long droptube chamber, which is evacuated roughly to 10^{-4} mbar and refilled which Helium to 800 mbar. The molten drops solidify during their freefall through the chamber into spheres of different sizes which can be collected at the bottom.

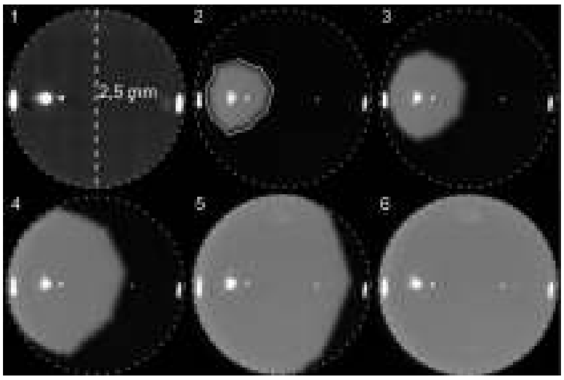

FIG. 1: A decagonal shaped solidification front propagates through a $Zr_{50}Ni_{50}$ sample at an undercooling of 300 K.

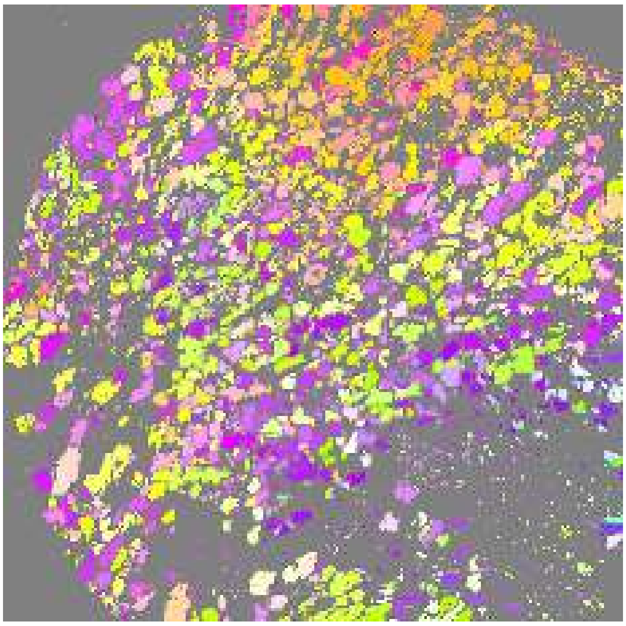

FIG. 2: The EBSD image shows a $Zr_{50}Ni_{50}$ sample of size between 100 and 63 µm. The different colors mark different orientations of the orthorombic ZrNi phase. The grey area inside the sample sphere is expected to be an unknown phase.

The granules are passed through a sieve to sort them by sizes between 1 mm to 50 µm. Spheres of different sizes are embedded and polished down to half spheres and can then be investigated with SEM and EBSD. Recently an unknown phase was found via EBSD at a sample of smallest size and is currently being investigated.

Special thanks go to Thomas Volkmann for his technical support.

* Corresponding author: `patrick.fopp@dlr.de`

[1] R. Kobold, *Thesis*, Bochum (2016).
[2] W.J. Jiang, Z.K. Hei, Y.X. Guo and K. H. Kuo, *Phil. Mag.* **A52**, p.L53 (1985).

Microstructure characterization of CoCrFeNiMnPd$_x$ eutectic high-entropy alloys

M. Kolbe,[1,*] Y. Tan,[2] J. Li,[2] J. Wang,[2] and H. Kou[2]

[1]Institut für Materialphysik im Weltraum, Deutsches Zentrum für Luft- und Raumfahrt (DLR), 51170 Köln, Germany
[2]State Key Laboratory of Solidification Processing, Northwestern Polytechnical University, Xi'an, Shaanxi 710072, PR China

Designing new alloys with improved properties for special applications is a central part of materials science. A new field are the so called high entropy alloys (HEA) [1], containing at least five elements with high concentration of 5-35 at.%. Usually such an alloy will contain a large amount of different phases, some of them being brittle and introducing low fracture toughness. Surprisingly, a considerable number of these alloys are single or double phase materials. The reason is a high mixing entropy in the liquid or in the high temperature solid state. The two phase alloys offer the opportunity to combine different properties, e. g. ductility and hardness, introduced by the two phases.

We studied the alloy system CoCrFeNiMnPd$_x$ (x=0.2-2), which aims at a eutectic HEA [2]. The idea is to combine the HEA CoCrFeNiMn (single FCC phase) by addition of Pd with an intermetallic phase (IM) and to produce a (FCC+IM)-type HEA. Pd was selected, because it exhibits the highest negative mixing enthalpy among the constituents with Mn and therefore Pd-Mn phases are expected as the preferred inter-metallic phases.

Microstructure analysis has been performed using a broad range of diagnostic tools as scanning electron microscopy (SEM), X-ray diffraction (XRD), transmission electron microscopy (TEM) and differential scanning calorimetry (DSC). Details can be found in [2], the main results are summarized in the following:

1. The alloys under investigation show a two-phase microstructure. The low Pd alloy (x=0.2) has a primary phase, which is similar to FCC CoCrFeNiMn solidifying in dendrites with a Pd-rich phase in the inter-dendritic space.
2. Alloys with higher Pd content (x<0.6) show coop-erative growth of two phases in eutectic dendrites or eutectic seaweed morphology and coarse eutectic (Fig. 1).

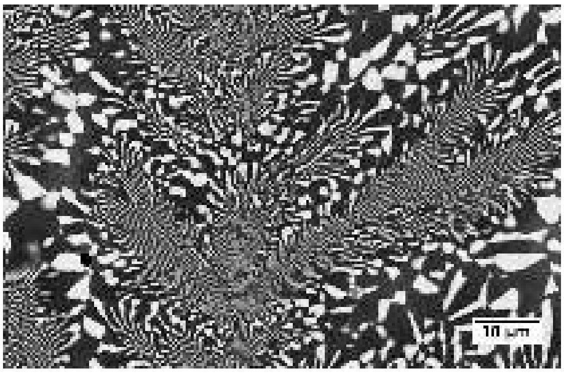

FIG. 1: Microstructure in the CoCrFeNiMnPd0.8 alloy. A eutectic dendrite is shown within coarse eutectic. The Pd-rich phase is given bright, the FCC phase dark.

3. The observation of cooperatively grown eutectic morphologies is supported by the DSC results, which show single, broad peaks upon cooling. This means solidification is a cooperative process of both phases.
4. XRD and TEM analyses show that the two phases exhibit a certain trend in their composition and crystal structure depending on Pd concentration. One phase is always FCC-structured, the other is an intermetallic Pd-Mn phase. With higher Pd content (x<0.6) more Pd enters the FCC phase up to equatomic concentration at highest Pd content. In parallel Mn leaves the FCC alloy and forms Pd-Mn phases with the remaining Pd. As the Pd-Mn system has a great number of intermetallic phases, several different Pd-Mn phases are observed.
5. The alloys with high Pd content (x<0.6) show not only a two-phase structure, but - in addition - a certain hierarchy of length scales in their microstructure. While the dendrites extend over several hundred microns, coarse granular eutectics is in the order of several microns. The fine lamellar eutectic has a size scale of below 1 micron, the Pd-Mn phases contain a great number of twins down to the nanometer scale. This type of microstructure has the potential of beneficial mechanical properties combining ductility and high mechanical strength.
6. Concerning design rules for high entropy alloys it has been shown that probably the high negative enthalpy mixing of Pd and Mn has an important influence towards the formation of a eutectic HEA instead of a single phase solid solution HEA.

Future work could be concentrated on the mechanical properties of the alloy system, on high temperature stability of the accompanying phases and metastable phases in non-equilibrium processing.

---

[*] Corresponding author: `matthias.kolbe@dlr.de`

[1] B. Cantor, I.T.H. Chang, P. Knight and A.J.B. Vincent, Mater. Sci. Eng. A **375-377**, 213-218 (2004).
[2] Y. Tan, J. Li, J. Wang, M. Kolbe and J. Kou, J. Alloys Compounds **731**, 600-611 (2018).

1.4 Granular Matter and Related

Influence of Mineral Composition on Sintering Lunar Regolith

A. Meurisse,[1,*] J. C. Beltzung,[1] M. Kolbe,[1] A. Cowley,[2] and M. Sperl[1,1]

[1] *Institut für Materialphysik im Weltraum, Deutsches Zentrum für Luft- und Raumfahrt (DLR), 51170 Köln, Germany*
[2] *ESA-EAC - European Space Agency - European Astronaut Centre - 51147 Köln, Germany.*

The Moon has been recently again under spotlight with the novel interests of a Moon village. A permanent lunar base will most likely call on existing architectural concepts of permanent habitats using lunar soil, underlining construction requirements and suggesting solutions to protect the explorers from vacuum, micrometeoroids and cosmic radiation [1–3]. In-situ resource utilization (ISRU) impacts significantly any outpost concept reducing launched Earth materials to a minimum thus making the mission cheaper and safer. One aspect of ISRU is using local resources as construction material to build shelters, roads or launchpads. The lack of actual lunar soil, called regolith, forces however the scientific community to use simulants made from Earth material. On the Moon, two different sites may be composed of regolith with two different mineral compositions and how these variations affect a sintering process need to be understood beforehand, on Earth. That is the reason why the authors investigate mechanical properties of sintered lunar regolith. Using JSC-1A and DNA lunar simulants, we studied the influence of changes in glass content, main plagioclase series and ilmenite content on a defined sintering process and on the mechanical properties of resulted sintered samples.

Plagioclase serie varies from two endmembers: anorthite and albite, respectively the main plagioclase compounds of JSC-1A and DNA lunar simulants. Under ambient conditions, albite and anorthite have a different melting point. This difference affects the sintering temperature: a diminution of 30°C was required to sinter the DNA lunar simulant with the same other parameters than JSC-1A (time, environment). This change in sintering temperature affected as well the other minerals of the simulants thus preventing the study of the influence of the glass content. The effect of the sintering environment was shown sintering JSC-1A lunar simulant in vacuum, shown Figure 1, and in air, shown Figure 2. In vacuum, the grains did not undergo any structural transformation and simply sinter together without interaction at the grain boundaries. In air, mainly iron oxide has the tendency to form at the boundaries thus preventing the grains to bond together. This issue was overcome increasing the sintering temperature which also led to the formation of a more porous sample due to the extra out-gassing provoked by the raise in temperature. This increase in porosity affected the mechanical properties reducing the compression strength from 152 MPa to 98 MPa. Finally addition of ilmenite material to mimic titanium rich areas on the Moon did not affect the sintering process. The same sintering parameters were used for sintering JSC-1A with ilmenite addition ranging from 0 wt.% to 20 wt.%.

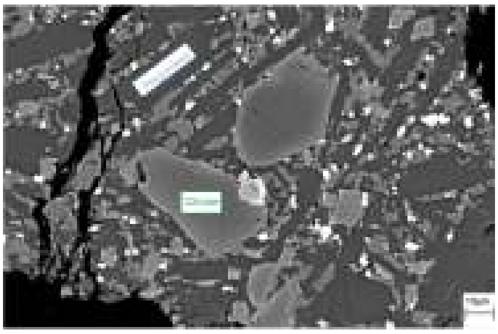

FIG. 1: SEM images of JSC-1A sintered under vacuum. No crystallographic transformations and no phase at the grain boundaries can be observed between sintered grains.

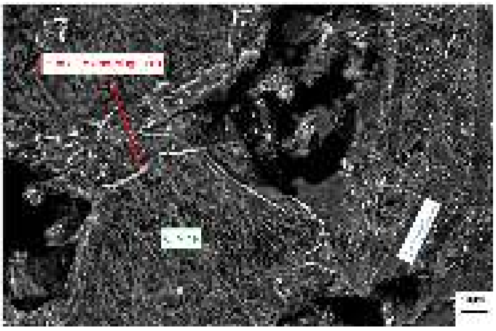

FIG. 2: SEM images of JSC-1A sintered in air. The formation of hematite (Fe_2O_3) and magnesia (MgO) can be observed at the border of an olivine grain with needle-shaped crystals.

In conclusion, ilmenite addition up to 20wt.% of the regolith showed a negligible effect on the sintered product. The anorthite plagioclase endmember cannot be replaced by albite, responsible for the low sintering temperature of DNA and covering up the effect of the glass phase. Vacuum environment was revealed to have a positive effect on JSC-1A sintering: the grains bond at lower temperature than in air, thus preventing the formation of additional porosity and increasing the compression strength up to 152 MPa compared to only 98 MPa for sintering JSC-1A in air.

This work has been carried out within the project entitled "3D printing of a model building block for a lunar base outershell" funded by ESA's General Support Technology Programm (GSTP). The authors wish to thank Advenit Makaya and Laurent Pambaguian, from ESA-ESTEC, for the interesting discussions and constructive comments during the project.

[*] Corresponding author: `alexandre.meurisse@dlr.de`

[1] T. Rousek, K. Eriksson, and O. Doule, Acta Astronautica **74**, 98-111 (2012).

[2] G. Cesaretti, E. Dini, X. De Kestelier, V. Colla, and L. Pambaguian, Acta Astronautica **93**, 430-450 (2014).

[3] H. Benaroya, and L. Bernold, Acta Astronautica **62**, 277-299 (2008).

Statistical nature of granular tribocharging

J. Haeberle,[1,*] M. Sperl,[1] P. Born,[1] A. Schella,[2] and M. Schröter[2]

[1] *Institut für Materialphysik im Weltraum, Deutsches Zentrum für Luft- und Raumfahrt (DLR), 51170 Köln, Germany*
[2] *Dynamik komplexer Fluide, Max-Planck-Institut für Dynamik und Selbstorganisation MPI-DS, 37077 Göttingen, Germany*

Forming and breaking of contacts among solid bodies is intrinsically connected to the generation of electrostatic charge. As such, this contact- or triboelectric charging is omnipresent in handling or fluidizing granular particles. The strength of the Coulomb interaction among the particles generated by triboelectric charging can frequently exceed any other interactions among the particles and even gravity. As such, it can be a non-negligible contribution to the dynamics and the arrangement of granular particles.

A common feature among the mechanisms which are proposed to cause electrostatic charging is their statistical nature [1]. The separation of the charged surfaces also must inevitably be connected to an at least transient discharging process [1]. The build up of the charge and the discharging are presently rarely discussed together, still the final charge on both surfaces is the result of both mechanisms.

Combining the statistics of both processes allows to derive a prediction for the distribution of the final charge Q_f produced by many independent contacts with the same configuration:

$$Q_f = \mathcal{N}(\mu_{tc}, \sigma_{tc}) * e^{-\mathcal{N}(\mu_{dc}, \sigma_{dc})}, \qquad (1)$$

with μ_{dc} the mean attenuation due to discharge and σ_{dc} its standard deviation. Without recombination, triboelectric charging can be expected to result in normal distributed charges Q_f with final charges of both signs possible. Contacts with a vanishing σ_{tc}, i.e. a deterministic transferred charge μ_{tc} combined with a random discharging, result in log-normal distributed final charges. In this case, the final charges all have the same sign. The intermediate cases, combining stochastic charging and discharging, result in distributions that are not symmetric about the mean and exhibit exponentially decaying probabilities for the final charges and thus deviate from normal and log-normal distributions.

We designed a setup to measure the distribution of charges over many identical granular particle contacts (see Fig. 1, [1]). Particles bounce off a grounded collision target after being discharged, and the remaining charge after this single collision is measured. The resulting charge distributions (see Fig. 2) exhibit many of the aforementioned features of the intermediate case, indicating granular triboelectric charging being a combination of charging and discharging. Correct modeling and engineering of granular triboelectric charging thus has to take both processes into account. Due to the exponential decay of the probability distributions, extreme charges far form the mean also have a higher probability than for the case of normal distributions.

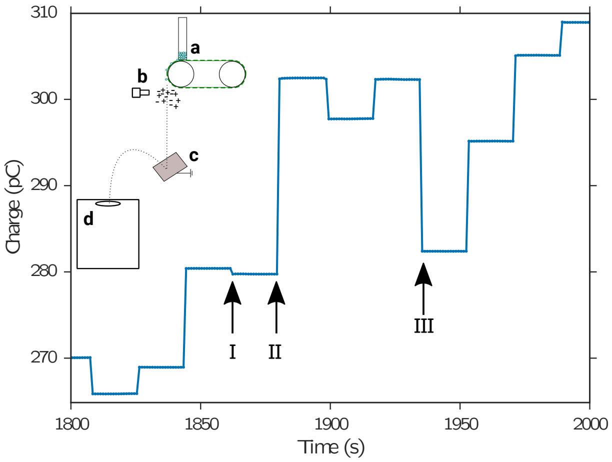

FIG. 1: Detail of the charge measurements, here glass beads bouncing off a PTFE slab. Particle drops causes a change in charge accumulated in the Faraday cup, causing regular jumps of the curve. Steps I, II, and III exemplify the large variability in magnitude and sign of the charge on the particles. Inset shows the measurement setup: a) particle reservoir and particle dispenser, b) ionization needle and ionized air to discharge the particles, c) collision target, d) Faraday cup. The dotted line indicates the route of the particles.

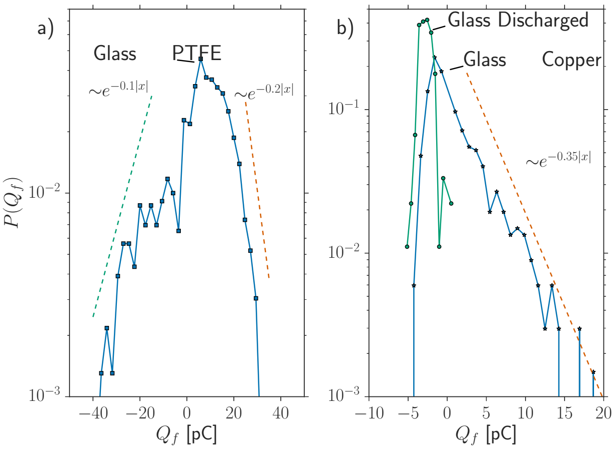

FIG. 2: Probability distribution for charges accumulated in single collisions of glass beads with a PTFE slab (a) and in collisions of glass beads with a Copper slab (b). The dashed lines act as a guide to the eye and highlight the exponential decay of the tails. Also shown in the (b) is the distribution of charges on the particles after being discharged by passing the ionization needle without colliding with a target.

[*] Corresponding author: `jan.haeberle@dlr.de`

[1] J. Haeberle, A. Schella, M. Sperl, M. Schröter, and P. Born, in preparation.

Approaching jamming in microgravity and on ground

P. Born,* J. Schmitz, and M. Sperl
Institut für Materialphysik im Weltraum, Deutsches Zentrum für Luft- und Raumfahrt (DLR), 51170 Köln, Germany

A challenge in experimental studies on bulk fluidized granular media is fluidization at high packing fractions. Fluidization by vibration is known to produce inhomogeneous fluidized states of granular media, where the media separate into dense and dilute phases. Fluidization by pressing a liquid or a gas through a granular column is able to produce more homogeneous states, but the density of the granular medium and the agitation strength are coupled. In particular, fluidzation with particle motion only sets in if the packing fraction gets below a threshold. This threshold is defined by particle interactions and the confining pressure build up by earth gravitation. Experimental studies on steady states close to the jamming packing fraction of granular media are thus not feasible with these methods on ground.

We realized a setup with gas fluidization for experiments in microgravity (see Fig. 1, [1]). The confining pressure vanishes in microgravity and the direction of fluidization can be arbitrary. The microgravity is realized in catapult flights in the ZARM drop tower in Bremen. We apply a light scattering methodology that is able to characterize the homogeneity and the kinetic energy in the granular medium [2]. The setup allows to change the volume of the sample cell and as such the filling fraction of the granular medium in the cell.

The filling fraction of the sample cell and the packing fraction of the granular medium decouple on ground, as expected. The particles stay sedimented in a dense state with a free surface, where the packing fraction is given by the agitation strength. In contrast, the granular medium expands in microgravity and fills the whole sample cell. The results of the light scattering diagnostics indicate a fundamentally different approach to jamming in microgravity and on ground once the volume of the sample cell is lowered (see Fig. 2, [3]).

On ground, the granular medium and its dynamics basically stay unaffected as long as the filling fraction is lower than the packing fraction of the fluidized medium. Once the volume of the cell is lowered and the filling fraction becomes higher than the packing fraction, the sample starts to partially arrest at a high packing fraction, while in the remaining volume the lower fluidized packing fraction is kept. The arrested fraction of the sample grows until the whole sample is arrested with lowering the volume of the sample cell.

In microgravity, the packing fraction is defined by the filling fraction at all sample cell volumes. With lowering the sample cell volume the packing fraction increases, until at the packing fraction of arrest the whole sample arrests at once. The transition to arrest of granular media in microgravity thus is much more defined than on ground, supporting the assumption of jamming being a well defined point in the phase space of agitated granular media.

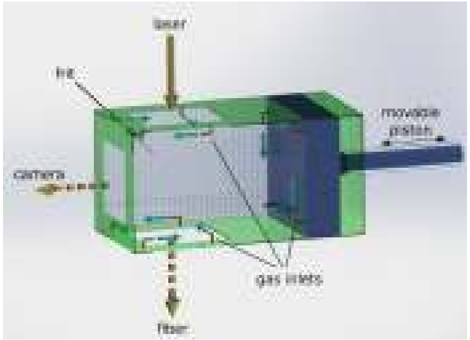

FIG. 1: The sample cell for fluidizing granular media on ground and in microgravity. Indicated are the piston to change the volume of the cell, the windows for light scattering diagnostics, the gas inlets for tangential agitation of the granular medium and glass frits as gas outlets.

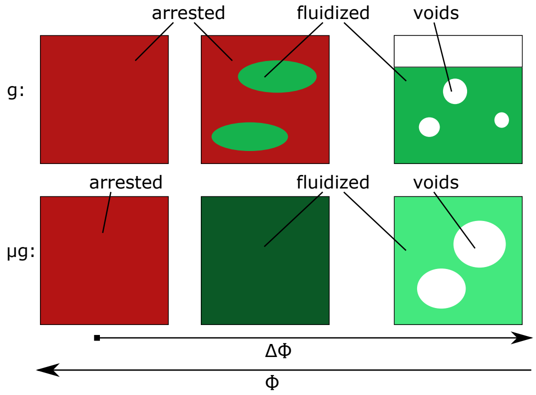

FIG. 2: Scheme how a granular medium approaches full arrest at high packing fraction Φ on ground (g) and in microgravity (μg). See text for detailed discussion. The colors indicate packing fractions and dynamics. White areas indicate empty voids and density fluctuations and a free surface of the granular medium on ground.

We thank the team from the ZARM Drop Tower Operation and Service Company (ZARM FAB mbH) for valuable technical support during the finalization of the setup and the measurement campaign. The European Space Agency is acknowledged for providing access to the drop tower by ESA-AO-2009-0943 "Compaction and Sound Transmission in Granular Media".

* Corresponding author: `philip.born@dlr.de`

[1] P. Born, J. Schmitz, M. Bußmann, and M. Sperl, Microgravity Sci. Technol. **28**, 413 (2016).
[2] P. Born, S. Reinhold, and M. Sperl, Phys. Rev. E **94**, 032901 (2016).
[3] P. Born, J. Schmitz, and M. Sperl, npj Microgravity **3**, 27 (2017).

THz transmission of dense granular media

P. Born[1,*] and K. Holldack[2]

[1] *Institut für Materialphysik im Weltraum, Deutsches Zentrum für Luft- und Raumfahrt (DLR), 51170 Köln, Germany*
[2] *Institut für Methoden und Instrumentierung der Forschung mit Synchrotronstrahlung, Helmholtz-Zentrum Berlin für Materialien und Energie GmbH, Albert-Einstein-Str. 15, 12489 Berlin, Germany*

Mechanical properties of granular media depend to a large extent on the geometrical arrangement of the particles in the granular medium. The problem of characterizing the packing structure of a bulk granular medium is not satisfactorily solved, though granular particles are macroscopic objects. Granular media are opaque even if they consist of particles that do not absorb light, and the only approaches to structural characterization are either tomographic methods based on X-rays or scanning techniques with index-matched suspensions. Both methods have limitations for dynamic granular media, as scanning times are frequently too long and particles cannot be resolved anymore.

We suggest an approach to structure sensitivity with a higher versatility based on spectroscopy. Light propagates through bulk opaque media by multiple scattering. The direction of the light is thus randomized after transmission and does not carry much information on the sample anymore. However, the efficiency of the light transport depends on the local scattering efficiencies in the sample. These scattering efficiencies depend strongly on two aspects, the local geometric arrangement and the ratio of the wavelength of the light to the size of the scattering features. Spectral measurements consequently probe local geometries at different length scales, and short scanning times can be achieved.

THz radiation has a suitable wavelength to probe geometric features of granular particles in many practical situations [1]. THz radiation thus is a good candidate to also probe structural features in granular media. We realized a setup for rotating or vibrating granular media inside of a THz spectrometer available at the THz beamline of Bessy II, Berlin [2].

A sensitivity of the measured THz transmission spectra can be shown (see Fig. 1). With increasing packing fraction of the sample an increase in overall transmission can be observed, in line with an increase of the effective refractive index. Additionally, at a particular wavelength λ of approximately 2 particle diameter the transmission gets increasingly suppressed with increasing the packing fraction of the hard particles. This behavior indicates a resonance in backscattering, where backscattered light interferes constructively at each two particles.

The high time resolution of spectroscopic measurements allows to monitor structural changes in dynamic samples. A consolidated vibrated granular medium exhibits already the backscattering resonance (see Fig. 2). The sudden transition with continued vibration to regular structure can be identified in the spectra.

THz spectroscopy thus may be applied to track the structure during segregation, crystallization or fluidization processes. It may be interesting to investigate the nature of the backscattering resonance in detail. Particularly, the relation between this resonance and the formation of photonic bandgaps may guide a more general approach to the optics of hard sphere packings.

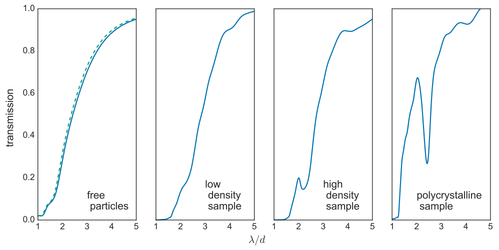

FIG. 1: Demonstration of the structure sensitivity of THz transmission spectroscopy. Transmission is measured for individual particles, a low-density packing formed by sticky particles, a dense disordered packing formed by hard-spheres, and a polycrystalline packing of these spheres. Transmission becomes increasingly suppressed at $\lambda \approx 2d$ with increasing packing density. The position of this feature shifts away from $\lambda = 2d$ due to the increase of the effective refractive index of the particle packing with packing density. The dashed line in the left panel is the transmission of free particles expected from Mie-theory with a fitted number density.

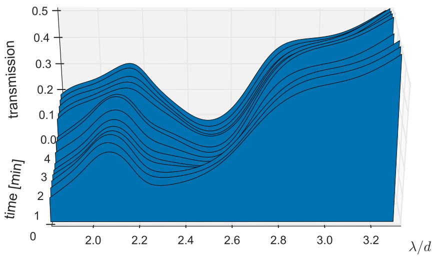

FIG. 2: Evolution of the transmission spectrum of a vibrated packing of monosized spheres with time. The initial position of the scattering feature ($\lambda \approx 2.25d$) indicates a dense packing, which evolves into a polycrystalline packing with a strong scattering feature at $\lambda \approx 2.6d$ within a few minutes.

The authors thanks Matthias Sperl and Andreas Meyer for their continued support of the project, Jan Haeberle and Sebastian Pitikaris for help during measurement campaigns, and A. Schnegg and D. Ponwitz for support at the THz-beamline at Bessy II.

[*] Corresponding author: `philip.born@dlr.de`

[1] P. Born, K. Holldack, and M. Sperl, Granular Matter 17, 531 (2015).
[2] P. Born, and K. Holldack, Rev. Sci. Instrum. **88**, 051802 (2017).

Rheology of Granular Fluids

W. T. Kranz,[1,*] O. Lopez,[1] M. Sperl,[1,2] F. Frahsa,[3] M. Fuchs,[3] and A. Zippelius[4]

[1] *Institut für Materialphysik im Weltraum, Deutsches Zentrum für Luft- und Raumfahrt (DLR), 51170 Köln, Germany*
[2] *Institut für Theoretische Physik, Universität zu Köln, 50937 Köln, Germany*
[3] *Fachbereich Physik, Universität Konstanz, 78457 Konstanz, Germany*
[4] *Institut für Theoretische Physik, Georg-August-Universität Göttingen, 37077 Göttingen, Germany*

Understanding and predicting granular flow is desirable for many industrial processes as a large fraction of raw materials comes in granular form [1] and handling granular matter under reduced gravity will become important in the near future for 3d-printing of regolith [2]. On earth, a fluidized bed can be used to study granular fluids at packing fractions lower than the closed packed isostatic configurations.

We used an innovative Anton Paar air-fluidized shear cell (Powder Cell PCC V1 with Fluidization Set Quality Control FSQ and Fluidization Set Scientific FSS 15) for an Anton Paar rheometer MCR 102 to measure flow curves, *i.e.*, shear stress σ as a function of shear rate $\dot\gamma$ at well controlled packing fractions (Fig. 1). Considerable care has been taken to prepare the samples and to ensure reproducible conditions. Moreover it was found that extended periods of shearing were necessary to ensure stationary conditions. To understand the results, we developed a kinetic theory [3, 4] applicable at high densities and high shear rates of non-equilibrium granular fluids based on the Integration Through Transients (ITT) formalism [5]. In terms of the Peclet number $\mathrm{Pe} \propto \dot\gamma$, we find

$$\frac{\sigma}{nT} = \frac{\sigma_0}{nT} + \mathrm{Pe}\,\varphi \frac{(1+\varepsilon)^2}{4} \int_0^\infty \frac{\mathrm{d}\tau}{\sqrt{1+(\mathrm{Pe}\,\tau)^2/3}} \times \int_0^\infty \frac{\mathrm{d}q^* q^{*4}}{360\pi} \times \frac{C_{q^*(-\tau)} C_{q^*}}{S_{q^*}^2} \Phi^2_{q^*(-\tau)}(\tau), \quad (1)$$

where $\Phi_q(t)$ denotes the dynamics scattering function and S_q, C_q are structural correlations. This granular ITT theory allows to predict flow curves over many orders of magnitude (Figs. 1,2) for different packing fractions and different inelasticities of the particles, quantified by a coefficient of restitution ε.

Consistently between experiment and theory, we observe a rich phenomenology. For low shear rates and low densities the granular system behaves as a Newtonian fluid, $\sigma \sim \dot\gamma$. The theory predicts that this regime ends when the shear rate becomes comparable to the α-relaxation rate of the granular fluid. In particular, above the granular glass transition [6], the fluidized bed acquires a finite yield stress, $\sigma(\dot\gamma \to 0) > 0$ and generally shows shear thinning, $\sigma \approx$ const., beyond the Newtonian regime. At the highest shear rates, shear heating becomes dominant and the fluidised bed follows Bagnold scaling [7], $\sigma \sim \dot\gamma^2$, which manifests itself as shear thickening. Exploring how accurate the quantitative predictions of granular ITT track the experimental results as well as applying the knowledge gained here to build a 3d-printer that functions in micro-gravity is work in progress.

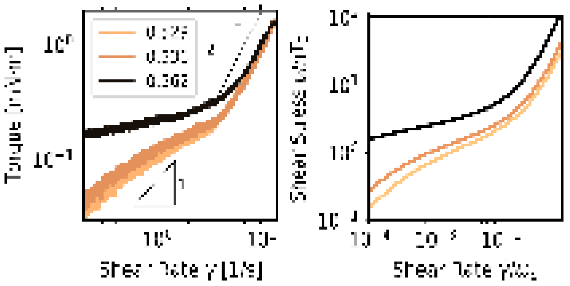

FIG. 1: (Left) Experimental flow curves determined by the Anton Paar (MCR 102) fluidised bed shear cell for three packing fractions as indicated. Particles are PS spheres of diameter 250 μm. (Right) Granular ITT prediction for comparable packing fractions. Note the excellent agreement between measurements and predictions.

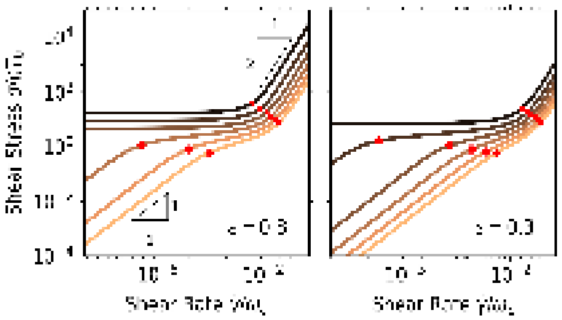

FIG. 2: Flow curves determined by granular ITT, shear stress σ as a function of shear rate $\dot\gamma$ for different packing fractions from $\varphi = 0.48$ (bottom) to 0.58 (top) and two values of the coefficient of restitution ε as indicated. The slope of the Newtonian and Bagnold regime is indicated. Red crosses mark where the α-relaxation rate is comparable to the shear rate and the red squares mark where shear heating becomes important.

We acknowledge illuminating discussions with Hisao Hayakawa and Thomas Voigtmann

[*] Corresponding author: `till.kranz@dlr.de`

[1] P. Richard, M. Nicodemi, R. Delannay, P. Ribiere, and D. Bideau, Nature Materials **4**, 121 (2005).
[2] A. Meurisse, J. C. Beltzung, M. Kolbe, A. Cowley, and M. Sperl, J. Aerospace Engng., **30**, 04017014 (2017)
[3] W. T. Kranz, F. Frahsa, A. Zippelius, M. Fuchs, M. Sperl, submitted to Phys. Rev. Lett., arXiv:1710.04452
[4] W. T. Kranz, F. Frahsa, A. Zippelius, M. Fuchs, M. Sperl, submitted to Phys. Rev. Fluids, arXiv:1710.04475
[5] M. Fuchs, M. E. Cates, Phys. Rev. Lett. **89**, 248304 (2002)
[6] W. T. Kranz, M. Sperl and A. Zippelius, Phys. Rev. Lett. **104**, 225701 (2010)
[7] R. A. Bagnold, Proc. Royal Soc. A **225**, 49 (1954)

Rheology of Hertzian Spheres

W. T. Kranz[1,*] and M. Sperl[1,2]

[1] Institut für Materialphysik im Weltraum, Deutsches Zentrum für Luft- und Raumfahrt (DLR), 51170 Köln, Germany
[2] Institut für Theoretische Physik, Universität zu Köln, 50937 Köln, Germany

Flows of dense granular materials are ubiquitous in nature and industry [1, 2]. Inclined plane flows both in industrial and geophysical settings have been successfully modeled by inelastic Hertzian spheres [2, 3] using molecular-dynamics simulations. Discrete element models are constrained, however, to relatively small system sizes due to computational demands. For a continuum modeling which can be applied at very large scales, it is essential to have access to the transport coefficients as functions of the system parameters. Based on a recent generalization [4, 5] of the Integration Through Transients (ITT) formalism [6] we calculated the viscosity and the Bagnold coefficient for inelastic Hertzian spheres [7].

We consider a monodisperse system of inelastic Hertzian spheres [8] of diameter d and mass $m = 1$ at finite packing fraction φ. The overlap potential is given by

$$V(r) = \Gamma T(1 - r/d)^{5/2} \quad \text{for } r < d \qquad (1)$$

where Γ controls the the strength of repulsion and T denotes the granular temperature. We focus on the practically relevant case of stiff particles $\Gamma \gg 1$. Dissipation is quantified by a constant coefficient of restitution $\varepsilon < 1$. Fluidisation is modelled by a random force with a strength characterised by the fluidisation power. We prescribe a shear rate $\dot\gamma$ through the Sllod equations of motion [9].

For moderate densities and small shear rates (Fig. 1), we observe that the viscosity η increases with ε as expected. Note that we obtain values that are far above the Boltzmann-Enskog value η_0. Also the stiffer particles have a higher viscosity. In general, the viscosity increases over several orders of magnitude upon increasing the density. Note that we span more than two orders of magnitude in viscosity by varying the inelasticity ε at the highest packing fraction considered.

For strong shear such that shear heating dominates the fluidisation $\eta\dot\gamma^2 \gg P_D$ we obtain Bagnold scaling where the system no longer behaves like a Newtonian fluid with a stress $\sigma = \eta\dot\gamma$, but $\sigma = B\dot\gamma^2$ with the Bagnold coefficient B. We observe (Fig. 2) a very weak dependence of B on the stiffness Γ but, just as for the viscosity, a strong increase with the coefficient of restitution ε. As is expected also the Bagnold coefficient increases with increasing density.

We acknowledge continuing discussions with Annette Zippelius, Matthias Fuchs, and Fabian Frahsa and thank Marco Heinen for the structure factor code

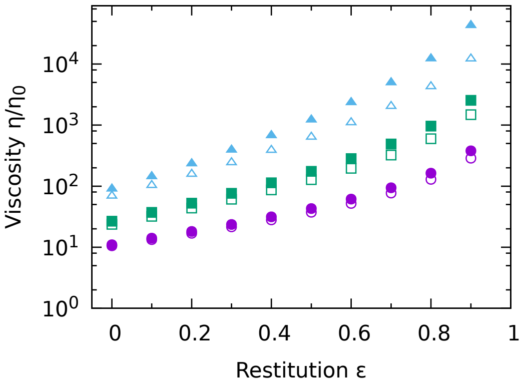

FIG. 1: Viscosity η relative to its low density limit η_0 as function of the coefficient of restitution ε for packing fractions $\varphi = 0.51$ (volet disks), 0.56 (green squares), and 0.61 (blue triangles) and stiffness $\Gamma = 1000$ (open), and 1500 (filled)

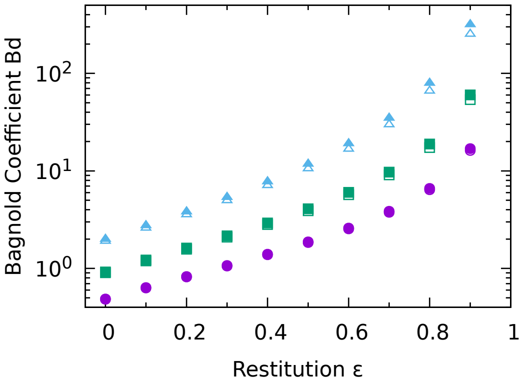

FIG. 2: Bagnold coefficient $B \cdot d$ as function of the coefficient of restitution ε for packing fractions $\varphi = 0.51$ (volet disks), 0.56 (green squares), and 0.61 (blue triangles) and stiffness $\Gamma = 1000$ (open), and 1500 (filled)

[1] K. Hutter and N. Kirchner, *Dynamic response of granular and porous materials under large and catastrophic deformations* (Springer, Heidelberg, 2013)
[2] H. M. Jaeger, S. R. Nagel, Science **255**, 1523 (1992)
[3] C. S. Campbell, Powder Technology **162**, 208 (2006)
[4] W. T. Kranz, F. Frahsa, A. Zippelius, M. Fuchs, M. Sperl, submitted to Phys. Rev. Lett., arXiv:1710.04452
[5] W. T. Kranz, F. Frahsa, A. Zippelius, M. Fuchs, M. Sperl, submitted to Phys. Rev. Fluids, arXiv:1710.04475
[6] M. Fuchs, M. E. Cates, Phys. Rev. Lett. **89**, 248304 (2002)
[7] W. T. Kranz and M. Sperl, EPJ Web Conf. **140**, 03064 (2017)
[8] J. C. Pamies, A. Cacciuto, D. Frenkel, J. Chem. Phys. **131**, 044514 (2009)
[9] G. P. Morriss, D. J. Evans, *Statistical Mechanics of Nonequilbrium Liquids* (ANU Press, Canberra, 2007)

[*] Corresponding author: `till.kranz@dlr.de`

1.5 Complex Plasmas

Instabilities in bilayer complex plasmas: Wake-induced mode coupling

A. V. Ivlev[1,*] and R. Kompaneets[2]

[1] *Max-Planck-Institut für extraterrestrische Physik, 85748 Garching, Germany*

[2] *Institut für Materialphysik im Weltraum, Deutsches Zentrum für Luft- und Raumfahrt (DLR), 82234 Wesseling, Germany*

Complex plasmas are plasmas containing dust particles, which get electrically charged by collecting free ions and electrons, and, owing to the resulting strong interparticle interactions, are often used as model systems to study various phenomena occurring in fluids and solids [1]. Experiments with complex plasmas are performed on the ground as well as, to get rid of the gravity force strongly affecting dust structures, on parabolic flights and onboard the International Space Station.

In ground-based experiments with complex plasmas, the dust particles generally form a horizontal monolayer, either fluid or crystalline, or another structure strongly squeezed vertically due to the gravity force, and such experiments are characterised by non-reciprocal interactions between dust particles, i.e., actio $\neq$ reactio. Of course, the third Newton law by itself is not violated — the non-reciprocity is due to the plasma, which acts as a mediator of the interactions and is thus a third body. This non-reciprocity is unavoidable in ground-based experiments: The particles are levitated against the gravity force by a strong electric field, which drives ion flow in the parent neutral gas and thereby distorts the otherwise spherically symmetric Debye shielding clouds surrounding the charged dust particles. This makes ground-based complex plasmas hardly suitable to model processes occuring in conventional fluids and solids, but, on the other hand, opens up an excellent possibility to study non-Hamiltonian systems.

And perhaps one of the most well-known and thoroughly studied phenomena resulting from the non-Hamiltonian nature of the dust dynamics is the mode coupling instability of crystalline dust monolayers [2]. The physics of this phenomenon is simple: Owing to the non-reciprocal interparticle interactions, the horizontal motion of dust particles in the monolayer is coupled to the vertical motion even in the linear perturbation approximation, and the coupling coefficient is of the sign that triggers an oscillatory instability. Importantly, this phenomenon has two thresholds: First, the monolayer must be dense enough for the modes to intersect, and, second, the gas pressure must be small enough for the instability not to be suppressed by the dust-neutral friction. The phenomenon was extensively studied theoretically and experimentally and also was reproduced in simulations.

The work reported on this page of the annual report is a thorough theoretical study of a similar phenomenon in bilayers, which, like monolayers, can easily be formed in ground-based experiments. The corresponding publication is Ref. [3].

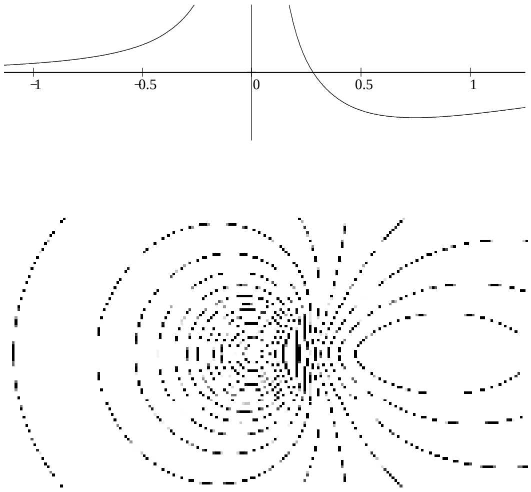

FIG. 1: A typical result of the calculation of the interparticle interaction potential. The upper graph shows the potential (divided by the negative charge of the particle) as a function of the distance for the direction along the flow. The lower plot shows equipotential lines, with the particle being in the centre. The flow is to the right. For the parameter values and spatial dimensions of the graphs, see Ref. [3].

The study is based on the recent theory of the interaction between dust particles first-authored by the DLR participant of the study [4]. Unlike many models assuming a shifted Maxwellian distribution of ions, the theory self-consistently takes into account the electric field that drives the ion flow, ion-neutral collisions, and the resulting non-Maxwellian ion velocity distribution. The resulting interaction potential is shown in Fig. 1 for some typical parameter values and generally does not have an oscillatory structure predicted by models based on the assumption of a shifted Maxwellian distribution.

The study predicts a new kind of mode coupling instability — an instability triggered by the coupling between horizontal modes of different layers. The instability is due to the non-Hamiltonian nature of the dust dynamics, can be realised experimentally under easily achievable conditions, and works both for crystalline and fluid bilayers, and its temporal development beyond the linear stage well may lead to interesting nonlinear phenomena in such a non-Hamiltonian system.

[*] Corresponding author: `ivlev@mpe.mpg.de`

[1] G. E. Morfill and A. V. Ivlev, Rev. Mod. Phys. **81**, 1353 (2009).

[2] A. V. Ivlev, U. Konopka, G. Morfill, and G. Joyce, Phys. Rev. E **68**, 026405 (2003); L. Couëdel, V. Nosenko, A. V. Ivlev, S. K. Zhdanov, H. M. Thomas, and G. E. Morfill, Phys. Rev. Lett. **104**, 195001. (2010).

[3] A. V. Ivlev and R. Kompaneets, Phys. Rev. E **95**, 053202 (2017).

[4] R. Kompaneets, G. E. Morfill, and A. V. Ivlev, Phys. Rev. Lett. **116**, 125001 (2016); R. Kompaneets, G. E. Morfill, and A. V. Ivlev, Phys. Rev. E **93**, 063201 (2016).

Coupling of Noncrossing Wave Modes in a Two-Dimensional Plasma Crystal

J. K. Meyer,* I. Laut, S. Zhdanov, V. Nosenko, and H. M. Thomas

Institut für Materialphysik im Weltraum, Deutsches Zentrum für Luft- und Raumfahrt (DLR), 82234 Wesseling, Germany

A complex, or dusty, plasma is a weakly ionized gas in which micrometer sized particles are immersed . In many experiments the particles become suspended in a two-dimensional (2D) layer in the sheath of the lower electrode, where the downward gravitational force is balanced by the upward electric force. The ability to directly image the particle motion via laser illumination and high speed videography allows the complete measurement of the state of the entire particle ensemble. Combining these factors, complex plasmas are convenient systems for experimental study of strongly coupled phenomena at the kinetic level.

In a 2D complex plasma crystal, two in-plane dust-lattice (DL) wave modes are permitted, namely the longitudinal (L) and transverse horizontal (TH) modes with acoustic dispersion. Due to finite vertical confinement, a transverse vertical (TV) mode is also permitted . This vertical mode has negative optical dispersion and depends on the *plasma wake* below the particles. The plasma wake can be modeled as a point charge below the particle. It interacts with neighboring particles and is tied positionally relative to its seed particle.

When studying generic phenomena like transport phenomena, phase transitions, and linear and nonlinear waves in complex plasmas, care has to be taken that the plasma-specific processes do not play a role. One prime example of such a specific process is the so-called mode-coupling instability (MCI), where the L and TV modes intersect and at the intersection the unstable hybrid mode is formed which grows exponentially with time until the crystal melts [1]. During the MCI, a *mixed polarization* can be observed in experiments, where traces of the L mode can be measured in the transverse vertical spectra and vice versa.

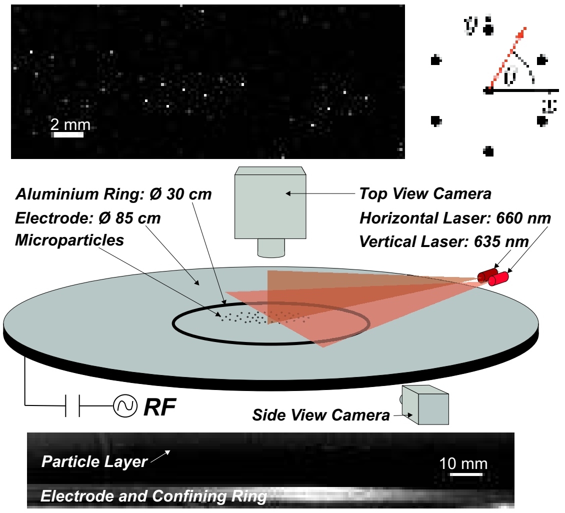

FIG. 1: Layout of the setup used in the experiment with a cropped top view image (top left) from the experiment showing part of a crystal and a side view (bottom). The electrode is 85 cm in diameter, and there is an aluminium ring with inner diameter 30 cm for radial confinement. The microparticles are illuminated horizontally by a 660 nm wavelength laser sheet and vertically (through the center of the cloud) by a 635 nm wavelength laser sheet.

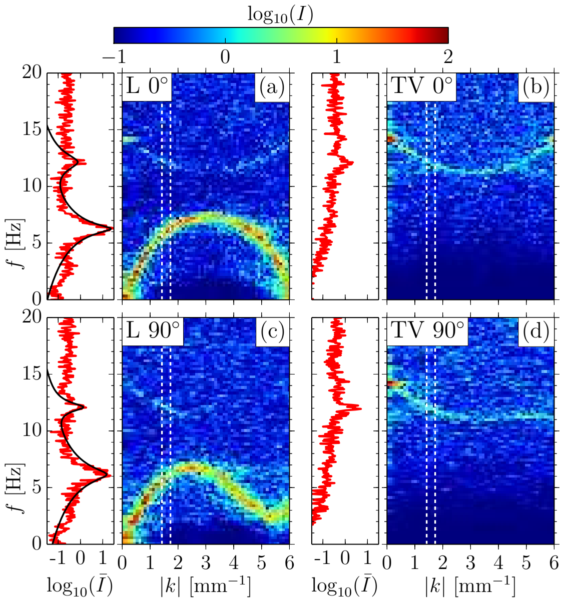

FIG. 2: Experimental fluctuation spectra for longitudinal (L) and transverse vertical (TV) waves with wave vectors along $\theta = 0^\circ$ and $\theta = 90^\circ$. To the left of each panel, the average intensity $\bar{I}$ in the range $1.4\ \mathrm{mm}^{-1} < |k| < 1.8\ \mathrm{mm}^{-1}$ is shown. Intensities are shown in arbitrary units and with logarithmic scale.

In our contribution [2], we report on the observation of mixed polarization of L and TV modes in a 2D complex plasma crystal in the absence of mode crossing. A new chamber was used for these experiments which had a much larger radius (85 cm) and crystal size (27 cm), see Fig. 1. It is an RF plasma in argon at background pressures of 1.00-0.10 Pa. This larger crystal size and lower pressure allowed for more uniform crystals and less damping of particle motion. Our experimental L mode spectra showed the mixed polarization of the L and TV modes in the absence of mode crossing, see Fig. 2. Molecular-Dynamics simulated experiments with point-like wakes and similar theory backed up our observations and support the conclusion that the effect is wake mediated.

---

* Corresponding author: `john.meyer@dlr.de`

[1] L. Couëdel, V. Nosenko, A. V. Ivlev, S. K. Zhdanov, H. M. Thomas, and G. E. Morfill, Phys. Rev. Lett. **104**, 195001 (2010).

[2] Meyer, J. K. and Laut, I. and Zhdanov, S. K. and Nosenko, V. and Thomas, H. M., Phys. Rev. Lett. **119**, 255001 (2017).

Spinning particle pairs in a single-layer complex plasma crystal

V. Nosenko,[1,2,*] S. K. Zhdanov,[1] H. M. Thomas,[1] J. Carmona-Reyes,[2] and T. W. Hyde[2]

[1] *Institut für Materialphysik im Weltraum, Deutsches Zentrum für Luft- und Raumfahrt (DLR), 82234 Wesseling, Germany*
[2] *Center for Astrophysics, Space Physics, and Engineering Research, Baylor University, Waco, Texas 76798-7310, USA*

Complex plasmas are popular model systems to study various phenomena such as waves, phase transitions, and transport phenomena, in real time and at the level of individual particles. However, care should be taken to clearly separate the generic and plasma-related phenomena which are peculiar to plasma crystals. The latter may be, e.g., mode-coupling instability (MCI), channeling of upstream extra particles, or particle pairing. Vertical pairs of particles can form in a single-layer plasma crystal spontaneously or after a sudden drop of the neutral gas pressure. Pairs of particles which were spinning around their axis were recently observed in Ref. [1]. Such spinning pairs, or torsions can form in a single-layer complex plasma crystal if the vertical confinement becomes sufficiently weak. A theoretical model of a spinning particle pair based on the plasma wake (ion focus) effect was proposed in Ref. [1]. According to this model, torsions are driven by the nonreciprocal interactions between dust particles mediated by the plasma wakes.

In the present contribution, we systematically study torsion formation using lower than in Ref. [1] gas pressures, in order to better reveal the particle dynamics. The experiments were performed in a modified Gaseous Electronics Conference (GEC) rf reference cell [2]. Plasma was produced by a capacitively coupled radio-frequency (rf) discharge in argon. Melamine-formaldehyde microspheres with a diameter of 8.9 ± 0.09 μm were suspended as a single layer in the plasma sheath above the lower rf elecrode. The argon pressure p_{Ar} was then set to either 19.3, 17.4, or 12 Pa and the forward discharge power P_{rf} was stepwise reduced from 40 to 1 W. This resulted in a weakening of the vertical confinement for the particles and eventual departure of their suspension from the single-layer structure.

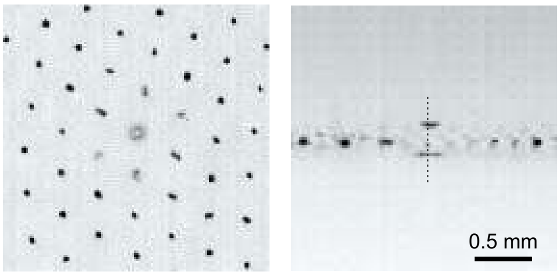

FIG. 1: Spinning pair of particles in a single-layer plasma crystal. Left panel shows the top view, right panel the side view. The particles spin around the vertical axis shown by the dashed line. 90 frames from the video are superimposed, the resulting image is inverted and its brightness and contrast adjusted. Experimental parameters were the following: argon pressure $p_{\mathrm{Ar}} = 17.4$ Pa, discharge power $P_{\mathrm{rf}} = 7$ W.

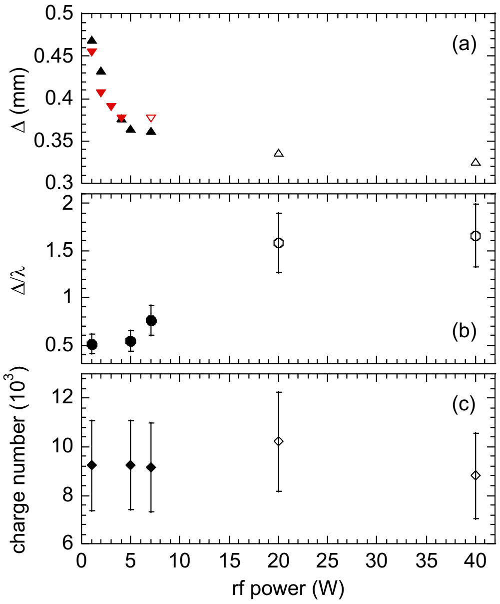

FIG. 2: Mean interparticle spacing Δ (a), screening parameter $\kappa = \Delta/\lambda$ (b), and particle charge number Z (c) as functions of the discharge power P_{rf}. Open symbols indicate undisturbed crystal, solid symbols indicate crystal with torsions. The pressure of argon was $p_{\mathrm{Ar}} = 17.4$ Pa, except for down triangles in (a), which correspond to $p_{\mathrm{Ar}} = 19.3$ Pa.

In the experimental runs with argon pressures of $p_{\mathrm{Ar}} = 19.3$ Pa and 17.4 Pa, torsions appeared at discharge powers as low as $P_{\mathrm{rf}} = 4$ W and 7 W, respectively, see Fig. 1. However, in the experimental run with $p_{\mathrm{Ar}} = 12$ Pa, the torsion formation was preceded by the onset of the mode-coupling instability at $P_{\mathrm{rf}} = 15$ W. Therefore, vertical pair formation and MCI are two competing scenarios for the crystal response to weakening vertical confinement.

To clarify the torsion formation mechanism, we studied how the main crystal parameters varied with discharge power, see Fig. 2. We interpret these findings in the following way. Particle pairs form when the screening length of the screened Coulomb interparticle interaction exceeds a threshold. That allows more distant neighbors of a particle to exert a force on it. Therefore, the interaction of a particle with neighbors other than nearest, is probably essential for triggering the particle pairing.

[*] Corresponding author: `V.Nosenko@dlr.de`

[1] V. Nosenko, S. K. Zhdanov, H. M. Thomas, J. Carmona-Reyes, and T. W. Hyde, Europhys. Lett. **112**, 45003 (2015).
[2] V. Nosenko, S. K. Zhdanov, H. M. Thomas, J. Carmona-Reyes, and T. W. Hyde, Phys. Rev. E **96**, 011201(R) (2017).

Photophoretic force on microparticles in complex plasmas

C.-R. Du,[1] V. Nosenko,[2,*] H. M. Thomas,[2] A. Müller,[3] A. M. Lipaev,[4] V. I. Molotkov,[4] V. E. Fortov,[4] and A. V. Ivlev[3]

[1] *College of Science, Donghua University, Shanghai 201620, PR China*
[2] *Institut für Materialphysik im Weltraum, Deutsches Zentrum für Luft- und Raumfahrt (DLR), 82234 Wesseling, Germany*
[3] *Max Plank Institute for Extraterrestrial Physics, Garching 85741, Germany*
[4] *Joint Institute for High Temperatures, Moscow 125412, Russia*

The PK-3 Plus laboratory was an experimental facility for the investigation of 3D complex plasmas under microgravity conditions on board of the International Space Station (ISS) [1]. The setup consisted of a vacuum chamber where capacitively coupled radio-frequency (rf) discharge in neon or argon was used to confine micrometer sized particles; illumination and imaging system for particle observation; and control system. Microparticles injected into the plasma under microgravity conditions were confined in the center of the chamber by the plasma fields, forming a 3D particle cloud.

Through years of experiments in the PK-3 Plus laboratory, we observed on multiple occasions that single particles would behave quite differently from the rest of the cloud [2], see Fig. 1. These "abnormal" particles often moved either with a much higher velocity or in a different direction compared with the surrounding particles. Their trajectories were rather random and did not appear to have been caused by the plasma electric field or ion drag force. These particles were trapped in either static or scanning illumination laser sheet. Their irregular trajectories may have resulted from a combined effect of the radiation pressure and photophoretic force exerted by the illumination laser. In the longitudinal direction, most of the "abnormal" particles moved along the laser direction, driven mainly by the radiation pressure force. In the transverse direction, their motion was rather random, which may be due to the photophoretic force.

To study the effect of photophoretic force quantitatively, we performed a series of dedicated experiments with a 2D complex plasma in the (ground-based) Gaseous Electronics Conference (GEC) rf reference cell [2]. The results show that the distribution of particle velocity has a larger high-speed tail for higher illumination laser powers. Comparing the particle velocity in the longitudinal and transverse directions with respect to the laser beam, little correlation was found. The optical microscopy study of the particles collected from the chamber after experiments suggests that the "abnormal" particles could be those with deformations or defects on their surface.

Combining the study of the morphology of microparticles with particle dynamics in both experimental devices, we attribute the driving mechanism of the "abnormal" particles to the photophoretic force. Photophoresis occurs when a particle is non-uniformly heated by a beam of light. The surrounding gas atoms colliding with a "hot spot" on the particle surface acquire higher temperature upon their accommodation. Their desorption leads to the net momentum transfer to the particle. Defects on the particle surface may strongly enhance the light absorption and therefore generate such hot spots. Since the defects have various shapes and are distributed randomly on the surface of those deformed particles, the photophoretic force is not necessarily aligned with the direction of the laser beam, resulting in uncorrelated irregular motion of a small fraction of the particles.

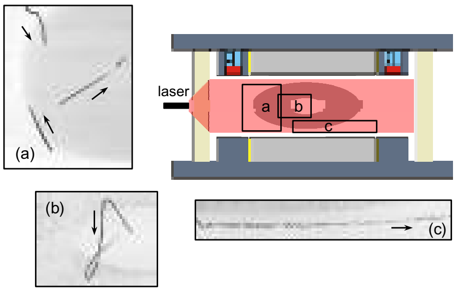

FIG. 1: Observation of "abnormal" particle trajectories in the PK-3 Plus laboratory on board of the ISS. A sketch of the PK-3 Plus chamber is provided, where a 3D particle cloud is illuminated by the laser sheet. Three examples are selected and shown in panels (a), (b), and (c), corresponding to the three regions marked in the sketch.

It can be easily shown that a temperature difference of a few degrees can already generate a considerable driving force. Assuming the particle radius is a and the effective radius of a "hot spot" on its surface is a_*, the net momentum transferred to the particle can be written as $F \sim \pi a_*{}^2 n_0 T_0 (n_* T_*/n_0 T_0 - 1)$, where n_0 and T_0 are the number density and temperature of gas respectively, and T_* is the temperature of the "hot spot". The density of absorbing atoms/molecules n_* is determined from the flux conservation $n_*\sqrt{T_*} = n_0\sqrt{T_0}$ and thus $n_*T_*/n_0T_0 = \sqrt{T_*/T_0} \geq 1$. From the balance with the Epstein drag $F_{ep} = 2\sqrt{2\pi} a^2 n_0 T_0 (u/v_{Tn0})$, where u is the particle velocity, we get $u/v_{Tn0} \sim (a_*/a)^2(\sqrt{T_*/T_0} - 1)$. For $\delta T = T_* - T_0 \ll T_0$, we have $u/v_{Tn0} \sim 0.3(a_*/a)^2(\delta T/T_0)$. For a small temperature difference $\delta T/T_* \sim 10^{-2}$ at a small "hot spot" $(a_*/a)^2 \sim 0.3$, the particle velocity can already reach $u \sim 10^{-3} v_{Tn0} \approx 30$ cm/s.

---

[*] Corresponding author: `V.Nosenko@dlr.de`

[1] H. M. Thomas, G. E. Morfill, V. E. Fortov *et al.*, New J. Phys. **10**, 033036 (2008).
[2] C.-R. Du, V. Nosenko, H. M. Thomas *et al.*, New J. Phys. **19**, 073015 (2017).

Moment fluid equations for ions in weakly ionized plasma

I. L. Semenov*

Institut für Materialphysik im Weltraum, Deutsches Zentrum für Luft- und Raumfahrt (DLR), 82234 Wesseling, Germany

Mathematical and numerical modelling of transport processes in weakly-ionized plasma plays an important role for better understanding the basic properties of low-pressure gas discharges. There are two main types of models for describing transport phenomena in partially-ionized plasma: kinetic and fluid (continuum) models.

Kinetic models are more preferable for describing the electron component in low-pressure discharges because non-equilibrium and non-local kinetic effects have a substantial influence on the electron distribution function. In contrast to the electrons the ion component in low-pressure discharges is more often described by means of the fluid equations. Despite the fact that these equations are not always based on an explicitly stated kinetic model they have been shown to give reasonable results under certain conditions. Nevertheless, two points can be made regarding the applicability and accuracy of the fluid equations for ions.

At first, it should be noted that these equations are generally formulated without considering the ion energy balance. In order to close the model, the pressure term in the ion momentum equation is neglected or assumed to be equal to that of the local Maxwellian distribution with the gas temperature. Since this assumption is not well justified in the presheath-sheath region, it might affect the accuracy of the model and must be examined carefully.

The second point to note is the approximation used for the velocity moments of the ion-neutral collision integral. A common approach in this case is to apply the well-known exchange relations with an effective collision frequency. The latter is usually evaluated as a function of the ion mean velocity using the data from the ion swarm experiments. It is worth noting that the experimental data are available only in a limited range of the electric fields and cannot be used to calculate the effective collision frequency in the entire range of the ion drift velocities.

In the present work we propose a one-dimensional fluid model for ions which partially overcomes the limitations discussed above. To address these limitations the following steps have been implemented. First, we consider the Monte-Carlo (MC) kinetic model of the ion swarm experiments to define the approximations of the collision terms in the fluid equations. Second, the ion energy equation is taken into account. The fluid equations are closed by applying a simple model of the ion distribution function.

The accuracy of the proposed fluid model is examined by comparing the predicted results with those obtained using the particle-in-cell simulation method combined with the Monte-Carlo collision model (PIC-MCC approach). In particular, a parallel plate model of the capacitively coupled radio-frequency (CCRF) discharge in argon and helium is considered (see Fig. 1). The comparison is presented for several test problems including the benchmarks [1] and experimental situations [2]. It has been shown that the results obtained using the proposed fluid model for ions are in good agreement with those obtained from the PIC-MCC simulations over a wide range of discharge conditions. The results of the present work can be applied for more effective modelling of low-pressure gas discharges used in the experiments with complex plasmas.

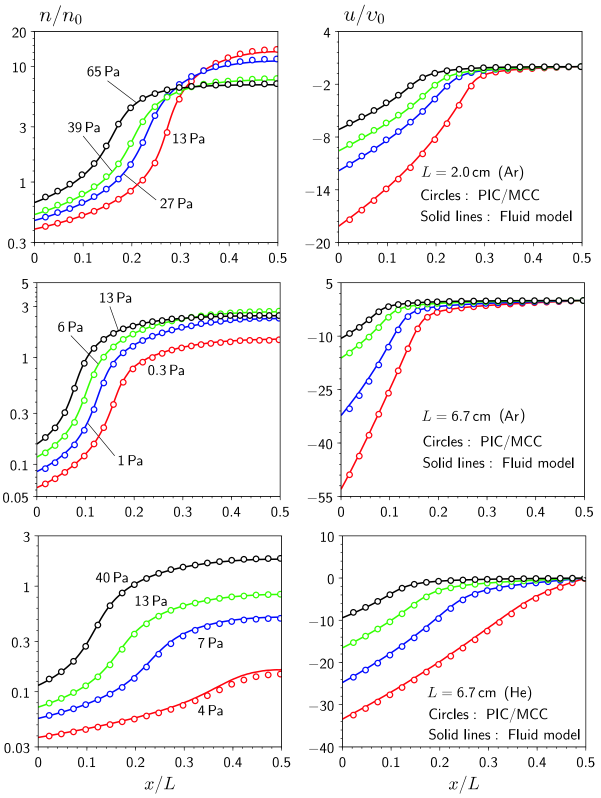

FIG. 1: Comparison between kinetic PIC-MCC simulations and fluid simulations based on the proposed fluid model for ions. Shown are distributions of the normalized ion number density (left) and velocity (right) near the left electrode of a parallel plate CCRF discharge with the length L. The results are presented for Ar and He at different gas pressures.

---

* Corresponding author: `Igor.Semenov@dlr.de`

[1] M. M. Turner, A. Derzsi, Z. Donko et al., Phys. Plasmas **20**, 013507 (2013).

[2] V. A. Godyak and R. B. Piejak, Phys. Rev. Lett. **65**, 996 (1990).

Momentum transfer cross-section for ion scattering on dust particles

I. L. Semenov,* S. A. Khrapak, and H. M. Thomas
Institut für Materialphysik im Weltraum, Deutsches Zentrum für Luft- und Raumfahrt (DLR), 82234 Wesseling, Germany

The elastic scattering of ions by charged dust particles has an important influence on properties of complex (dusty) plasmas. A proper accounting of the drag force exerted on dust particles by flowing ions (ion drag force) plays an essential role in explaining various experimental observations. Moreover, the effect of ion-dust collisions on the ion mobility might be a significant factor determining the confinement of dust clouds in complex plasmas.

If the electric potential around a dust particle can be assumed to be isotropic, the ion-dust collisions are described using the classical binary collision theory. This is justified, for example, when dust particles levitate in the bulk region of the plasma discharge (typical conditions in microgravity experiments). The binary collision approach allows one to calculate the momentum transfer cross-section and estimate the ion drag force.

A common approach adopted in the field of complex plasmas is to approximate the potential distribution around the dust particle using the Yukawa (screened Coulomb) model. One important factor limiting the applicability of the Yukawa model is related to the nonlinear effects associated with a strong coupling between the ions and highly charged dust particles. The nonlinear effects can be partially taken into account by choosing proper value of the screening length in the Yukawa potential [1]. The accuracy of this approach has been discussed in detail in [2]. It was demonstrated that the Yukawa model can significantly overestimate the potential at distances comparable to typical interparticle spacing in dust particle clouds.

In the present work we calculate the momentum transfer cross-section for the ion-dust collisions using a more accurate model potential proposed recently in [2]. This potential was derived for a single dust particle in isotropic collisionless plasma and was shown to be in good agreement with the solution of the Vlasov-Poisson equations. The obtained results are used to analyze the influence of the nonlinear screening effects on the ion-dust collision cross section. The nonlinearity of the particle screening is characterised by the parameter $\beta = (ak_{\rm D})(e|\varphi_{\rm p}|/kT_{\rm i})$, where a is the radius of the particle, $k_{\rm D}$ is the inverse plasma Debye length, $\varphi_{\rm p}$ is the particle potential and $T_{\rm i}$ is the ion temperature.

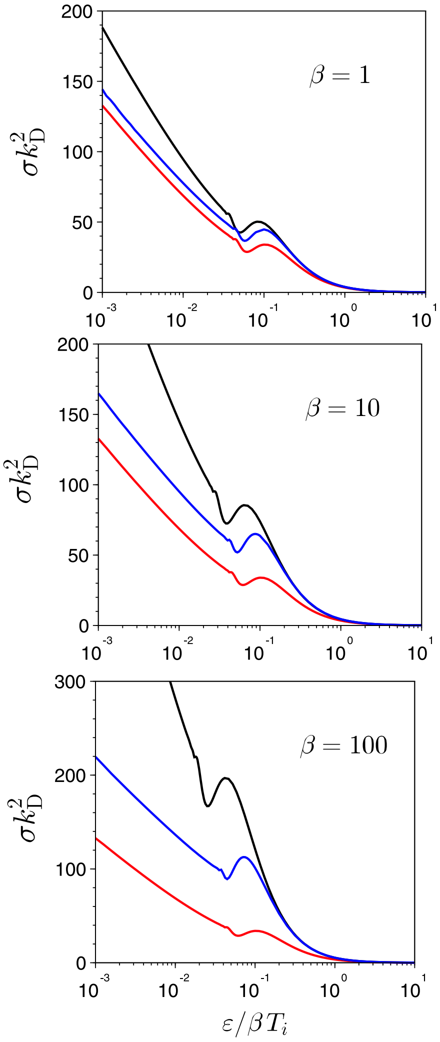

FIG. 1: The normalized cross section for ion-dust collisions as a function of the normalized collision energy. The lines of different colors correspond to different interaction potentials: the model of [2] (blue), the model of [1] (black) and conventional Yukawa potential (red).

In Fig. 1 we show the normalized momentum transfer cross-section as a function of the normalized collision energy for different potentials. It can be seen that the cross-section obtained using the Yukawa potential with the effective screening length (model of [1]) significantly overestimates the cross-section calculated for more accurate potential proposed in [2]. This is clearly observable in the nonlinear screening regime $\beta \gg 1$. Moreover, it can be also seen that the conventional Yukawa potential does not take into account properly the nonlinear screening effects. Therefore, accurate approximation of the potential distribution around the dust particle can play an important role in estimating the momentum transfer cross-section for the ion-dust collisions. This can be of special importance for analysing the recent results obtained from the PK-4 experiment onboard the International Space Station [3].

---

* Corresponding author: `Igor.Semenov@dlr.de`

[1] S. Ratynskaia, U. De Angelis, S. Khrapak et al., Phys. Plasmas **13**, 104508 (2006).
[2] I. L. Semenov, S. A. Khrapak, and H. M. Thomas, Phys. Plasmas **22**, 053704 (2015).
[3] M. Y. Pustylnik et al., Rev. Sci. Instrum. **87**, 093505 (2016).

Influence of microparticles on rf plasmas: experiments and simulation

M. Y. Pustylnik,* I.L. Semenov, E. Zähringer, and H.M. Thomas

Institut für Materialphysik im Weltraum, Deutsches Zentrum für Luft- und Raumfahrt (DLR), 82234 Wesseling, Germany

Microparticles immersed in a plasma affect its properties. They represent a volumetric sink of plasma particles shifting the ionization balance. They also play a significant role in the charge balance and therefore affect the electric fields in the plasma. In microgravity complex plasma experiments (e.g. PK3-Plus [1] or PK-4 [2]), the microparticles usually occupy significant fraction of its volume. Therefore, their influence on the background plasma cannot be neglected. Moreover, deep understanding of the interaction between plasma and microparticles immersed in it is required for the correct interpretation of the results of complex plasma experiments as well as for the development of future microgravity complex plasma facilities. We have studied the influence of the microparticles on the capacitively-coupled plasma both experimentally and using the numerical simulations.

The experiments were performed in a PK3-Plus chamber [1] with the disc-shaped electrodes of 6 cm diameter and 3 cm interelectrode gap. RF plasma was created in argon in the pressure range of 20-40 Pa. Melamineformaldehyde resin microspheres of 1.95 μm were injected into the plasma. To mimic microgravity conditions, they were supported against gravity by thermophoretic force originating from the controlled temperature difference of 17 K between the lower and upper electrodes. Microparticles were observed by illuminating them with a 532-nm laser sheet and registering the scattered light by a CMOS videocamera. The rf-period-resolved spatiotemporal profile of the plasma emission was recorded by an ICCD videocamera, synchronized (via the frequency divider) with the rf signal on the electrodes [3].

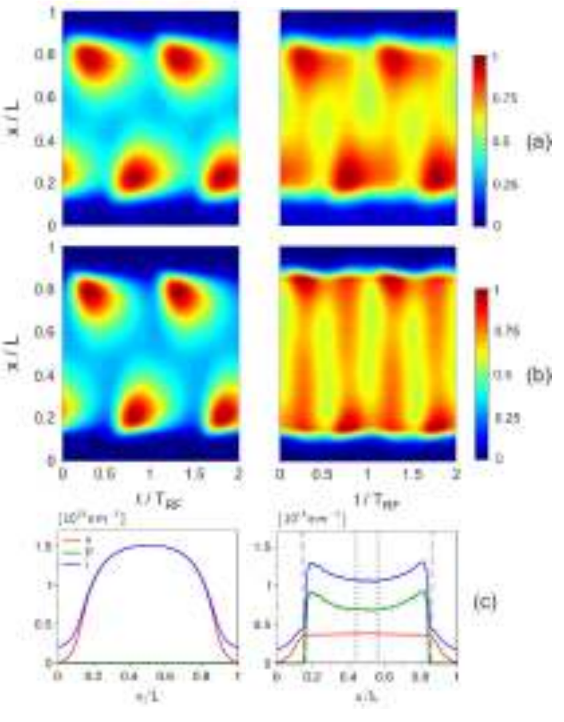

FIG. 1: Spatiotemporal emission patterns of the capacitively coupled rf discharge: (a) experiment and (b) simulations. (c) The rf-period-averaged charge density distributions for the electrons (red line), microparticles (green line) and ions (blue line) obtained from the simulations. Left column corresponds to the microparticle-free discharge. Right column corresponds to the discharge significantly affected by the presence of microparticles. Vertical dashed lines represent the exprerimentally observed boundaries of the microparticle cloud. Vertical dotted lines correspond to the experimentally observed axial void boundaries.

Simulations of the plasma were performed using the 1D hybrid (particle-in-cell for electrons and hydrodynamic for ions) approach described in Ref. [4]. For the microparticles, self-consistent charging and drift-diffusion equations were used. Losses of electrons and ions on the microparticle surfaces as well as the ion scattering on microparticles were included into the respective models. Only electrostatic and ion drag forces acting on the microparticles were taken into account. Microparticle charge density was also included into the Poisson equation.

Simulated and measured spatiotemporal emission profiles exhibit qualitatively the same tendency (Fig.1): introduction of microparticles into the plasma makes the emission profile spatially more uniform. In absence of microparticles, highly mobile electrons screen out the rf electric field. Microparticles bind the free electrons allowing rf electric field to penetrate much deeper into the plasma. In contrast to the experiment, simulated microparticle density distribution exhibits no void. Attempt to fix the microparticle distribution with a void (in the simulations) leads to unrealistic spatiotemporal emission pattern with an emission peak inside the void.

The observed discrepancies between experimental and numerical results can be attributed either to the two-dimensional effects or to the incorrect description of the sharp void boundary by a fluid model. These hypotheses can be verified by more detailed numerical simulations and depth-resolved optical plasma diagnostics, e.g., laser-induced fluorescence.

The authors appreciate helpful discussions with A. Zobnin.

* Corresponding author: `mikhail.pustylnik@dlr.de`

[1] H.M. Thomas, G.E. Morfill, V.E. Fortov et.al., New J. Phys. **10**, 033036 (2008)

[2] M.Y. Pustylnik, M.A. Fink, V.N. Nosenko et.al., Rev. Sci. Instrum. **87**, 093505 (2016)

[3] M.Y. Pustylnik, I.L. Semenov, E. Zähringer, H.M. Thomas, Phys. Rev. E **96**, 033203 (2017)

[4] I.L. Semenov, Phys. Rev. E **96**, 043208 (2017)

Wake-mediated propulsion of an upstream particle in two-dimensional plasma crystals

I. Laut,[1,*] C. Räth,[1] S. K. Zhdanov,[1] V. Nosenko,[1] G. E. Morfill,[2,3] and H. M. Thomas[1]

[1] *Institut für Materialphysik im Weltraum, Deutsches Zentrum für Luft- und Raumfahrt (DLR), 82234 Wesseling, Germany*
[2] *Max Planck Institute for Extraterrestrial Physics, 85741 Garching, Germany*
[3] *BMSTU Centre for Plasma Science and Technology, Moscow, Russia*

In ion beam physics, channeling effects can strongly influence the motion of ions or other charged particles in a crystalline solid. The channeling effect can also be observed in two-dimensional complex plasma crystals where, instead of slowing down, a so-called extra particle moves at an almost constant velocity through the crystal. In the present work we show that this intriguing effect can be reproduced in simulations with the simple model of a pointlike ion wake [1].

One large difference between classical solids and plasma crystals is that the latter constitute nonequilibrium systems that are driven by a radio-frequency plasma source. In a two-dimensional plasma crystal there is a strong ion flow, and the flowing ions are focused below each particle where they form a small positive excess charge, the so-called ion wake. A simple way to model the complicated wake structure is to assume a positive pointlike charge at a fixed distance below each negatively charged particle.

In the molecular-dynamics simulation the equation of motion for particle i reads:

$$M\ddot{\mathbf{r}}_i + M\nu\dot{\mathbf{r}}_i = \sum_{j\neq i}\mathbf{F}_{ji} + \mathbf{C}_i + \mathbf{L}_i, \qquad (1)$$

where $\mathbf{r}_i$ is the three-dimensional particle position, M the mass and ν the damping rate. The forces acting on the particle are the mutual particle interactions $\mathbf{F}_{ji}$, the confinement force $\mathbf{C}_i$ derived from an external potential, and a Langevin heat bath $\mathbf{L}_i$. In the pointlike wake model $\mathbf{F}_{ji}$ has two contributions, one is repulsive (between any two particles) and one is attractive (between a particle and a wake of another particle).

A top view of a channeling effect is shown in Fig. 1(a) and compared to the experiment of Ref. [2], shown in Fig. 1(b). The extra particle moves in a relatively straight line from the left to the right. During the passage of the extra particle, the particles in the crystal layer are attracted towards the extra particle and subsequently perform a circular motion. Despite the friction force the extra particle moves at a constant velocity. The simulated trajectory agrees well with the experimental data.

The fact that the particles that constitute the channel approach the extra particle during the passage can be explained by the ion wake model, and it is itself the key to understand the propulsion mechanism of the extra particle. The sketch shown in Fig. 1(c) gives an idea of the propulsion mechanism: During the passage of the extra particle floating above the crystal, the channel particles (large gray balls) are attracted to the wake charge (small black ball) of the extra particle and thus deform the channel. Due to this symmetry-breaking deformation, the repulsion force exerted by the channel particles on the extra particle is stronger behind the extra particle than in front of it, leading to a net propelling force acting on the extra particle.

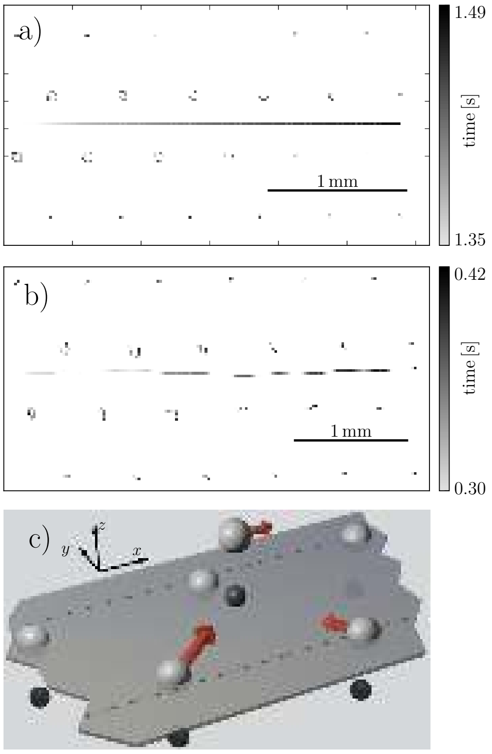

FIG. 1: Channeling of an extra particle moving from the left to the right in the simulations (a) and the experiments of Ref. [2] (b). The trajectories of the extra particle and the particles in the crystal that constitute the channel are color-coded with respect to time. (c) Sketch of the propulsion mechanism.

In the paper, we also estimate the terminal velocity of the extra particle and find a good agreement with the velocities observed in simulations and in experiments. In the future, the interaction of the extra particle with defects in the crystal can be addressed in the simulations.

This work was supported by the German Federal Ministry for Economy and Technology under grant No. 50WM1441.

[*] Electronic address: `Ingo.Laut@dlr.de`

[1] I. Laut, C. Räth, S. K. Zhdanov, V. Nosenko, G. E. Morfill, and H. M. Thomas, Phys. Rev. Lett. **118**, 075002 (2017).
[2] C.-R. Du, V. Nosenko, S. Zhdanov, H. M. Thomas, and G. E. Morfill, Europhys. Lett. **99**, 55001 (2012).

Density waves at the interface of a binary complex plasma

L. Yang,[1] M. Schwabe,[2,*] S. K. Zhdanov,[2] H. M. Thomas,[2] A. M. Lipaev,[3] V. I. Molotkov,[3] V. E. Fortov,[3] J. Zhang,[1] and C.-R. Du[1]

[1]*College of Science, Donghua University, 201620 Shanghai, PRC*
[2]*Institut für Materialphysik im Weltraum, Deutsches Zentrum für Luft- und Raumfahrt (DLR), 82234 Wesseling, Germany*
[3]*Joint Institute for High Temperatures, Russian Academy of Sciences, 125412 Moscow, Russia*

When waves travel across an interface, various interesting phenomena can occur, including transmission, reflection, and refraction. Studying the behavior of individual particles at interfaces has recently become possible with colloids [1] and granular media [2], but these systems do not allow for studies at the kinetic level due to the presence of rigid contacts in granular media and strong damping in colloids. Here, we report on the observation of density waves in complex plasmas that allow studying the transmission of waves across an interface between two media on the kinetic level.

The experiment was performed in the PK-3 Plus Laboratory [3], which was operated on board the International Space Station (ISS) from 2006 – 2013. Its heart consisted of a capacitively coupled plasma chamber, into which microparticles could be inserted with dispensers. A vertically spread laser beam illuminated the microparticles, and their movement was recorded with CCD cameras with a frame rate up to 50 fps. The microparticles acquired high charges and interacted with each other.

In order to study wave transmission across an interface, a binary complex plasma was produced containing melamine-formaldehyde microparticles of diameter 6.8 μm and 9.2 μm in an argon gas. The force balance that determines the position of the microparticles in the chamber depends on the particle radius. Thus, the particles arranged by size around a particle-free void in the center of the chamber [4]. As the pressure was lowered beneath a threshold, waves appeared [5]. The waves in the cloud made up of small particles were excited by oscillations of the void, while those in the large particles were caused by an ion streaming instability. The waves traveled from the void in the center of the cloud towards the edges, crossing the interface between the two subclouds. The wave frequency, wave length and speed were different in the two subclouds.

Figure 1(a) shows a space time plot (periodgram) of the microparticles near the interface. This diagram was produced by selecting a rectangular region of interest in the experimental images that is elongated in horizontal (x) direction and crosses the interface. For each time step and each x, the pixel intensity is summed along the vertical direction. This results in intensity plots $I(x)$ for every time step. These plots are arranged one after the other, producing periograms as in Fig. 1. The bright lines correspond to higher microparicle density, that is, the wave crests.

In the figure, some representative wave crests are marked with colored lines. It can be seen that some wave crests transmit across the interface, while others emerge there. We were able to identify a "collision zone" before the interface and a "merger zone" behind it, in which the dynamics of the waves change. Due to the "collision" when approaching the interface, the phase speed $|\nu|$ decreases for the transmitting waves, see Fig. 1(b). Accordingly, $|\nu|$ of the self-excited waves increases. This experiment can serve as first step towards a generic picture of wave transmission across an interface on the kinetic level.

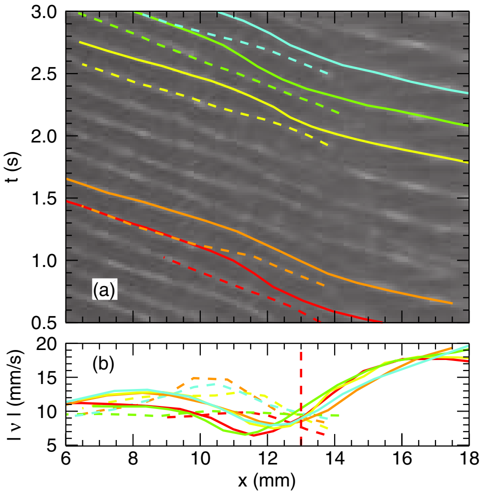

FIG. 1: Periodgram (space-time plot), and (b) phase speed of wave crests close to the interface between subclouds composed of 6.8 μm (left in the figure) and 9.2 μm particles (right). The transmitting wave crests are marked with solid lines, and the wave crests self-excited in the smaller particles with dashed lines. In (b), the interface is marked with a vertical dashed red line. From [5].

The PK-3 Plus Project was funded by the space agency of the Deutsches Zentrum für Luft- und Raumfahrt e.V. with funds from the Federal Ministry for Economy and Technology according to a resolution of the Deutscher Bundestag under grant No. 50WM1203.

[*] Corresponding author: `mierk.schwabe@dlr.de`

[1] J. Hernández-Guzmán, and E. R. Weeks, PNAS **106** 15198 (2009).
[2] V. F. Nesterenko, C. Daraio, E. B. Herbold, and S. Jin, Phys. Rev. Lett. **95**, 158702 (2005).
[3] H. M. Thomas, G. E. Morfill, V. E. Fortov, et al., New J. Phys. **10**, 033036 (2008).
[4] K. R. Sütterlin, A. Wysocki, A. V. Ivlev, et al., Phys. Rev. Lett. **102**, 085003 (2009).
[5] L. Yang, M. Schwabe, S. K. Zhdanov, H. M. Thomas, A. M. Lipaev, V. I. Molotkov, V. E. Fortov, J. Zhang, and C.-R. Du, EPL **117**, 25001 (2017).

Observation of metallic sphere – complex plasma interactions in microgravity

M. Schwabe,[1],* S. K. Zhdanov,[1] T. Hagl,[1] P. Huber,[1] A. M. Lipaev,[2] V. I. Molotkov,[2] V. N. Naumkin,[2] M. Rubin-Zuzic,[1] P. V. Vinogradov,[3] E. Zähringer,[1] V. E. Fortov,[2] and H. M. Thomas[1]

[1] Institut für Materialphysik im Weltraum, Deutsches Zentrum für Luft- und Raumfahrt (DLR), 82234 Wesseling, Germany
[2] Joint Institute for High Temperatures, Russian Academy of Sciences, 125412 Moscow, Russia
[3] Rocket Space Corporation 'Energia', 141070 Korolev, Moscow Region, Russia

All objects suspended in a plasma acquire charges by collecting ions and electrons from the plasma. This holds true for microparticles in a low temperature plasma such as a neon tube, and for dust particles in diffuse regions in the interstellar medium. There, plasma-mediated interactions might lead to the formation of dusty clumps [1]. In this paper [2], we investigate the interaction of millimeter-sized spheres with microparticles immersed in a low temperature plasma in the PK-3 Plus Laboratory on board the International Space Station [3]. The heart of the PK-3 Plus Laboratory consisted of a capacitively coupled plasma chamber which could be filled with argon or neon gas that was subsequently ionized by an alternating radio-frequency electric field. Microparticles were inserted into the plasma, charged up and were trapped in the chamber by ambipolar electric fields. The mixture of low temperature plasma and microparticles is called "complex plasma". The complex plasma was illuminated by a vertically elongated sheet of laser light, on which CCD cameras were focused that recorded the movement of the microparticles.

In the experiments presented here, argon gas at pressures between 15 and 30 Pa and microparticles with sizes between 1.6 and 15 μm were used. In addition to the microparticles, metallic spheres of 1 mm diameter were present in the complex plasma. The spheres moved through the plasma basically force-free. The cosmonaut who performed the experiment, Pavel Vinogradov, imparted momentum on the spheres by shaking the experimental container. The influence of the spheres on the complex plasma, however, was profound.

Figure 1 shows an experimental snap shot of the complex plasma containing spheres. The spheres are visible as large white circles. As they reflect much more light than the microparticles, they are visible even when they were not located in the laser sheet. When they transversed the laser sheet, they cast long shadows on the microparticle cloud. Counting the number of frames that these shadows were visible allowed estimating the transversal velocity of the spheres.

FIG. 1: Side view of a complex plasma containing microparticles (small white dots) and metallic spheres (larger white circles). The particles are illuminated from the left, which is why the spheres show a characteristic half moon. The cavity surrounding the sphere in the center right is caused by electric repulsion of the microparticles, while the large particle-free region in the right is due to plasma-specific effects. Field of view: $26 \times 36\,\mathrm{mm}^2$.

Both the spheres and the microparticles were charged negatively by strong electron fluxes onto their surfaces. When the microparticles were close to the spheres, they were correspondingly repelled by this strong charge and formed a cavity in the cloud surrounding the spheres (visible in the center right of Figure 1). At intermediate distances, the microparticles were attracted by the spheres. It was the ions that mediated this "repulsive attraction" – the ions were charged positively and were thus flowing towards the negatively charged spheres. The ion flux towards the spheres caused a drag force on the microparticles, which exceeded the strength of the electric repulsion at intermediate distances.

The strong effect of the spheres on the plasma ions can also be seen in experiments at lower pressure. Then, the electric field of the spheres was large enough that the total electric field crossed the threshold for wave excitation in the vicinity of the spheres.

Experiments like these shed light on the plasma-mediated interaction between micron-sized dust particles and larger objects. They would not be possible on Earth, as gravity would accelerate both microparticles and spheres downwards. This would compress the microparticle cloud and limit the interaction time between the objects.

The PK-3 Plus Project was funded by the space agency of the Deutsches Zentrum für Luft- und Raumfahrt e.V. with funds from the Federal Ministry for Economy and Technology according to a resolution of the Deutscher Bundestag under grant No. 50WM1203.

* Corresponding author: `mierk.schwabe@dlr.de`

[1] A. V. Ivlev, V. V. Akimkin, and P. Caselli, Astrophys. J. **833** 92 (2016).
[2] M. Schwabe, S. K. Zhdanov, T. Hagl, et al., New J. Phys. **19**, 103019 (2017).
[3] H. M. Thomas, G. E. Morfill, V. E. Fortov, et al., New J. Phys. **10**, 033036 (2008).

Instability onset and scaling laws of an auto-oscillating turbulent flow in a complex plasma

M. Schwabe,* S. K. Zhdanov, and C. Räth

Institut für Materialphysik im Weltraum, Deutsches Zentrum für Luft- und Raumfahrt (DLR), 82234 Wesseling, Germany

Turbulence is considered one of the last unsolved problems of modern physics. Research in turbulence is hindered by the fact that the carriers of the interaction are not directly observable, but tracer particles or simulations are used instead. However, understanding the mechanisms of turbulent energy, vorticity, and mass transfer between scales and between points in space will help understanding turbulence better and might even be profound enough to be considered a "solution to the mystery of turbulence" [1].

Here we report on experiments on the onset of turbulent movement in a complex plasma [2, 3]. Complex plasmas consist of microparticles embedded in a low temperature plasma. Ion and electron fluxes from the plasma strongly charge the microparticles, so that they acquire charges of several thousands of elementary charges. The microparticles are large enough, and their movement is slow enough to be imaged on the level of individual particles.

The experiment was performed in the PK-3 Plus Laboratory onboard the International Space Station [4]. Its heart consisted of a parallel plate, capacitively coupled plasma chamber. In the present experiment, the plasma chamber was filled with argon gas at a pressure of 9 Pa. Melamine formaldehyde particles with a diameter of 9.2 μm were injected into the plasma. The light from a laser was spread into a vertical plane which illuminated the microparticles. A digital camera was used to image the microparticle trajectories. We traced the microparticles from frame to frame, calculated their velocities, and the velocity distribution in space. From these velocity maps, it is possible to calculate the kinetic energy spectra (see [3] for details). Care was taken to avoid problems caused by missing data in the velocity maps, which would lead to errors in the spectra.

We calculated the spectra before and after the onset of an instability of the microparticle cloud called "heartbeat". In this instability, the central particle-free region of the microparticle cloud (the "void") oscillated radially, periodically pushing the microparticle cloud [5]. The result is shown in Fig. 1. Before the onset of the instability, the kinetic energy spectrum is best fitted with an exponential dependence (blue crosses). After the onset, it splits into two regions which can be fit with power laws $E \propto k^{-5/3}$ (wave numbers $k < k_{\text{exc}}$) and $E \propto k^{-3}$ ($k > k_{\text{exc}}$). This double spectrum reminds of that predicted for forced two-dimensional turbulence [6] (shown as inset in Fig. 1), even though our experiment was three-dimensional. We speculate that the movement of the microparticles was channeled into two dimensions by the heartbeat instability, but further experiments are needed to confirm this hypothesis.

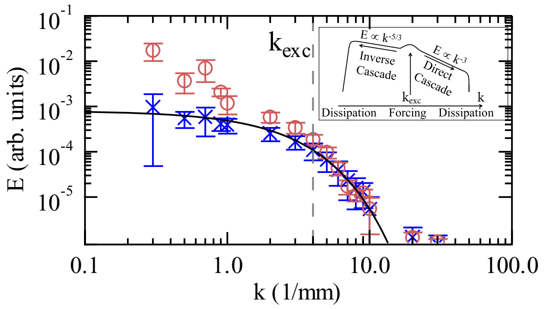

FIG. 1: Kinetic energy spectrum before (blue crosses) and after (red circles) the onset of an instability. Before, an exponential dependence fits the spectrum (solid line), indicating laminar flow. During the instability, the spectrum splits into two parts which can be described by power laws. The crossover occurs at the excitation wave number, k_{exc}. This reminds of the double spectrum predicted for forced two-dimensional turbulence (shown as inset). From [2].

Assuming that the spectrum we observed is indeed a double cascade as in forced two-dimensional turbulence, it is possible to calculate the wave number where the two ranges meet. This should correspond to the scale on which energy is put into the system, k_{exc}. Using the theoretical description of a double cascade [6], we arrive at $k_{\text{exc}} = 3.9\,\text{mm}^{-1}$, which fits very well with the position in the graph where the two regions meet. The scale estimated from the heartbeat frequency f_{HB} and the microparticle speed of sound C_{DAW} is $k_{\text{HB}} = 2\pi f_{\text{HB}}/C_{\text{DAW}} = 2.7\,\text{mm}^{-1}$.

These results demonstrate the potential of complex plasmas to serve as model systems to study turbulent fluids. In complex plasmas, the carriers of the interaction can be traced on the level of individual particles. This makes it potentially possible to study the energy and vorticity transport across scales, which might help shed light on the mechanisms of turbulence.

The PK-3 Plus Project was funded by the space agency of the Deutsches Zentrum für Luft- und Raumfahrt e.V. with funds from the Federal Ministry for Economy and Technology according to a resolution of the Deutscher Bundestag under grant No. 50WM1203.

---

* Corresponding author: `mierk.schwabe@dlr.de`

[1] R. Ecke, Los Alamos Science **29**, 124 (2005).
[2] M. Schwabe, S. Zhdanov, and C. Räth, Phys. Rev. E **95**, 041201(R) (2017).
[3] M. Schwabe, S. Zhdanov, and C. Räth, IEEE Trans. Plasma Sci. **PP**, 99 (2017).
[4] H. M. Thomas, G. E. Morfill, V. E. Fortov, et al., New J. Phys. **10**, 033036 (2008).
[5] R. J. Heidemann, L. Couëdel, S. K. Zhdanov, et al., Phys. Plasmas **18**, 053701 (2011).
[6] R. H. Kraichnan, Phys. Fluids **10**, 1417 (1967); C. E. Leith, Phys Fluids **11**, 671 (1968).

Fingerprints of different interaction mechanisms on the collective modes in complex (dusty) plasmas

Sergey Khrapak,[1,2,*] Boris Klumov,[2,3] and Hubertus Thomas[1]

[1] Institut für Materialphysik im Weltraum, Deutsches Zentrum für Luft- und Raumfahrt (DLR), 82234 Wesseling, Germany
[2] Aix Marseille University, CNRS, Laboratoire PIIM, Marseille, France
[3] Joint Institute for High Temperatures, Russian Academy of Sciences, Moscow, Russia

Complex plasma can be viewed as a classical system of individually visible strongly interacting particles. Relatively weak damping from the plasma background (dominated by the neutral gas) and the absence of hydrodynamic interactions make complex plasmas very suitable models to understand dynamics of simple atomic and molecular systems beyond the limits of continuous media. It has been recently recognized that this new class of soft matter – the "plasma state of soft matter" – can be used (complementary to other soft matter systems like colloids, granular medium, etc.) to investigate a broad range of important fundamental processes (equilibrium and non-equilibrium phase transitions, phase separation, self-organizations, rheology, waves, transport, etc.) at the most fundamental individual particle level.

As in most other interacting particle systems, the exact shape of the interaction potential between the particles is a key factor determining the rich variety of physical phenomena involved. In complex plasmas interactions are not fixed, but can vary considerably. In particular, the important property of complex plasmas - their thermodynamic openness (associated with continuous exchange of matter and energy between the particles and the surrounding plasma) - results in a remarkable diversity of interaction mechanisms. This diversity is not a problem, but rather an advantage: It widens the range of phenomena accessible for detailed investigation. The problem is the current state of our understanding: While considerable progress has been made in the last decade to understand basic properties of plasma-particle and particle-particle interactions theoretically, there is a lack regarding experimental confirmations of these findings.

The main purpose of this study has been to investigate in detail one of the possible relations between the exact shape of the interparticle interactions and phenomena relatively easily observable in experiments – dispersion of low-frequency waves. One of the most important conclusions from this study is that the conventional dispersion relation of the dust acoustic waves (DAW) is not an inherent property of complex (dusty) plasmas. The DAW dispersion operates when the interparticle interactions are of Yukawa (screened Coulomb) form. Deviations from the Yukawa potential result in deviations in the dispersion law.

In order to demonstrate this we have used the quasi-crystalline approximation (QCA) and derived the corresponding dispersion relations of the longitudinal waves for several representative pair interaction potentials, which can be operable in complex plasmas [1]. The interaction considered include double-Yukawa, Yukawa plus long-range Coulomb asymptote, and Yukawa plus long-range r^{-2} asymptote (all repulsive). Both, weakly coupled and strongly coupled regimes have been studied. In Fig. 1 examples of calculated dispersion relations (a) and q-dependent sound velocities (b) for several types of interactions which can operate in complex plasmas are shown. The comparison with the case of pure Yukawa interaction (dotted red curve) is also shown.

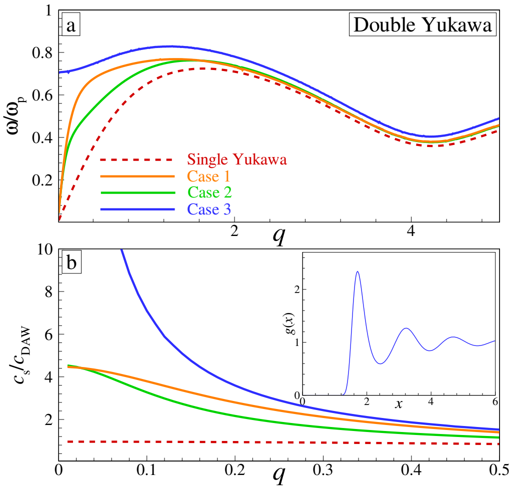

FIG. 1: (a) Dispersion relation $\omega(q)$ and (b) apparent sound velocity $c_{\rm s}(q)$ of three different realizations of double repulsive Yukawa potential (solid curves) in the strong coupling regime. Frequency is expressed in units of the plasma frequency scale $\omega_{\rm p}$ and the sound velocity in units of the DAW sound velocity $c_{\rm DAW}$. Dashed red curves correspond to the conventional DAW (single-Yukawa potential). The inset shows the radial distribution function $g(r)$ used in calculations [1].

Experimental observations of the longitudinal dust acoustic waves have a long-standing history. Careful analysis of the corresponding dispersion relations can be in principle used to verify the existence of deviations from the conventional Yukawa interactions in complex plasmas experimentally. Related studies are in progress.

This work was supported by the A*MIDEX project (Nr. ANR-11-IDEX-0001-02) funded by the French Government "Investissements d'Avenir" program managed by the French National Research Agency (ANR) and by the French-German PHC PROCOPE Program (Project No. 35325NA/57211784).

---

[*] Corresponding author: `sergey.khrapak@dlr.de`

[1] S. A. Khrapak, B. A. Klumov, and H. M. Thomas, Phys. Plasmas **24**, 023702 (2017).

Thermodynamics of two-dimensional Yukawa systems across coupling regimes

Nikita Kryuchkov,[1] Sergey Khrapak,[2,3,*] and Stanislav Yurchenko[1]

[1] *Bauman Moscow State Technical University, 2nd Baumanskaya Str. 5, 105005 Moscow, Russia*
[2] *Institut für Materialphysik im Weltraum, Deutsches Zentrum für Luft- und Raumfahrt (DLR), 82234 Wesseling, Germany*
[3] *Aix Marseille University, CNRS, Laboratoire PIIM, Marseille, France*

Systems of particles interacting via Yukawa (screening Coulomb, or Debye-Hückel) potential are widely found in nature. In the physics of soft matter, the Yukawa potential plays a particularly important role because it is traditionally used to describe interactions between ions in screening media (e.g. aqueous solutions of electrolytes), charged colloidal micro- and nano-particles in various solvents, at interfaces of fluid media, and between charged particles in complex (dusty) plasmas. In addition, Yukawa systems represent a useful model of classical interacting particles with the softness of interaction variable in a very wide range, from extremely soft Coulomb interaction (one-component plasma limit in the absence of screening) to the extremely steep interaction (hard spheres in the limit of very strong screening).

In this work, thermodynamics of two-dimensional Yukawa systems has been studied systematically using molecular dynamics (MD) simulations [1]. Simulations cover very broad parameter range spanning from a weakly coupled gaseous state to the strongly coupled fluid and crystalline states. Important thermodynamic quantities, such as internal energy and pressure, have been obtained and accurate fits have been proposed.

For weakly non-ideal gases, virial expansion with the two first terms retained has been shown to provide reasonably good estimate of the excess energy. For fluids simple fits have been proposed, examples are shown in Figure 1.

For crystals, in addition to numerical simulations, the recently developed shortest-graph interpolation method has been applied to describe pair correlations and hence thermodynamic properties. It is shown that the finite-temperature effects can be accounted for by using simple correction of peaks in the pair correlation function. The corresponding correction coefficients have been evaluated using MD simulation.

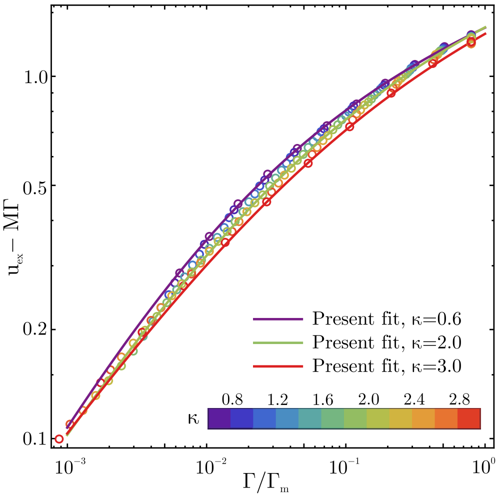

FIG. 1: Dependence of the excess thermal energy $u_{\rm th}$ on the reduced coupling parameter $\Gamma/\Gamma_{\rm m}$. Circles correspond to the data obtained from numerical simulations. Solid curves correspond to proposed fits. For details see Ref. [1].

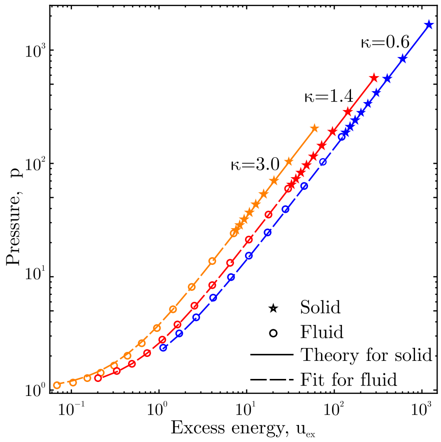

FIG. 2: Dependence of the reduced pressure on the reduced excess energy. Open (solid) symbols are the results of MD simulations for fluids and solids, respectively. The solid and dashed curves correspond to the shortest-graph method for solids and to the proposed fit for fluids. For details see Ref. [1]

Figure 2 shows the dependence of the reduced pressure on the reduced excess energy for both fluid and solid phases. The solid and dashed curves correspond to the shortest-graph method for solids and to the fits used to describe thermodynamics of the fluid phase.

The results of this study can be useful for thermodynamic calculations related to various phenomena in 2D and quasi- 2D Yukawa fluids and solids in a broad range of parameters. In particular, this includes colloidal systems, complex (dusty) plasmas, and liquid electrolytes.

This work was supported by the Russian Science Foundation (Projects Nr. 14-29-00277 and 14-43-00053), Russian Foundation for Basic Researches (Project Nr. 16-38-00952), and by the A*MIDEX project (Nr. ANR-11-IDEX-0001-02) funded by the French Government "Investissements d'Avenir" program managed by the French National Research Agency (ANR).

---

[*] Corresponding author: `sergey.khrapak@dlr.de`

[1] N. P. Kryuchkov, S. A. Khrapak, and S. O. Yurchenko, J. Chem. Phys. **146**, 134702 (2017).

Grüneisen parameter for strongly coupled Yukawa systems

Sergey Khrapak[1, 2, *]

[1] *Institut für Materialphysik im Weltraum, Deutsches Zentrum für Luft- und Raumfahrt (DLR), 82234 Wesseling, Germany*
[2] *Aix Marseille University, CNRS, Laboratoire PIIM, Marseille, France*

An equation of state (EoS) in the form of a relation between the pressure and internal energy of a substance (often referred to as the Grüneisen or Mie-Grüneisen equation) has been proven very useful in describing condensed matter under extreme conditions. Central to this form of EoS is the Grüneisen parameter, whose thermodynamic definition is

$$\gamma_{\rm G} = V\frac{(\partial P/\partial T)_V}{(\partial E/\partial T)_V} = \frac{V}{C_V}\left(\frac{\partial P}{\partial T}\right)_V, \qquad (1)$$

where V is the system volume, P is the pressure, T is the temperature, E is the internal energy, and $C_V = (\partial E/\partial T)_V$ is the specific heat at constant volume. Under the assumption that $\gamma_{\rm G}$ is independent of P and E one can write

$$PV = \gamma_{\rm G}(\rho)E + C(\rho)V, \qquad (2)$$

where $C(\rho)$ is the "cold pressure", which depends only on the density $\rho = N/V$.

Grünesein parameter depends considerably on the substance in question as well as on the thermodynamic conditions (location on the corresponding phase diagram). In most metals and dielectrics in the solid phase, $\gamma_{\rm G}$ is in the range from $\simeq 1$ to $\simeq 4$. For fluids it is usually somewhat smaller, typically ranging from $\simeq 0.2$ to $\simeq 2$ [1]. The focus of this paper is on Yukawa model systems, which are often applied as a first approximation to complex (dusty) plasmas, representing a collection of highly charged particles immersed in a neutralizing environment. It is desirable to have a practical approach allowing to estimate the Grüneisen parameter and related quantities under different experimental conditions. In this work, the Grüneisen parameter for strongly coupled three-dimensional (3D) one-component Yukawa systems has been evaluated [2].

The Grüneisen parameter has been estimated using simple and reliable analytical expressions for the energy and pressure of strongly coupled Yukawa fluids proposed recently in Refs. [3, 4]. These expressions are based on the Rosenfeld-Tarazona (RT) scaling of the thermal component of the excess internal energy when approaching the freezing transition. They demonstrate relatively good accuracy and are very convenient for practical applications. The resulting Grüneisen gamma is shown in Fig. 1 on the plane of (κ, $\Gamma/\Gamma_{\rm m}$) parameters. Here κ is the screening parameter (defined as the ratio of the interparticle distance to the screening length) and $\Gamma/\Gamma_{\rm m}$ is the reduced coupling parameter ($\Gamma_{\rm m}$ corresponds to the coupling parameter at the fluid-solid phase transition).

The Grüneisen parameter evaluated here can potentially be useful in the context of shock-wave experiments in complex (dusty) plasmas. It appears in the expressions relating the pressure and density jumps across a shock wave front (known as Hugoniot equations). Main applicability conditions are (i) shock-waves are excited in three dimensional particle clouds, (ii) the Yukawa potential is a reasonable representation of the actual interactions between the charged particles under these conditions, (iii) there is no or weak dependence of particle charge on particle density, and (iv) the screening length is not very much smaller compared to the mean interparticle separation. These conditions can (at least partially) be met in complex plasma experiments in microgravity conditions, e.g., in the PK-4 laboratory, currently operational onboard the International Space Station.

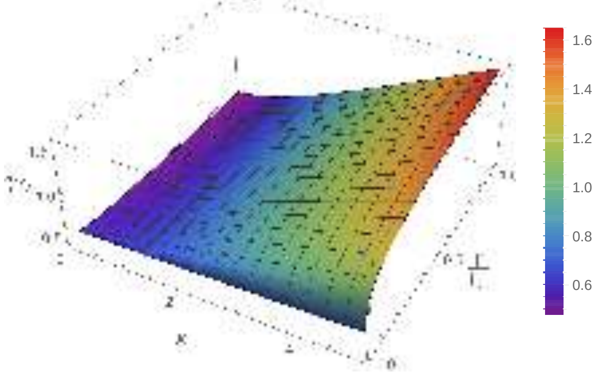

FIG. 1: Plot of the Grüneisen gamma parameter, $\gamma_{\rm G}$, on the plane (κ, $\Gamma/\Gamma_{\rm m}$). For details see Ref. [2].

This work was supported by the A*MIDEX project (Nr. ANR-11-IDEX-0001-02) funded by the French Government "Investissements d'Avenir" program managed by the French National Research Agency (ANR).

---

[*] Corresponding author: `sergey.khrapak@dlr.de`

[1] V. Arp, J. M. Persichetti, G. B. Chen, J. Fluid. Eng. **106**, 193 (1984).
[2] S. A. Khrapak, Phys. Plasmas **24**, 043706 (2017).
[3] S. Khrapak and H. Thomas, Phys. Rev. E **91**, 023108 (2015).
[4] S. Khrapak, N. Kryuchkov, S. Yurchenko. and H. Thomas, J. Chem. Phys. **142**, 194903 (2015).

Collective modes in simple melts: Transition from soft spheres to the hard sphere limit

Sergey Khrapak,[1,2,*] Boris Klumov,[2,3] and Lenaic Couedel[2]

[1] *Institut für Materialphysik im Weltraum, Deutsches Zentrum für Luft- und Raumfahrt (DLR), 82234 Wesseling, Germany*
[2] *Aix Marseille University, CNRS, Laboratoire PIIM, Marseille, France*
[3] *Joint Institute for High Temperatures, Russian Academy of Sciences, Moscow, Russia*

We have studied collective modes in a classical system of particles with repulsive inverse-power-law (IPL) interactions in the fluid phase, near the fluid-solid coexistence (IPL melts). The IPL exponent has been varied from $n = 10$ to $n = 100$ to mimic the transition from moderately soft to hard-sphere-like interactions. We have compared the longitudinal dispersion relations obtained using molecular dynamic (MD) simulations with those calculated using the quasi-crystalline approximation (QCA). The comparison is presented in Figure 1. The main results from this study can be formulated as follows (for details see Ref. [1]):

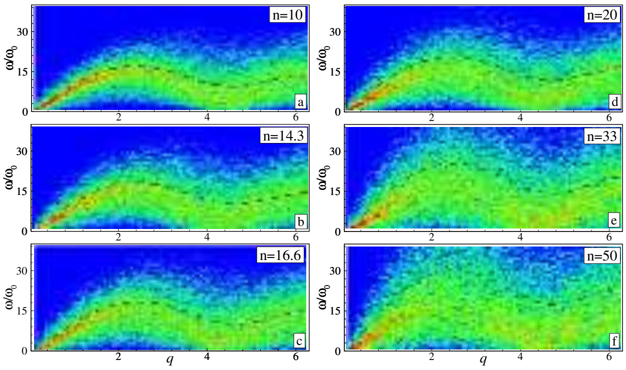

FIG. 1: Dispersion relations of the longitudinal mode in IPL melts. The frequency is measured in units of $\omega_0 = v_T/a$, where $v_T = \sqrt{T/m}$ is the thermal velocity, the reduced wave-number is $q = ka$, and a is the Wigner-Seitz radius. The color background corresponds to the longitudinal current fluctuation spectrum from MD simulations (the intensity increases from blue to red). The dashed lines are the results of calculation using QCA theoretical model. The results are shown for six different IPL exponents n indicated in figures. For details see Ref. [1].

(i) The QCA description of collective modes fails for sufficiently steep interactions; For the IPL model considered here this failure occurs at $n \sim 20$ (see Fig. 1).

(ii) For softer potentials QCA can provide a reasonable description of the high-frequency portion of the longitudinal dispersion relation (in particular, in the vicinity of the first maximum); However, the QCA elastic sound velocity overestimates the actual sound velocity.

(iii) The instantaneous sound velocity, evaluated using the instantaneous bulk modulus, is an appropriate measure of the actual (adiabatic) sound velocity observed in MD simulations (see Fig. 2); This instantaneous sound velocity (C_∞) is related to the elastic longitudinal (C_L) and transverse (C_T) sound velocities of the QCA approach via $C_\infty^2 = C_\mathrm{L}^2 - \frac{4}{3}C_\mathrm{T}^2$.

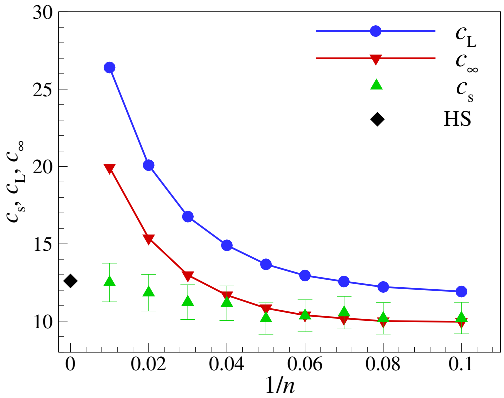

FIG. 2: Sound velocity of IPL melts versus the inverse IPL exponent $1/n$ (softness parameter). The green data (up triangles) correspond to the (adiabatic) sound velocities obtained directly from MD simulations (c_s), the blue data (circles) are the sound velocities obtained using QCA model (c_L), and the red data (down triangles) show the instantaneous sound velocities c_∞. The black diamond at $n = \infty$ corresponds to the adiabatic sound velocity of the hard sphere fluid at the fluid-solid coexistence. All velocities are expressed in units of the thermal velocity v_T. For details see Ref. [1].

(iv) In the limit of soft interactions (not considered here, but previously extensively studied using Coulomb and Yukawa model systems), the strong inequality $C_\mathrm{L} \gg C_\mathrm{T}$ generally holds, which implies that the longitudinal QCA sound velocity, instantaneous sound velocity, and the thermodynamic sound velocity are all close to each other;

(v) The conventional expressions for high frequency (instantaneous) elastic moduli should not be employed in the hard-sphere interaction limit, where they diverge.

The main finding can also be briefly reformulated as follows. The QCA model was formulated originally to describe collective motion in simple fluids without any explicit limitations regarding the shape of the interaction potential. It turns out, however, that this model works very well for soft interactions (in particularly in the plasma-related context), but fails when the interaction becomes sufficiently steep. We have located this failure here using the IPL family of potentials.

This work was supported by the A*MIDEX project (Nr. ANR-11-IDEX-0001-02) funded by the French Government "Investissements d'Avenir" program managed by the French National Research Agency (ANR).

---

[*] Corresponding author: `sergey.khrapak@dlr.de`

[1] S. A. Khrapak, B. A. Klumov, and L. Couedel, Sci. Rep. **7**, 7985 (2017).

1.6 Theory and Simulation

Crystal Growth under Fluid Flow

Hailong Peng,[1,2] Dieter M. Herlach,[1,2] and Thomas Voigtmann[1,3,*]

[1] *Institut für Materialphysik im Weltraum, Deutsches Zentrum für Luft- und Raumfahrt (DLR), 51170 Köln, Germany*
[2] *Experimentalphysik IV, Ruhr-Universität Bochum, Universitätsstraße 150, 44780 Bochum, Germany*
[3] *Department of Physics, Heinrich-Heine-Universität Düsseldorf, Universitätsstraße 1, 40225 Düsseldorf, Germany*

The nucleation and the growth of crystalline phases from the melt are greatly affected by processing conditions. In particular fluid flow dramatically modifies nucleation rates [1]. In simple model systems, the rates are found to depend non-monotonically on the shear rate [2]. Regarding the subsequent growth of the crystalline phase, the interplay of the quiescent driving force favoring the crystal with shear-induced surface erosion leads to a nonequilibrium coexistence line in the temperature–flow-rate plane [3, 4].

We study the way the crystal-growth velocity $v_I(T;\dot\gamma)$ depends on both temperature T and the shear rate $\dot\gamma$ imposed on the fluid [6]. Using molecular-dynamics simulations of a model of Al-Ni seeded with a planar interface between a crystalline B2 structure and the liquid, we find that $v_I(T;\dot\gamma)$ in this congruently melting system displays four qualitatively different regimes as a function of $\dot\gamma$, as shown in Fig. 1.

At low shear rate, crystal growth is either suppressed or enhanced with increasing shear rate (regime i), depending on temperature. At large shear rates (regime ii), v_I is a decreasing function of $\dot\gamma$ that approaches a temperature independent master curve for low temperatures. This regime is entered once the shear rate is fast compared to the rate of structural relaxation in the equilibrium fluid, i.e., the Weissenberg number $Wi = \dot\gamma\tau \gtrsim 1$. At still higher shear rates, we observe a coexistence regime (iii) that becomes broader in the sense that at low temperatures, $v_I \approx 0$ holds for an increasing shear-rate window. Finally, at the highest shear rates we simulated (regime iv), the observed growth velocity $v_I < 0$, i.e., the crystal shrinks as it is shear-molten.

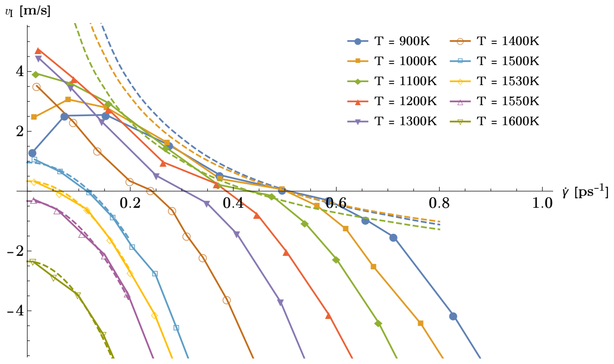

FIG. 1: Growth velocity v_I of a Al-Ni planal crystal interface into the surrounding fluid, as a function of temperature T (as labeled) and the shear rate $\dot\gamma$ imposed on the fluid, obtained from molecular-dynamics simulations. Regions where $v_I > 0$ imply that the system crystallizes, while for $v_I < 0$, the initially seeded crystal melts and the system is fluidized.

Several microscopic mechanisms are responsible for these different regimes. The non-monotonic regime (i) and the nearly temperature-independent regime (ii) can be linked to the nonlinear-response properties of the strongly supercooled fluid, whose dynamics is governed by the shear rate as the only relevant time scale once $\dot\gamma\tau \gg 1$. The weak temperature dependence of $v_I(\dot\gamma)$ in regime (ii) signals in particular that here, the crystal-growth mechanism is dominated by kinetic effects in the fluid, rather than changes in the effective thermodynamic free energy. Only in regime (iv), the melting of the crystal can be understood in terms of thermodynamics, recalling that there the shear fluid can be assigned an effective temperature $T_{\text{eff}}(\dot\gamma) > T_m$, where T_m is the equilibrium melting temperature.

Empirically, the growth velocity is often expressed in terms of a Wilson-Frenkel growth law [5],

$$v_I = v_\infty\left(1 - e^{-\beta\Delta\mu}\right)\,, \qquad (1)$$

where $\Delta\mu$ is the equilibrium chemical-potential difference between the phases (a *thermodynamic* driving force), and v_∞ is used to model *kinetic* driving forces. This empirical law becomes questionable in non-equilibrium situations and thus in the presence of flow. Nevertheless, regime (i) can be rationalized in terms of an effective Wilson-Frenkel law: here, for temperatures sufficiently below the melting point, kinetic slowing down in the fluid is responsible for a reduced growth velocity at strong undercooling. Weak shear flow causes the mobility of particles in the fluid to increase in this regime, and thus $v_I(\dot\gamma)$ increases with increasing $\dot\gamma$. The subsequent regime (ii) indicates a regime where the Wilson-Frenkel law can no longer be applied: v_I decreases although increasing shear flow still increases the kinetic prefactor. We conclude that in this regime, the balance between increased mobility and increased surface erosion due to shear flow determines the growth velocity.

We acknowledge funding from Deutsche Forschungsgemeinschaft, grant number He 1601/26.

[*] Corresponding author: `thomas.voigtmann@dlr.de`

[1] D. Richard and T. Speck, Sci. Rep. **5**, 14610 (2015).
[2] B. Lander, U. Seifert, and T. Speck, J. Chem. Phys. **138**, 224902 (2013).
[3] S. Butler and P. Harrowell, Nature (London) **415**, 1008 (2002).
[4] M. Ramsay and P. Harrowell, Phys. Rev. E **93**, 042608 (2016).
[5] H. A. Wilson, Philos. Mag. **50**, 238 (1900); j. Frenkel, Phys. Z. Sowjetunion **1**, 498 (1932).
[6] H. L. Peng, D. M. Herlach, and Th. Voigtmann, Phys. Rev. Materials **1**, 030401(R) (2017).

Model for the Chemotactic Motion of a Random Walker in a Porous Medium

Th. Voigtmann[1, 2, *] and T. Schilling[3]

[1] Institut für Materialphysik im Weltraum, Deutsches Zentrum für Luft- und Raumfahrt (DLR), 51170 Köln, Germany
[2] Institut für Physik, Heinrich-Heine Universität Düsseldorf, Universitätsstraße 1, 40225 Düsseldorf, Germany
[3] Physikalisches Institut, Albert-Ludwigs-Universität Freiburg, 79104 Freiburg, Germany

Bacteria often seek food in fluid-filled porous materials, directing their motion to regions of higher food concentration. Understanding such "chemotactic" motion is of importance for the physics of biological systems in general, but also for applications such as groundwater decontamination (where an unwanted pollutant is food to the bacteria) or microbial enhanced oil recovery (where microbes feed on long hydrocarbon chains found in underground oil reservoirs, breaking them up into the valuable light crude oil).

Generic aspects of self-propelled motion can be studied within simple lattice models. We address the dynamics of a chemotactic random walker [1] in a disorderded environment of obstacles (Fig. 1). The walker biases its movement to nearby places where it encounters "food", which it then consumes. The setup on a two-dimensional square lattice resembles the famous 1980s arcade game PAC-MAN®.

The random walk on a lattice with independently randomly blocked sites (with probability $1-p$) is a well known model for transport in porous media [2, 3]. The accessible sites form a fractal structure, and this causes "anomalous" dynamics, i.e., non-trivial power laws in the transport properties. At a critical p_c, a system-spanning percolating cluster appears in the infinite system. The mean-squared displacement (MSD) of an unbiased random walker confined to this cluster follows $\delta r^2(t) \sim t^{2\nu}$ for $t \to \infty$, with an exponent $\nu \approx 0.347$ below the $\nu = 1/2$ obtained for the free random walk.

We simulate the process using a Monte Carlo algorithm. At each time step, the walker jumps to one of the nearest-neighbor sites following the probabilities

$$p_{j\leftarrow i} = \left(\sum\nolimits_{k\sim i} \exp F_k\right)^{-1} \exp F_j \qquad (1)$$

where $F_k = F > 0$ if there is food at site k, and the sum runs over all nearest-neighbor sites.

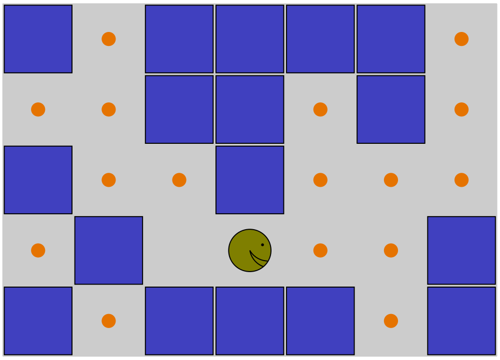

FIG. 1: Sketch of the model. Dark squares are obstacles, small circles are food, and the large circle is the random walker.

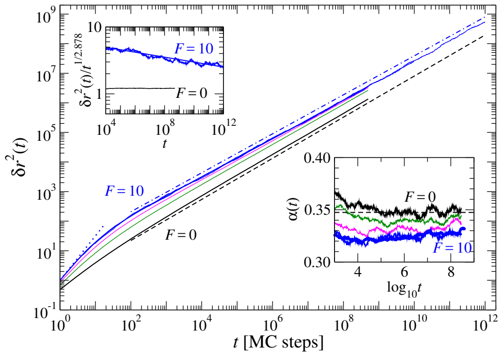

FIG. 2: Mean-squared displacement $\delta r^2(t)$ of the pacman walker on the 2D percolating cluster for various food propensities F (increasing from top to bottom). Dashed and dash-dotted lines indicate power-law anomalous diffusion. Lower right inset: effective exponent $\alpha(t) = d\log\delta r^2(t)/d\log t$.

Figure 2 shows the MSD for various food propensities. $F = 0$ recovers the asymptotic power law of the unbiased walk (dashed line). For $F > 0$, the walk initially spreads out faster, as intuitively expected. But its long-time asymptote is described by a power law (dash-dotted line) that grows *slower* than the one for the unbiased walk ($\nu \approx 0.33$ for $F = 10$). Our simulations suggest that the corresponding power-law exponent decreases continuously with increasing F, in contrast to the expectation from many statistical-physics models of criticality, where exponents usually belong to universality classes and do not change continuously.

Our analysis suggests that this slowing down occurs because the chemotactic walker "gets stuck in culs-de-sac": the percolating cluster is composed of a low-dimensional backbone, and a fractal distribution of dangling ends. Long-range transport requires motion along the backbone, but chemotaxis draws the walker deeper into the dangling ends than would be typical for the unbiased walker. Since the dangling ends appear in a fractal size distribution, this is a scale-free renormalization of the transport process, and hence changes the power law describing anomalous transport.

We thank T. Franosch and G. Peccati for discussoins. PAC-MAN is a registered trademark of BANDAI NAMCO Entertainment, Inc., Japan.

[*] Corresponding author: `thomas.voigtmann@dlr.de`

[1] T. Schilling and Th. Voigtmann, J. Chem. Phys. **147**, 214905 (2017).
[2] D. Stauffer and A. Aharony, *Introduction to Percolation Theory*, revised 2nd ed. (Taylor & Francis, London, 1994).
[3] S. Havlin and D. Ben-Avraham, Adv. Phys. **36**, 695 (1987).

Mode Coupling Theory of Active Brownian Particles

Alexander Liluashvili* and Thomas Voigtmann
Institut für Materialphysik im Weltraum, Deutsches Zentrum für Luft- und Raumfahrt (DLR), 51170 Köln, Germany

The collective dynamics of self-propelled particles and the related behavior of dense suspensions of microswimmers have received strong attention in the past few years. The physical principles of this dynamics are relevant for many biophysical questions. The collective dynamics of cells, bacteria colonies, or that found in the cell cytoskeleton show slow dynamics. It can be associated to the slow dynamics that arises from crowding effects at high densities and from the approach to a glass or jamming transition.

One of the simplest theoretical models in this context is that of active Brownian particles (ABP). We consider a system of hard disks in 2 dimensions having a self-propulsion velocity in the direction of their own orientation. The dynamics obeys overdamped Langevin equations for the positions $\boldsymbol{x}_i$, and the orientations φ_i.

$$d\vec{x}_i = D_t\vec{F}_i dt + v_0\vec{o}_i dt + \sqrt{2D_t}d\vec{W}_i^x\,, \tag{1}$$

$$d\varphi_i = \sqrt{2D_r}dW_i^\varphi\,, \tag{2}$$

where D_t and D_r are diffusion coefficients, and $\vec{o}_i = (\cos\varphi_i, \sin\varphi_i)^T$ are the orientation vectors. The forces interpaticle forces $\vec{F}_i$ are assumed to derive from a potential, and the dW are independent white-noise processes. The coefficient v_0 quantifies the self propulsion of the particles. The dynamical behavior is characterized by the angle-resolved density correlations

$$\boldsymbol{S}_{l,l'}(\boldsymbol{q},t) = \frac{1}{N}\left\langle \rho_l(\boldsymbol{q})^* e^{\Omega^\dagger t}\rho_{l'}(\boldsymbol{q})\right\rangle, \tag{3}$$

where $\Omega^\dagger$ is the time-evolution (Smoluchowski) operator of the system. The density fluctuations are given by $\varrho_l(\vec{q}) = \sum_{k=1}^N \exp[i\vec{q}\cdot\vec{r}_k]\exp[il\varphi_k]$.

A Zwanzig-Mori procedure leads to evolution equations of the form

$$\begin{aligned}\partial_t\boldsymbol{S}(t) &= -\hat{\boldsymbol{\omega}}\boldsymbol{S}^{-1}\boldsymbol{S}(t)\\ &- \int_0^t dt'\boldsymbol{m}^\mathsf{T}(t-t')\,\hat{\boldsymbol{\omega}}_\mathsf{T}^{-1}\left[\partial_{t'}\boldsymbol{S}(t') + \hat{\boldsymbol{\omega}}_\mathsf{R}\boldsymbol{S}(t')\right].\end{aligned} \tag{4}$$

Here, $\hat{\boldsymbol{\omega}} = \hat{\boldsymbol{\omega}}_\mathsf{T} + \hat{\boldsymbol{\omega}}_\mathsf{R}$ is a matrix characterizing the short-time motion in the translational and rotational degrees of freedom, and $\boldsymbol{S} \equiv \boldsymbol{S}(0)$ is the equilibrium static structure factor of the system. The appearance of the rotational contribution $\hat{\boldsymbol{\omega}}_\mathsf{R}$ in the integral is a consequence of the fact that orientational motion in the ABP model fully decouples from the translational motion (but not vice versa), and hence never arrests. We approximate the memory kernel $\boldsymbol{m}^\mathsf{T}$ using a mode-coupling approximation [1]. The resulting set of equations is solved numerically.

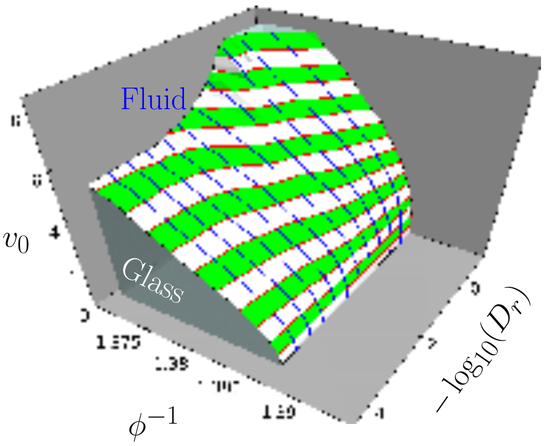

FIG. 1: Glass-transition surface for active Brownian hard disks, in terms of inverse density ϕ^{-1}, self-propulsion speed v_0, and persistence of the motion, $1/D_r$.

Figure 1 shows the glass transition surface in the three-dimensional parameter space spanned by the packing fraction ϕ, the self-propulsion velocity v_0, and the persistence time of self propulsion $1/D_r$ (quantifying the typical time after which a particle's direction becomes randomized). The results are in qualitative agreement with simulations of a tissue model [2].

One finds that increasing self-propulsion speed shifts the glass transition to higher densities and softens the glass. Decreasing the persistence time $1/D_r$, the effect of self propulsion becomes weaker, and for $1/D_r \to 0$, it becomes entirely ineffective; the model then matches that of a passive colloidal glass. As shown in the figure, for $1/D_r$ aobve a certain value, the glass transition is determined by ϕ and v_0 alone. This arises once the persistence length of swimming, $\ell_p = v_0/D_r$ exceeds the typical size of nearest-neighbor cages.

A further discussion of the dynamical solutions of the MCT for ABP is presented in Ref. [1]. Because orientational motion of ABP never freezes, the active glass is qualitatively different from its passive counterpart. The usual MCT-based description of glassy arrest (in terms of a critical power law and the so-called von Schweidler power law governing the divergence of the structural relaxation time of the fluid) needs to be reassessed.

We acknowledge funding from DFG, SPP 1726 project Vo 1270/7-1, and computing time granted by the John von Neumann Institute for Computing and provided on the supercomputer JURECA (project HKU26).

---

* Corresponding author: `alexander.liluashvili@dlr.de`

[1] A. Liluashvili, J. Ónody, and Th. Voigtmann, Phys. Rev. E **96**, 062608 (2017).
[2] D. Bi, X. Yang, M. C. Marchetti, and M. L. Manning, Phys. Rev. X **6**, 021011 (2016).

Active Brownian Particles in Crowded Media

J. Ónody[1] and Th. Voigtmann[1, 2]

[1] *Institut für Materialphysik im Weltraum, Deutsches Zentrum für Luft- und Raumfahrt (DLR), 51170 Köln, Germany*[*]
[2] *Fachgruppe Physik, Heinrich-Heine Universität, Düsseldorf, Germany*

In order to investigate the collective dynamics of microswimmers, e.g. to describe the experiment shown in figure 1, we discuss a system of *Active Brownian disks* in two dimension embedded in a model porous background. The microswimmers are modeled by hard disks in two dimension undergoing translational and rotational diffusion. Additionally they show an active swim mechanism with constant velocity along their direction of orientation (*cf.* results of A. Liluashili [1] for homogeneous background). The model is extended to a porous background modeled by fixed hard disks as discussed for the scenario of passive spheres (in 3d) by V. Krakoviack (*cf.* [2]). The setting is shown in figure 2.

The central quantity of the system (for N microswimmers) is the so called *density-density-correlator* (matrix form) describing whether it behaves like a fluid or like a glass (finite long-time value):

$$\begin{aligned} S_{\vec{q},l,l'}(t) &= \frac{1}{N}\overline{\left\langle \rho^*_{\vec{q},l}\rho_{\vec{q},l'}(t)\right\rangle} \\ &= \frac{1}{N}\overline{\left\langle \rho^*_{\vec{q},l}\right\rangle\left\langle \rho_{\vec{q},l'}(t)\right\rangle} + \frac{1}{N}\overline{\left\langle \delta\rho^*_{\vec{q},l}\delta\rho_{\vec{q},l'}(t)\right\rangle} \\ &= S^b_{\vec{q},l,l'}(t) + S^c_{\vec{q},l,l'}(t) \end{aligned} \tag{1}$$

Here, $\rho_{\vec{q},l}(t)$ is the Fourier transformed microscopic density with wave vector $\vec{q}$ and angular momentum index l ($\delta\rho$: density fluctuation). Due to the porous background we have to deal with two subsequently applied average, the *braket*-average for the microswimmer and the *bar*-average for all possible obstacle-configurations. The b is indicating *blocked*, while c stands for *connected*, corresponding to the part of the microswimmers that is able to propagate through the whole backbone of the environment.

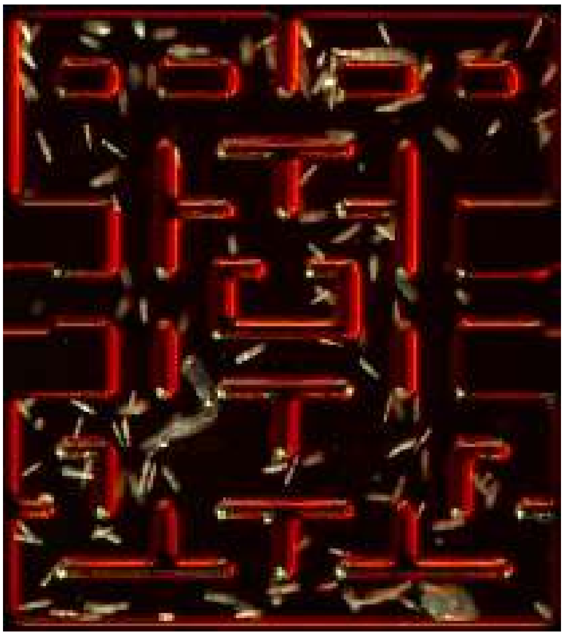

FIG. 1: Experiments with real bacteria modeling *Pacman* done by workgroup of Prof. E. A. Johannessen, Departement of Micro and Nano System Technology, Unversity College of Southeast Norway. Source: *youtube.com*.

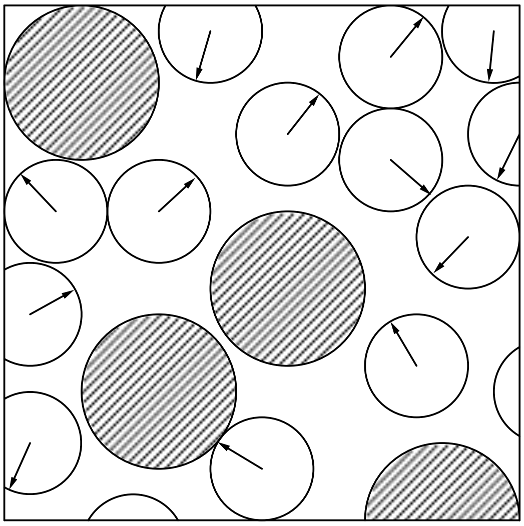

FIG. 2: Setting: Active hard disks embedded in a model porous background (hatched).

Making use of the *Mori-Zwanzig* projection-operator formalism one finds coupled evolution equations for the blocked $S^b(t)$ and the connected density correlator $S^c(t)$. They have the typical form of integro-differnetial equations where the occuring *memory kernels* can be approximated by the *Mode-Coupling Theory*-approximations (*cf.* [3]). They show a much more complicated structure with many more contributions compared to the separated cases.

As a next step the numerics for the full theory have to be established which is currently in progress.

[*] Corresponding author: `jonathan.onody@dlr.de`

[1] Liluashvili, A., Ónody, J., and Voigtmann, Th., Mode Coupling Theory for Active Brownian Particles, Phys. Rev. E **96**, 062608 (2017).
[2] Krakoviack, V., Mode-coupling theory for the slow collective dynamics of fluids adsorbed in disordered porous media, Phys. Rev. E **75**, 031503 (2007).
[3] Götze, W., Complex Dynamics of Glass-Forming Liquids - A Mode-Coupling Theory.

Mode-Coupling Theory for Active Brownian Particles: Anisotropic and Sheared Systems

J. Reichert[1] and Th. Voigtmann[1,2]

[1] *Institut für Materialphysik im Weltraum, Deutsches Zentrum für Luft- und Raumfahrt (DLR), 51170 Köln, Germany**
[2] *Fachgruppe Physik, Heinrich-Heine Universität, Düsseldorf, Germany*

We use the model of Active Brownian hard disks to describe the dynamics of microswimmers. In this model, a colloidal particle undergoes translational and rotational diffusion combined with an additional constant driving force along an orientational vector which evolves with the rotational diffusion of the particle. Based on this model, we use the Mode-Coupling theory (MCT) [3] to numerically solve the equation of motion of the Fourier-transformed non-equilibrium density-density correlator matrix, defined as

$$S_{\vec{q},l,l'}(t) := \frac{1}{N}\left\langle \rho^*_{\vec{q},l}\,\rho_{\vec{q},l'}(t)\right\rangle , \tag{1}$$

where $\rho_{\vec{q},l}(t)$ is a Fourier-transformed microscopic density mode with wavevector $\vec{q}$ and l corresponds to the orientation index. The density-density correlator plays an important role in the context of glass-forming liquids and describes the transition from an ergodic fluid state to a non-ergodic glass state. The theory of Active Brownian hard disks has been succesfully combined with the MCT to show, how activity is able to melt the glass and shift the transition point to higher densities [1]. However, in this model the particles are assumed to be perfectly spherical, which is not true for most microswimmers like bacteria which have an elongated shape and are influenced by steric interactions (see figure 1). For high densities particles can additionaly be blocked in their orientational degrees of freedom. By introducting interactions depening on the orientation of the particles, we receive additonal coupling terms between translational and rotational degrees of freedom in the equation of motion. These terms have been successfully calculated yet, however they cause numerical instabilites in solving the equation of motion, so a new solving scheme has to be established and is still under progress.

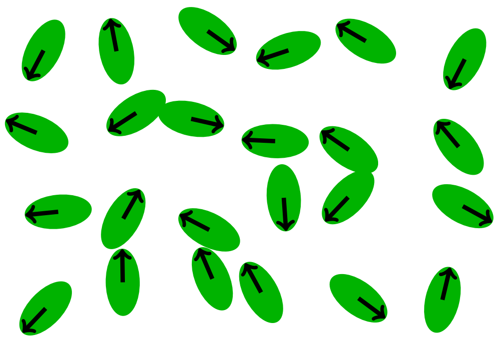

FIG. 1: Active Brownian particles with an elliptical shape

In a second project, we use again MCT to investigate Active Brownian hard disks under steady shear flow. By introducing an even infinitesimal shear flow, long time correlations break down and the systems remains ergodic for all densities, in contrast to the active driving force which can only melt the glass for sufficiently high values. The effects of shearing have already been demonstrated by Fuchs and Cates in the case of Passive Brownian hard disks, where MCT has successfully been applied to systems under homogeneous steady shear flow (see [2] and figure 2). We adapt their simplified model called "Isotropically Sheared hard disk model" and combine it with the MCT for Active Brownian hard disks. In a next step the obtained density-density correlators can be used as an input to calculate macroscopic quanitities like the viscosity of the system making use of the Integraion Through Transients (ITT) formalism from what we hope to learn more about the rheology of active systems. ITT has already be proven to be successfull in calculating the non-equilibrium swim velocities from which we were able to predict the Motility-induced phase seperation of the system.

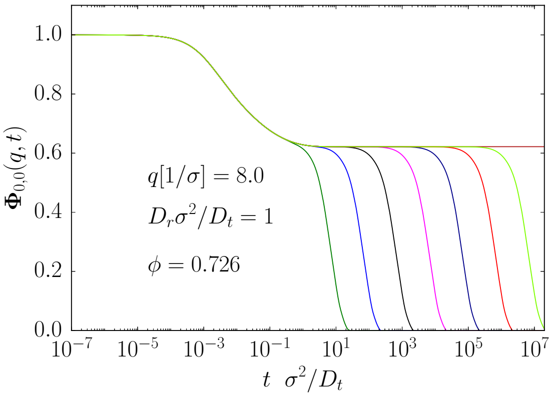

FIG. 2: Normalized density-density correlator for Passive Brownian hard disks under shear flow. The applied shear-rate varries from $\gamma = 1e-1$ (left) to $\gamma = 1e-7$ (right). Red is the system without shear. We see that γ sets the timescale for structural relaxation.

* Corresponding author: `Julian.Reichert@dlr.de`

[1] Liluashvili, A., Ónody, J., and Voigtmann, Th., Mode Coupling Theory for Active Brownian Particles, Phys. Rev. E **96**, 062608 (2017).
[2] Fuchs, M., Cates, M.E., A mode coupling theory for brownian particles in homogeneous steady shear flow, Journal of Rheology, 53 (957) (2009).
[3] Götze, W., Complex Dynamics of Glass-Forming Liquids – A Mode-Coupling Theory

Glassy dynamics in highly asymmetric binary mixtures of hard-spheres

L. F. Elizondo Aguilera^{1,*} and Th. Voigtmann^{1,2}

^{1}*Institut für Materialphysik im Weltraum, Deutsches Zentrum für Luft- und Raumfahrt (DLR), 51170 Köln, Germany*
^{2}*Department of Physics, Heinrich-Heine-Universität Düsseldorf, Universitätsstraße 1, 40225 Düsseldorf, Germany*

We investigate the glass transitions in highly asymmetric binary mixtures of HS. The main goal consist in unravel the dynamical mechanisms that lead to different arrested states and to unify the understanding of the glassy dynamics of the mixture. We present experimental, simulational and theoretical joint evidence for the distinct dynamical arrest transitions observed in highly asymmetric colloidal binary mixtures. This study confirms the occurrence of a single glass of big particles, in which the small species remains mobile, and a double glass in which both components arrest simultaneously. All techniques evidence consistently that the transitions to the different glassy states can be distinguished mainly through the dynamics of the small spheres, which in turn influence significantly the dynamics of the large spheres. It thus demonstrates the need for a full two- component description of the glass transition in binary mixtures.

The dynamically arrested states diagram of a binary mixture of hard spheres, with $\delta \approx 0.2$, and as a function of the control parameters (ϕ_b, ϕ_s), i.e., the volume fractions of, respectively, big and small spheres is presented in Fig. 1. Here $\phi_i \equiv \frac{\pi}{6}\rho_i\sigma_i^3$ $(i = s, b)$, where $\rho_i \equiv N_i/V$ denotes the corresponding particle number density. Details of the determination of such diagram are provided in Ref. [1]. In Fig. 1 we also display different state points that we have studied in this work by means of both MD simulations (*paths A* and *B*) [3] and experimental techniques (*paths* $1(+), 2(*)$ and $3(\times)$) [4]

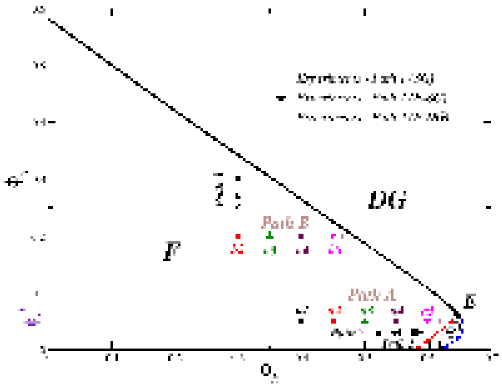

FIG. 1: Dynamical arrest diagram for a binary mixture of HS with size ratio $\delta \equiv \sigma_s/\sigma_b \approx 0.2$, as a function of the volume fractions of small, ϕ_s and big, ϕ_b, spheres. Lines are predictions of the SCGLE theory [1]. The (black) solid line indicates the transitions from the fluid (***F***) to the double glass (***DG***) state. The (red) dashed line indicates the separation between the (***F***) and the *single* glass (***SG***) states. The (blue) dashed-dotted line shows the transition from the ***SG*** to the double glass ***DG*** state. Two different paths obtained at constant ϕ_s are shown: *Paths A* ($\phi_s = 0.05$) and *B* ($\phi_s = 0.2$). The state points $a1$-$a5$ and $b1$-$b4$ along each path represents data studied in this work with MD simulations. *Path* 1 (+) corresponds to the experimental data of Ref. [4], whereas *Paths* 2 (∗) and 3 (×) correspond to experimental data obtained in this work.

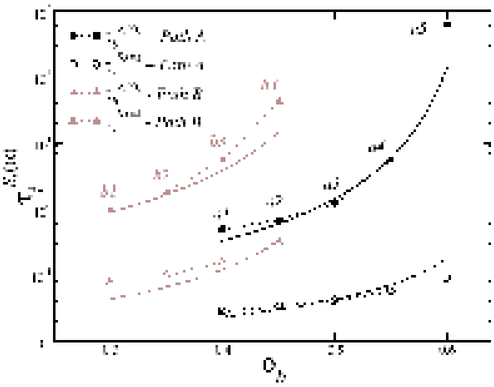

FIG. 2: *Self* α-relaxation times of both species along the two *paths* in Fig.1. For *path A*, the behavior of $\tau_b^{S,(\alpha)}$ (solid circles-MD, solid line-SCGLE) and $\tau_s^{S,(\alpha)}$ (open circles-MD, dashed line-SCGLE) with increasing ϕ_b seems uncorrelated and suggests a dynamical decoupling of each species. In *path B*, $\tau_b^{S,(\alpha)}$ (solid triangles-MD, solid line -SCGLE) and $\tau_s^{S,(\alpha)}$ (open triangles-MD, dashed line -SCGLE) display the same qualitative behavior with increasing ϕ_b.

To reach our goal we have investigated both *self* and collective dynamical properties, of the two species, and along the points indicated in Fig. 1. More specifically, we have studied the mean square displacements (MSDs), self and collective intermediate scattering functions (ISFs) combining the three aforementioned techniques. A remarkable consistency between MD and theory is observed, which also describes the trends of the experiments. The analysis of the correlation- time and wave vector dependence of this quantities reveals the main features of each of the two transitions from region ***F***- ***PG*** and from ***F***-***DG***, briefly illustrated in Fig. 2 in terms of the behavior of the so- called self α-relaxation times.

L.F.E.A. acknowledge financial support from the German Academic Exchange Service (DAAD) through the DLR-DAAD programme under grant No. 212.

[*] Corresponding author: `luisfer.elizondo@gmail.com`

[1] R. Juárez-Maldonado and M. Medina-Noyola, *Phys.Rev. E.*, **77**, 051503 (2008).
[2] T. Voigtmann, EuroPhys. Lett. **96** (2011), 36006.
[3] E. Lázaro-Lázaro, *et.al. J. Chem. Phys.*, **146** 184506 (2017).
[4] T. Sentjabrskaja, *et al.,* Nat. Comm. 7:11133 doi: 10.1038/ncomms11133 (2016).

Glass-Transitions in Dipolar Fluids

L. F. Elizondo Aguilera[1,*] and Th. Voigtmann[1,2]

[1] *Institut für Materialphysik im Weltraum, Deutsches Zentrum für Luft- und Raumfahrt (DLR), 51170 Köln, Germany*
[2] *Department of Physics, Heinrich-Heine-Universität Düsseldorf, Universitätsstraße 1, 40225 Düsseldorf, Germany*

We have carried out extensive molecular dynamics simulations for a model system representing a dipolar fluid consisting in N rigid spheres interacting through a truncated dipole-dipole potential. By monitoring the behavior of the generalized density correlation functions, $F^{S}_{lm;l'm'}(k,t)$, the mean square displacement, $W_T(t) =< [\Delta\mathbf{r}(t)]^2 >$, and the angular mean square deviations $W_\theta(t) =< \theta^2(t) >$ and $W_{\sin\theta}(t) =< \sin^2\theta(t) >$, we discuss the dynamical arrest of the translational (TDF) and orientational (ODF) degrees of freedom of the model.

We find three types of transitions in our model: *(i)* the simultaneous dynamical arrest of both TDF and ODF, occurring at low and intermediate concentrations upon cooling down the system, and where two different types of *frozen* structures are observed, namely, dipolar percolating chains and liquid-like structures; *(ii)* an ordinary glass transition for the translational motion, occurring at high densities and high temperatures, and where the orientations remain ergodic; and *(iii)* the subsequent arrest of the ODF in a *positionally-frozen* but disordered structure, occurring at high densities and intermediate temperatures. Our findings suggest, thus, the existence of three different transition lines in the state space of the system, spanned by the two parameters (η, T), where η denotes the volume fraction occupied by the particles and T the corresponding temperature, and describing the dynamical arrest of different correlation functions, $F_{lm;lm}(k,t)$ and the mean square deviations, $W_T(t) =< [\Delta\mathbf{r}(t)]^2 >$, $W_\theta(t) =< \theta^2(t) >$ and $W_{\sin\theta}(t) =< \sin^2\theta(t) >$, which characterize the dynamical behavior of the system.

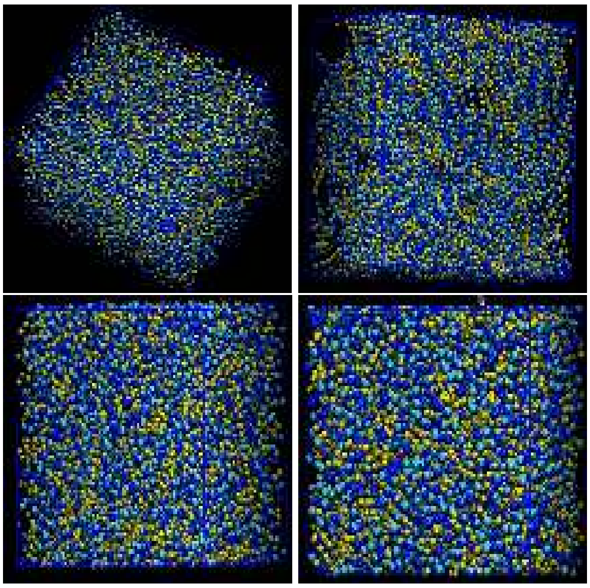

FIG. 1: (Color online) Simulation snapshots for the state points: (a) $\eta = 0.2, T = 2$ (upper left), (b) $\eta = 0.2, T = 0.02$ (upper right), (c) $\eta = 0.4, T = 0.05$ (lower left), and (d) $\eta = 0.6, T = 0.1$ (lower right). Blue color is used to represent *big* particles whereas yellow accounts for the *small* species. Dark and light shading indicates particles orientation

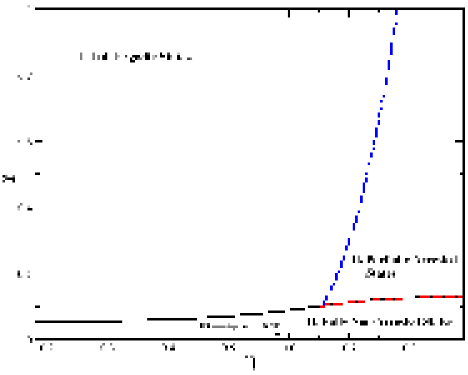

FIG. 2: Arrested phases diagram for the dipolar soft-sphere fluid as provided by the SCGLE theory [1] using, as an input, the solution of the Ornstein-Zernike equation combined with the soo -called Sharma-Sharma approximation for the static structure factors [2]. In the inset of this figure we show a comparison of these results with those obtained with the MCT [3]

The physical scenario emerging from our simulations is discussed and compared with independent results obtained in the context of the so-called self consistent generalized Langevin equation theory, from which we obtain a fully consistent physical picture.

Acknowledgments

L.F.E.A. acknowledge financial support from the German Academic Exchange Service (DAAD) through the DLR-DAAD programme under grant No. 212.

[*] Corresponding author: `luisfer.elizondo@gmail.com`

[1] L.F. Elizondo-Aguilera, P. F. Zubieta Rico, H. Ruiz Estrada and O. Alarcón-Waess, Phys. Rev. E, **90** 052301, (2014).
[2] R.V. Sharma and K.C. Sharma, Physica A **89**, 213 (1997).
[3] R. Schilling and T. Scheidsteger, *Phys. Rev. E* **56** 2932 (1997).
[4] C. G. Gray and K. E. Gubbins, *Theory of Molecular Fluids Vol I: Fundamentals*, Oxford University Press, New York, (1984).

On the generalized generalized Langevin equation

H. Meyer,[1] T. Schilling,[1] and Th. Voigtmann[2, 3, *]

[1] *Physikalisches Institut, Albert-Ludwigs-Universität Freiburg, 79104 Freiburg, Germany*
[2] *Institut für Materialphysik im Weltraum, Deutsches Zentrum für Luft- und Raumfahrt (DLR), 51170 Köln, Germany*
[3] *Institut für Physik, Heinrich-Heine Universität Düsseldorf, Universitätsstraße 1, 40225 Düsseldorf, Germany*

In a classical many-particle system, one would usually like to measure only a restricted set of "relevant" variables, such as those that correspond to the slow evolution of observable bulk quantities, while one desires to "integrate out" the fast fluctuating degrees of freedom. In the context of a large particle moving in a bath of small solvent molecules, Langevin [1] first suggested to model the slow evolution of a relevant variable $A(t)$ in terms of slowly varying systematic forces and a "random force" with very short correlation time. In the limit that this random force is delta-correlated in time, one obtains what is now called the *Langevin equation*, and one of the most prominent stochastic Markov processes, the Ornstein-Uhlenbeck process [2]. In thermal equilibrium, stationarity of this process enforces that the white-noise correlation strength and the friction acting on $A(t)$ are directly connected, with the thermal energy kT setting the prefactor. This is often referred to as (a specific) fluctuation-dissipation theorem (FDT).

More formally, the correlation function of the noise must be related to the memory kernel $K(t)$ describing time-retarded friction on the dynamical variable, leading to the *generalized Langevin equation*

$$\partial_t A(t) = \omega A_t + \int_0^t K(t-t')A(t')\,dt' + \eta(t)\,, \tag{1a}$$

where ω is a (possibly vanishing) drift coefficient. The FDT states that the noise $\eta(t)$ obeys

$$K(t) = -\frac{\langle \eta^*(t)\eta(0)\rangle}{\langle |A|^2\rangle}\,. \tag{1b}$$

In the 1960's, Zwanzig and Mori [3, 4] introduced a projection-operator formalism as a systematic way to deduce such generalized Langevin equations for the evolution of arbitrary dynamical variables based on the microscopic equations of motion of a system. The Mori-Zwanzig formalism immediately yields an evolution equation for dynamical correlation functions $C(t) = \langle A^*(0)A(t)\rangle$, noting that the fluctuating force $\eta(t)$ is orthogonal to $A(t')$ at all t, t'. Various approximation schemes for the memory kernel then exist, such as the mode-coupling theory (for long time tails, or MCT for the glass transition) or related theoretical approaches.

The investigation of transport phenomena in non-equilibrium situations calls for a generalization of these statements to non-stationary time-dependent processes. A particular application arises in computer simulation studies, where a system is somehow prepared in a non-equlibrium state and then evolved under the equilibrium dynamics. This is common in studies of slowly relaxing systems (for example glasses) where an initial quench from a high-temperature equilibrium state to low temperatures provides the non-equilibrated initial conditions.

A formal extension of the projection-operator technique to non-equilibrium situations has been developed by Grabert [5] in the context of quantum mechanics. They are also the starting point of theoretical descriptions of aging glassy systems [6]. In a recent work [7], we adapted Grabert's projection-operator technique to the time evolution of quenched classical many-particle system, to obtain a *generalized generalized Langevin equation*,

$$\partial_t A_s(t) = \omega(t)A(t) + \int_s^t K(t,\tau)A_s(\tau)\,d\tau + \eta_s(s,t)\,, \tag{2a}$$

where $s < t$ is an arbitrary reference time where one starts tracking the time evolution of $A(t)$. This explicit reference becomes necessary in non-stationary situations to specify the initial point of correlation functions $C(t,s) = \langle A_s(0)^* A_s(t)\rangle$. The memory kernel can be shown to obey a generalized FDT-like relation,

$$K(t,\tau) = -\frac{\langle \eta_\tau^*(\tau,\tau)\eta_\tau(\tau,t)\rangle}{\langle |A_\tau(\tau)|^2\rangle}\,. \tag{2b}$$

All the quantities that appear in these equations can be formally defined in terms of the Liouville operator that drives the dynamics of the system (see Ref. [7]).

In the context of molecular-dynamics simulations, the memory kernel $K(t,\tau)$ can be expanded for small time differences, since in the simulation, the evolution of $A(t)$ is tracked over small time increments. We have performed simulations on well-controlled test cases to demonstrate the feasibility of this approach to construct systematic coarse-graining procedures for simulation [7].

This project was supported by the National Research Fund Luxembourg (FNR) within the AFR-PhD programme, and by computing time at the HPC facility of the University of Luxembourg.

[*] Corresponding author: `thomas.voigtmann@dlr.de`

[1] M. P. Langevin, Comptes Rend. Acad. Sci. **146**, 530 (1908).
[2] G. E. Uhlenbeck and L. S. Ornstein, Phys. Rev. **36**, 823 (1930).
[3] R. Zwanzig, Phys. Rev. **124**, 983 (1961).
[4] H. Mori, Prog. Theor. Phys. **33**, 423 (1965).
[5] H. Grabert, *Projection Operator Techniques in Nonequilibrium Statistical Mechanics* (Springer, Berlin, 1982).
[6] A. Latz, J. Stat. Phys. **109**, 607 (2002).
[7] H. Meyer, Th. Voigtmann, and T. Schilling, J. Chem. Phys. **147**, 214110 (2017).

2 Publications and Patents

2.1 Peer-Reviewed Publications

[1] A. Amon, P. Born, K. Daniels, J. Dijksman, K. Huang, D. Parker, M. Schröter, R. Stannarius, and A. Wierschem, *Focus on Imaging Methods in Granular Physics*, Review of Scientific Instruments **88**, 051701 (2017).

[2] A. Autricque, N. Fedorczak, S. Khrapak, L. Couedel, B. Klumov, C. Arnas, N. Ning, J.-M. Layet, and C. Grisolia, *Magnetized electron emission from a small spherical dust grain in fusion related plasmas*, Physics of Plasmas **24**, 124502 (2017).

[3] S. W. Basuki, F. Yang, E. Gill, K. Rätzke, A. Meyer, and F. Faupel, *Atomic dynamics in Zr-based glass forming alloys near the liquidus temperature*, Physical Review B **95**, 024301 (2017).

[4] P. Born and K. Holldack, *Analysis of Granular Packing Structure by Scattering of THz Radiation*, Review of Scientific Instruments **88**, 051802 (2017).

[5] P. Born, J. Schmitz, and M. Sperl, *Dense fluidized granular media in microgravity*, npj Microgravity **3**, 27 (2017).

[6] H. Cárdenas, F. Frahsa, S. Fritschi, A. Nicolas, S. Papenkort, T. Voigtmann, and M. Fuchs, *Nonlinear response of supercooled melts under applied forces*, European Physical Journal – Special Topics **226**, 3039 (2017).

[7] C.-R. Du, V. Nosenko, H. Thomas, A. Müller, A. Lipaev, V. Molotkov, V. Fortov, and A. Ivlev, *Photophoretic force on microparticles in complex plasmas*, New Journal of Physics **19**, 073015 (2017).

[8] P. K. Galenko, D. A. Danilov, K. Reuther, D. V. Alexandrov, M. Rettenmayr, and D. M. Herlach, *Effect of convective flow on stable dendritic growth in rapid solidification of a binary alloy*, Journal of Crystal Growth **457**, 349 (2017).

[9] P. K. Galenko, R. Hanke, P. Paul, S. Koch, M. Rettenmayr, J. Gegner, D. M. Herlach, W. Dreier, and E. V. Kharanzhevski, *Solidification kinetics of a Cu-Zr alloy: ground-based and microgravity experiments*, IOP Conference Series: Materials Science and Engineering **192**, 012028 (2017).

[10] M. Gliozzi, I. Papadakis, D. Grupe, W. Brinkmann, and C. Räth, *Long-term monitoring of Ark 120 with Swift*, Monthly Notices of the Royal Astronomical Society **464**, 3955 (2017).

[11] S. Hakamada, A. Nakamura, M. Watanabe, and F. Kargl, *Surface Oscillation Phenomena of Aerodynamically Levitated Molten* Al_2O_3, International Journal of Microgravity Science and Application **34**, 340403 (2017).

[12] A. Haluszczynski, I. Laut, H. Modest, and C. Räth, *Linear and nonlinear market correlations: Characterizing financial crises and portfolio optimization*, Physical Review E **96**, 062315 (2017).

[13] D. M. Herlach, S. Burggraf, P. Galenko, C.-A. Gandin, A. Garcia-Escorial, H. Henein, C. Karrasch, A. Mullis, M. Rettenmayr, and J. Valloton, *Solidification of Undercooled Melts of Al-Based Alloys on Earth and in Space*, JOM: Journal of the Minerals, Metals and Materials Society **69**, 1303 (2017).

[14] J. Hoetzer, P. Steinmetz, A. Dennstedt, A. Genau, M. Kellner, I. Sargin, and B. Nestler, *Influence of growth velocity variations on the pattern formation during the directional solidification of ternary eutectic Al-Ag-Cu*, Acta Materialia **136**, 335 (2017).

[15] A. Ivlev and R. Kompaneets, *Instabilities in bilayer complex plasmas: Wake-induced mode coupling*, Physical Review E **95**, 053202 (2017).

[16] S. Jaiswal, T. Hall, S. LeBlanc, R. Mukherjee, and E. Thomas, *Effect of magnetic field on the phase transition in a dusty plasma*, Physics of Plasmas **24**, 113703 (2017).

[17] S. Khrapak, *Gruneisen parameter for strongly coupled Yukawa systems*, Physics of Plasmas **24**, 043706 (2017).

[18] S. Khrapak, *Practical dispersion relations for strongly coupled plasma fluids*, AIP Advances **7**, 125026 (2017).

[19] S. Khrapak, B. Klumov, and L. Couedel, *Collective modes in simple melts: Transition from soft spheres to the hard sphere limit*, Scientific Reports **7**, 7985 (2017).

[20] S. Khrapak, B. Klumov, and H. Thomas, *Fingerprints of different interaction mechanisms on the collective modes in complex (dusty) plasmas*, Physics of Plasmas **24**, 023702 (2017).

[21] R. Kobold, W. Kuang, H. Wang, W. Hornfeck, M. Kolbe, and D. Herlach, *Dendrite growth velocity in the undercooled melt of glass forming Ni50Zr50 compound*, Philosophical Magazine Letters **97**, 249 (2017).

[22] K. Kosiba, S. Scudino, R. Kobold, U. Kühn, A. Greer, J. Eckert, and S. Pauly, *Transient nucleation and microstructural design in flash-annealed bulk metallic glasses*, Acta Materialia **127**, 416 (2017).

[23] W. T. Kranz and M. Sperl, *Kinetic theory for strong uniform shear flow of granular media at high density*, EPJ Web of Conferences **140**, 03064 (2017).

[24] N. Kryuchkov, S. Khrapak, and S. Yurchenko, *Thermodynamics of two-dimensional Yukawa systems across coupling regimes*, Journal of Chemical Physics **146**, 134702 (2017).

[25] I. Laut, C. Räth, S. Zhdanov, V. Nosenko, G. E. Morfill, and H. M. Thomas, *Wake-mediated propulsion of an upstream particle in two-dimensional plasma crystals*, Physical Review Letters **118**, 075002 (2017).

[26] E. Lázaro-Lázaro, P. Mendoza-Méndez, L. F. Elizondo Aguilera, J. A. Perera-Burgos, P. E. Ramírez-González, G. Pérez-Ángel, R. Castañedo-Priego, and M. Medina-Noyola, *Self-consistent generalized Langevin equation theory of the dynamics of multicomponent atomic liquids*, Journal of Chemical Physics **146**, 184506 (2017).

[27] A. Liluashvili, J. Ónody, and T. Voigtmann, *Mode-coupling theory for active Brownian particles*, Physical Review E **96**, 062608 (2017).

[28] D. Matson, J. Rodriguez, J. Lee, R. W. Hyers, O. Shuleshova, I. Kaban, S. Schneider, C. Karrasch, S. Burggraf, R. Wunderlich, and H.-J. Fecht, *Use of Thermophysical Properties to Select and Control Convection During Rapid Solidification of Steel Alloys Using Electromagnetic Levitation on the Space Station*, JOM: Journal of the Minerals, Metals and Materials Society **69**, 1311 (2017).

[29] A. Meurisse, J. C. Beltzung, M. Kolbe, A. Cowley, and M. Sperl, *Influence of Mineral Composition on Sintering Lunar Regolith*, Journal of Aerospace Engineering **30**, 04017014 (2017).

[30] H. Meyer, T. Voigtmann, and T. Schilling, *On the non-stationary Generalized Langevin Equation*, Journal of Chemical Physics **147**, 214110 (2017).

[31] J. K. Meyer, I. Laut, S. K. Zhdanov, V. Nosenko, and H. M. Thomas, *Coupling of Noncrossing Wave Modes in a Two-Dimensional Plasma Crystal*, Physical Review Letters **119**, 255001 (2017).

[32] V. Nosenko, S. Zhdanov, H. Thomas, J. Carmona-Reyes, and T. W. Hyde, *Dynamics of spinning particle pairs in a single-layer complex plasma crystal*, Physical Review E **96**, 011201 (2017).

[33] B. Nowak, D. Holland-Moritz, F. Yang, T. Voigtmann, Z. Evenson, T. Hansen, and A. Meyer, *Effect of component substitution on the atomic dynamics in glass-forming binary metallic melts*, Physical Review B **96**, 054201 (2017).

[34] B. Nowak, D. Holland-Moritz, F. Yang, T. Voigtmann, T. Kordel, T. Hansen, and A. Meyer, *Partial structure factors reveal atomic dynamics in metallic alloy melts*, Physical Review Materials **1**, 025603 (2017).

[35] Y. Ohishi, F. Kargl, F. Nakamori, H. Muta, K. Kurosaki, and S. Yamanaka, *Physical properties of core-concrete systems: Al_2O_3-ZrO_2 molten materials measured by aerodynamic levitation*, Journal of Nuclear Materials **487**, 121 (2017).

[36] A. Orth, S. Steinbach, A. Dennstedt, and L. Ratke, *Aerogel-filled metals: a syntactic cellular material*, Materials Science and Technology **33**, 299 (2017).

[37] H. L. Peng, D. Herlach, and T. Voigtmann, *Crystal growth in fluid flow: Nonlinear response effects*, Physical Review Materials **1**, 030401 (2017).

[38] M. Y. Pustylnik, I. L. Semenov, E. Zaehringer, and H. M. Thomas, *Capacitively coupled rf discharge with a large amount of microparticles: Spatiotemporal emission pattern and microparticle arrangement*, Physical Review E **96**, 033203 (2017).

[39] J. E. Rodriguez, C. Kreischer, T. Volkmann, and D. M. Matson, *Solidification velocity of undercooled Fe–Co alloys*, Acta Materialia **122**, 431 (2017).

[40] T. Schilling and T. Voigtmann, *Clearing out a maze: A model of chemotactic motion in porous media*, Journal of Chemical Physics **147**, 214905 (2017).

[41] M. Schwabe, S. Zhdanov, T. C. Hagl, P. Huber, A. Lipaev, V. Molotkov, V. Naumkin, M. Rubin-Zuzic, P. Vinogradov, E. Zähringer, V. Fortov, and H. M. Thomas, *Observation of metallic sphere–complex plasma interactions in microgravity*, New Journal of Physics **19**, 103019 (2017).

[42] M. Schwabe, S. Zhdanov, and C. Räth, *Instability onset and scaling laws of an auto-oscillating turbulent flow in a complex plasma*, Physical Review E **95**, 041201(R) (2017).

[43] M. Schwabe, S. Zhdanov, and C. Räth, *Turbulence in an autooscillating complex plasma*, IEEE Transactions on Plasma Science **PP (99)**, 1 (2017).

[44] I. Semenov, *Moment fluid equations for ions in weakly ionized plasma*, Physical Review E **95**, 043208 (2017).

[45] I. Semenov, S. Khrapak, and H. Thomas, *Momentum transfer cross-section for ion scattering on dust particles*, Physics of Plasmas **24**, 033710 (2017).

[46] M. Sperl and A. Zippelius, *Driven Granular Fluids*, European Physical Journal – Special Topics **226**, 3079 (2017).

[47] J. Valloton, D. M. Herlach, H. Henein, and D. Sediako, *Microstructural Quantification of Rapidly Solidified Undercooled D2 Tool Steel*, Metallurgical and Materials Transactions A **48**, 4735 (2017).

[48] P. Vega-Martinez, J. Rodriguez-Roriguez, D. van der Meer, and M. Sperl, *Drop tower setup to study the diffusion-driven growth of a foam ball in supersaturated liquids in microgravity conditions*, Microgravity Science and Technology **29**, 297 (2017).

[49] J. J. Wessing and J. Brillo, *Density, Molar Volume, and Surface Tension of Liquid Al-Ti*, Metallurgical and Materials Transactions A **48**, 868 (2017).

[50] R. Wunderlich, H. J. Fecht, and G. Lohöfer, *Surface tension and viscosity of the Ni-based superalloys LEK94 and CMSX-10 measured by the Oscillating Drop Method on board a parabolic flight*, Metallurgical and Materials Transactions B **48**, 237 (2017).

[51] F. Yang, K.-U. Hess, T. Unruh, E. Mamontov, D. Dingwell, and A. Meyer, *Intrinsic proton dynamics in hydrous silicate melts as seen by quasielastic neutron scattering at elevated temperature and pressure*, Chemical Geology **461**, 152 (2017).

[52] L. Yang, M. Schwabe, S. Zhdanov, H. M. Thomas, A. Lipaev, V. Molotkov, V. Fortov, J. Zhang, and C. Du, *Density waves at the interface of a binary complex plasma*, EPL **117**, 25001 (2017).

2.2 Books and Book Chapters

[1] A. A. Bogno, J. Valloton, H. Henein, M. Gallerneault, and D. Herlach, *Effect of Hypoeutectic Sc Additions to Al-4.5 wt% Cu Under Different Cooling Rates*, in *Proceedings of the 3rd Pan American Materials Congress*, edited by M. A. Meyers et al. (2017), The Minerals Metals & Materials Series, pp. 355–363.

[2] D. J. Browne, F. Garcia-Moreno, H. Nguyen-Thi, G. Zimmermann, F. Kargl, R. H. Mathiesen, A. Griesche, and O. Minster, *Overview of In Situ X-Ray Studies of Light Alloy Solidification in Microgravity*, in *Magnesium Technology 2017*, edited by K. N. Solanki (2017), The Minerals Metals & Materials Series, pp. 581–590.

[3] L. Hennet, D. Holland-Moritz, R. Weber, and A. Meyer, *High-Temperature Levitated Materials*, in *Neutron Scattering – Applications in Biology, Chemistry, and Materials Science*, edited by F. Fernandez-Alonso and D. L. Price (Academic Press, 2017), vol. 49 of *Experimental Methods in Physical Sciences*, pp. 583–636.

2.3 Other Publications

[1] J. Schmitz, *Deutschland forscht auf der ISS – eine Bilanz (Teil 3), EML (Elektromagnetischer Levitator)*, Raumfahrt Concret **100**, 37 (2017).

3 Presentations

3.1 Institute Seminar

Speakers that have contributed to the institute's seminar in 2017.

Dr. Barbara Terheiden, Universität Konstanz, Germany (Jan 31, 2017): Contacting silicon solar cells with aluminium: Void formation in local contacts

Prof. Thomas Weinhardt, Twente University, Enschede, The Netherlands (Feb 7, 2017): Multi-Scale Modelling of Granular Media

Dr. Beata Tyburska-Püschel, DLR-MP (Feb 9, 2017): The response of fusion and fission materials to neutron irradiation

Dr. Ulrich Kueppers, Ludwig-Maximilians-Universität München (Feb 14, 2017): Physics of Volcanoes

Dr. Jazmin Duarte, Max-Planck-Institut für Eisenforschung, Düsseldorf (Feb 21, 2017): Crystallization in Fe-based amorphous alloys: High resolution characterization and in-situ observations

Prof. Clemens Bechinger, Universität Stuttgart, Germany (Mar 9, 2017): Active Particles in Microgravity

Prof. Thomas Palberg, Universität Mainz, Germany (Mar 14, 2017): A transient amorphous solid formed from low density aqueous charged sphere

Dr. Eloi Pineda, UPC BarcelonaTech, Spain (Apr 25, 2017): Mechanical relaxation of metallic glasses: an overview of experimental results and theoretical models

Dr. Jonathan Kollmer, North Carolina State University, Rayleigh, USA (May 5, 2017): An experimental investigation of the force network ensemble

Benedikt Nowak, DLR-MP (May 16, 2017): On the relationship between structure and atomic dynamics in glass-forming metallic melts

Dr. Clemens Prescher, Institute for Geology, Universität zu Kön, Germany (May 23, 2017): The density of the liquid earth

Dr. Torben Daeneke, RMIT University, Melbourne, Australia (May 29, 2017): Large area 2D nano materials synthesis utilizing ambient temperature liquid metals

Prof. Iciar Gonzales, Instituto de Acustica, Consejo Superior de Investigaciones Cientificas (CSIC), Madrid, Spain (Jun 6, 2017): Ultrasounds for Sensors and Actuators

Maike Becker, DLR-MP (Jun 13, 2017): X-Ray Investigations on Metallic Melts

Sebastian Pitikaris, DLR-MP (Jun 20, 2017): Local Elasic Properties in Granular Matter

Dr. Andriy Yakimovich, Institute for Functional Materials, Vienna, Austria (Jul 4, 2017): Nanocomposite Sn-based Alloys: Thermophysical and Thermodynamic Properties of the Liquid

Dr. Philip Born, DLR-MP (Jul 5, 2017): Shining Light on Granular Media II

Dr. Andrea Quaini, CEA Saclay, France (Jul 11, 2017): A versatile experimental setup for high temperature investigation of nuclear materials

Dr. Troy Shinbrot, Rutgers University, USA (Jul 14, 2017): Against the current: three examples of paradoxial flows

Prof. Magdaleno Medina-Noyola, University of San Luis Potosí, Mexico (Jul 31, 2017): The Self-Consistent Langevin Equation approach to non-equilibrium dynamics of liquids and glasses

Dr. Suvendu Mandal, Universität Innsbruck, Austria (Aug 23, 2017): The dynamics of driven and active Brownian particles

Prof. Thomas Weinhart, Twente University, Enschede, The Netherlands (Aug 29, 2017): Multi-Scale Modelling of Granular Media

Dr. Matthew Krzystyniak, Rutherford Appleton Laboratory, UK (Sep 7, 2017): Mass-Selective Neutron Scattering

Dr. Philip Born, DLR-MP (Oct 26, 2017): Chargeing Mechanismus for Granular Particles

Dr. Roman Kompaneets, DLR-CP (Nov 7, 2017): Complex plasmas from a theoretician's perspective

Dr. Till Kranz, DLR-MP (Nov 21, 2017): Rheology og Granular Fluids: An Integration Through Transients Approach

Prof. Hiroaki Katsuragi, Nagoya University, Japan (Nov 29, 2017): Solid projectile impact onto a porous dust aggregate consisting of micrometer-sized particles

Dr. Stefan Scharring, DLR Institute of Technical Physics, Stuttgart (Dec 12,2017): Laser-based Removal of Small-Sized Space Debris

Seminar talks in Oberpfaffenhofen:

Dr. Rene Sedlak, DLR-EOC (Jan 12, 2017): High resolution observations of small scale gravity waves and turbulence features in the OH airglow layer

Prof. Jochen Schein, Universität der Bundeswehr Neubieberg (Feb 2, 2017): Antriebe fr Satelliten auf der Basis von Vakuumbögen

Prof. Matthias Sperl, DLR-MP (Mar 23, 2017): Granulare Medien mit und ohne Ladung

Patrick Fopp, DLR-MP (Mar 30, 2017): Aerodynamic-Electrostatic Hybrid Levitation at 20 bar: Welcome to HÆL

Sonia Gamba, Swiss Plasma Center, École Polytechnique Fédérale de Lausanne (Apr 6, 2017): Linear Instabilities in a Drift-Kinetic Model for the Scrape-Off Layer

Prof. Roberto Piazza, Politecnico di Milano (May 11, 2017): Thermal forces: Moving and manipulating matter with thermal gradients

Francesca Luoni, Politecnico di Milano, Italy (Jul 27, 2017): Positron annihilation lifetime spectroscopy in mesoporous AEROGEL $150\,\mathrm{mg/cm^3}$

Dr. Masato Adachi, DLR-MP (Sep 14, 2017): Dynamics of Electromagnetic Particles and Its Applications for Mitigation and Utilization Technologies of Regolith on Moon, Mars, and Asteroids

Dr. Shota Nunomura, National Institute of Advanced Industrial Science and Technology, Research Center for Photovoltaic Technologies, Tsukuba, Japan (Sep 19 2017): State of arthigh-efficiency siliconsolar cells based onplasma processing technology

Prof. Sergey Popel, Space Research Institute RAS, Moscow, Russia (Oct 19, 2017): Dust on the Moon

Dr. Philip Born, DLR-MP (Oct 26, 2017): Charge and Light in Granular Matter

Dr. Michael Himpel, Greifswald University (Dec 7, 2017): High-density 3D particle tracking using 4 cameras

3.2 Talks given by institute members

Invited talks of institute members given at international conferences, symposia, and seminars.

Dendrite Growth Kinetics and Solutal Field Evolution Investigated by In-Situ X-ray Radiography of Thin Al-Ge Alloy Samples
M. Becker; 6th Decennial International Conference on Solidification Processing (SP17), Old Windsor, UK, July 2017.

Present knowledge on light scattering diagnostics and fluidization of granular samples in µg
P. Born; SoMaDy Workshop, FAU Erlangen, Germany, September 2017.

Electrostatic levitation of metallic samples under microgravity
D. Bräuer; International Symposium on Physical Sciences in Space (ISPS-7), Antibes, France, October 2017.

Fluidity model for non-Newtonian glass forming liquids
H. Cárdenas; Annual European Rheology Congress, Copenhagen, Denmark, April 2017.

Flowability of Lunar Regolith Simulant
M. Fateri; European Planetary Science Congress, Riga, Latvia, September 207.

Solar Sintering for Additive Manufacturing on the Moon
M. Fateri; European Planetary Science Congress, Riga, Latvia, September 207.

The structure-dynamics relationship in binary glass-forming alloy melts
D. Holland-Moritz; Keynote lecture, The 16th International Conference on Rapidly Quenched & Metastable Materials (RQ-16), Leoben, Austria, September 2017.

Precursor solitons in a flowing complex plasma
S. Jaiswal; 1st Asia-Pacific Conference on Plasma Physics (AAPPS-DPP 2017), Chengdu, China, September 2017.

Diffusion in Liquid Metals and Alloys
F. Kargl; invited talk, DPG Spring Meeting 2017, Bremen, Germany, March 2017.

Materials Physics in space at German Aerospace Center (DLR)
F. Kargl; CEA Sáclay, France, October 2017.

Materials Science Research at the Extreme
F. Kargl; Osaka University, Japan, November 2017.

A Model of Particle Charging in a Flowing Collisional Plasma
S. Khrapak; PK-4 Facility Science Team Meeting, Oberpfaffenhofen, Germany, December 2017.

Collective modes in Strongly Coupled Complex Plasmas and Related Systems
S. Khrapak; 8th International Conference on the Physics of Dusty Plasmas, Prague, Czech Republic, May 2017.

Plasma Parameter Control for Complex Plasma Experiments
C. A. Knapek; DPG Spring Meeting 2017, Bremen, Germany, March 2017.

Ekoplasma - Experiments with Grid Electrodes in Microgravity
C. A. Knapek; 8th International Conference on the Physics of Dusty Plasmas (ICPDP), Prague, Czech Republic, May 2017.

Microstructure of tetragonal Ni_2B compound solidified from the undercooled melt
M. Kolbe; 6th Decennial International Conference on Solidification Processing (SP-17), Old Windsor, United Kingdom, July 2017.

Effective Dynamics of Microorganisms Interacting with their own Trail
T. Kranz; Institut für Theoretische Physik, Universitt Göttingen, January 2017.

Flow Curves for Granular Matter at Finite Density and Shear Rate
T. Kranz; Workshop Bridging the Scales in Glasses III, Mainz, Germany, February 2017.

Flow Curves for Granular Matter at Finite Density and Shear Rate
T. Kranz; DPG Spring Meeting, Dresden, Germany, March 2017.

Transformation kinetics of metastable bcc-phase in undercooled Fe-Co alloy melts
C. Kreischer; 6th Decennial International Conference on Solidification Processing (SP17), Old Windsor, UK, July 2017.

Wake-mediated propulsion of an extra particle in a two-dimensional plasma crystal
I. Laut; International Conference on the Physics of Dusty Plasmas, Prague, Czech Republic, May 2017.

Self-propelled motion of an extra particle in a two-dimensional plasma crystal
I. Laut; DPG Spring Meeting, Dresden, Germany, March 2017.

Influence of electromagnetic levitation on measuring viscosities of liquid metals by the oscillation drop method
G. Lohöfer; European Conference on Thermophysical Properties (ECTP-21), Graz, Austria, September 2017.

Inductive measurement of electrical resistivity and thermal expansion of liquid $Zr_{64}Ni_{36}$ alloy
G. Lohöfer; European Conference on Thermophysical Properties (ECTP-21), Graz, Austria, September 2017.

Inductive measurement of electrical resistivity and thermal expansion of liquid metals in μg e.m. levitation
G. Lohöfer; International Symposium on Physical Sciences in Space (ISPS-7), Antibes, France, October 2017.

Materials Physics: The Benefit of Experiments in Weightlessness
A. Mëyer; Technische Universität München und Ludwig-Maximilans-Universität, Kolloquium der Münchner Physiker, Germany, January 2017.

Research without Up and Down – The Benefit of Experiments in Weightlessness
A. Mëyer; University of Oxford, St. Peter's College, GB, February 2017.

Structural Transition upon Vitrification in Viscous Metallic Liquids
A. Mëyer; DPG-Frühjahrstagung 2017, Dresden, Germany, March 2017.

Research without Up and Down – The Benefit of Experiments in Weightlessness
A. Mëyer; Universität Göttingen, Germany, June 2017.

Structural Transition upon Vitrification in Viscous Metallic Liquids
A. Mëyer; 8th International Conference on Relaxation in Complex Systems, Wisła, Poland, July 2017.

Forschen ohne oben und unten – Der Nutzen von Experimenten in Schwerelosigkeit für die Materialphysik
A. Mëyer; DLR Bonn Oberkassel, Germany, October 2017.

Mode Coupling in Large 2D Complex Plasma Crystals
J. Meyer; International Conference on the Physics of Dusty Plasmas (ICPDP), Prague, Czech Republic , May 2017.

Coupling of non-crossing wave modes in a two-dimensional plasma crystal
J. Meyer; 59th Annual Meeting of the APS Division of Plasma Physics, Milwaukee, Wisconsin, USA, October 2017.

Nonlinear time series analysis of atmospheric gravity waves
H. Modest; Conference on Statistical Physics Sigma Phi 2017, Korfu, Greece, July 2017.

Pairing of particles in two-dimensional complex plasma crystals
V. Nosenko; 8th International Conference on the Physics of Dusty Plasmas, Prague, Czech Republic, May 2017.

Influence of the chemical short-range order on the dynamics in binary glass-forming melts
B. Nowak; DPG-Frühjahrstagung 2017, Dresden, Germany, March 2017.

How chemical order and packing density influence the atomic dynamics in binary/ternary glass-forming metallic melts
B. Nowak; 24th International Symposium on Metastable, Amorphous and Nanostructured Materials (ISMANAM 2017), Donostia-San Sebastian, Spain, June 2017.

Recent results from the Plasmakristall-4 (PK-4) microgravity complex plasma laboratory
M.Y. Pustylnik; 8-th International Conference on Physics in Dusty Plasmas, Prague, Czech Republic, May 2017.

PK-4 experiment on board the ISS
M.Y. Pustylnik; International Symposium on Physical Sciences in Space (ISPS-7), Antibes, France, October 2017.

Status of the PK-4 project
M.Y. Pustylnik; ESA PK-4 Facility Science Team meeting, Oberpfaffenhofen, Germany, December 2017.

Synchronization in systems with linear, yet nonreciprocal interactions
C. Räth; SigmaPhi2017, Corfu, Greece, July 2017.

Single Particle Dynamics in a Radio-Frequency Produced Plasma Sheath
M. Rubin-Zuzic ; 8th International Conference on the Physics of Dusty Plasmas, Prague, Czech Republic, May 2017.

Single Particle Dynamics in a Radio-Frequency Produced Plasma Sheath
M. Rubin-Zuzic; PIIM-DLR Meeting on "Complex Plasma Crystals and Fluids: Dynamics and Thermodynamics", Marseille, France, December 2017.

3d structure of complex plasma obtained from PK-4 scans
M. Rubin-Zuzic; PK-4 FST Meeting, Oberpfaffenhofen, Germany, December 2017.

Wake-mediated propulsion of an extra particle in a two-dimensional plasma crystal
I. Semenov; 8th International Conference on the Physics of Dusty Plasmas (ICPDP-8), Prague, Czech Republic, May 2017.

Installation and Operation of the Electromagnetic Levitator EML on ISS and Experiment Preparation
S. Schneider; International Symposium on Physical Sciences in Space (ISPS-7), Antibes, France, October 2017.

Onset of turbulence in an autooscillating complex plasma
M. Schwabe; International Conference on the Physics of Dusty Plasmas (ICPDP), Prague, Czech Republic, May 2017.

Latest Results on Complex Plasmas with the PK-3 Plus Laboratory on board the International Space Station
M. Schwabe; International Symposium on Physical Sciences in Space (ISPS-7), Antibes, France, October 2017.

Rheology and Microrheology in Driven Granular Media
M. Sperl; Internationaler Glastag Konstanz, Germany, April 2017.

Granular Experiments in Microgravity
M. Sperl; Soft Matter research group, Lucasian Chair, Cambridge University, UK, May 2017.

Dune Formation and Migration in a Laboratory Windtunnel
M. Sperl; Department of Applied Mathematics and Theoretical Physics, Cambridge University, UK, May 2017.

Sintering and Shaping Lunar Regolith by Solar Light
M. Sperl; 5th European Lunar Symposium, Münster, Germany, May 2017.

Rheology in Particulate Systems
M. Sperl; Bubble and Drop 2017, Lyon, France, June 2017.

Dynamics of Granular Matter in Microgravity
M. Sperl; Physics Department, Technical University of Munich, Germany, July 2017.

Dense Granular Rheology from First Principles
M. Sperl; V International Conference on Particle-Based Methods (PARTICLES 2017), Hannover, Germany, September 2017.

Investigation of the effect of fluid flow on microstructure evolution in Al-Si-Fe alloys: The MICAST project
S. Steinbach; Invited lecture, 6th Decennial International Conference on Solidification Processing (SP17), Old Windsor, UK, July 2017.

The influence of Intermetallic Phases on the Permeability in Al-Si-Cu-Fe Alloys Processed under Forced Fluid Flow Conditions
S. Steinbach; 6th Decennial International Conference on Solidification Processing (SP17), Old Windsor, UK, July 2017.

Gravity impact on microstructure evolution in technical alloys during Solidification Processes
S. Steinbach; CSU-ESA Cooperation in Manned Space Science and Utilization, Beijing, China, June 2017.

Past, Present and Future of Complex/Dusty Plasma research under microgravity conditions
H. Thomas; keynote lecture, 8th International Conference on the Physics of Dusty Plasmas (ICPDP-8), Prague, Czech Republic, May 2017.

Ekoplasma – The Future of Complex Plasma Research in Space
H. Thomas; International Symposium on Physical Sciences in Space (ISPS-7), Antibes, France, October 2017.

History-Dependent Material Properties
Th. Voigtmann; Colloquium of the International Graduate School Soft Matter Sciences, Freiburg, Germany, January 2017.

Nonlinear Resposne in Crystallization
Th. Voigtmann; International Workshop of the COST Action Flowing Matter, Erlangen, Germany, February 2017.

Crystal Growth in Fluid Flow
Th. Voigtmann; Annual European Rheology Congress, Copenhagen, Denmark, April 2017.

Slow Dynamics of Active Brownian Particles
Th. Voigtmann; Physics Colloquium, University of Greifswald, Germany, April 2017.

Slow Dynamics of Active Brownian Particles
Th. Voigtmann; Minisymposium on Amorphous Solids and Viscoelasticity, Strasbourg, France, June 2017.

Sampling Chess
Th. Voigtmann; Big Tech Day, TNG Consulting, Munich, Germany, June 2017.

Slow Dynamics of Active Brownian Particles
Th. Voigtmann; 8th International Conference on Relaxation in Complex Systems, Wisła, Poland, July 2017.

On the Importance of Pawns in Chess
Th. Voigtmann; Physics Colloquium, University of Leipzig, Germany, December 2017.

Dendrite growth kinetics and growth morphology of fcc and bcc structured phases in undercooled melts
T. Volkmann; 6th Decennial International Conference on Solidification Processing (SP 17), Old Windsor, United Kingdom, July 2017.

Metastable phase formation in undercooled Nd-Fe-B alloy melts
T. Volkmann; International Symposium on Physical Sciences in Space (ISPS-7), Antibes, France, October 2017.

Fine structure of a Mach cone in a zero gravity, 3d complex plasma system
E. Zähringer; DPG Spring Meeting 2017, Bremen, Germany, March 2017.

Relation between self-diffusion and viscosity in $Ni_{66.7}B_{33.3}$
S. Zimmermann; 16th International Conference on Rapidly Quenched and Metastable Materials (RQ16), Leoben, Austria, August 2017.

3.3 Doktorandenrunde

Doktorandentag in Köln-Porz, May 18, 2017:

Jan Haeberle, DLR-MP: Tribocharging of surface treated granular media

Alexandre Meurisse, DLR-MP: Solar 3D printing of lunar regolith

Koray Önder, DLR-MP: Exact Solution of the spin model on the Bethe lattice

Carolina Kreischer, DLR-MP: Electromagnetic levitation and the investigation of FeCo alloys

Dandan Zhao, DLR-MP: Solidification in Ti-Y alloys under electrostatic levitation

Sandro Szabo, DLR-MP: Self-diffusion of Ge in AlGe, investigated with quasi-elastic neutron scattering

Nannan Zhang, DLR-MP: Influence of fluid flow and iron intermetallic phases on the microstructure of directionally solidified Al-Si- Cu-Fe alloys

Mareike Wegener, DLR-MP: Morphological transition in Al based alloys observed with in-situ X-ray radiography

Ingo Laut, DLR-CP: Wake-mediated effects in two-dimensional complex plasmas

Erich Zähringer, DLR-CP: Supersonic Particle in a Low Damped Complex Plasma under Microgravity

Alexander Böbel, DLR-CP: Morphological Data Analysis in Complex Plasmas

Meike Müller, DLR-CP: Decontamination of Space Equipment Using Cold Atmospheric Plasma

Doktorandentag in Oberpfaffenhofen, December 13/14, 2017:

Olfa Lopez, DLR-MP: Powder-basedAdditive Manufacturing in microgravity

Kasten Tell, DLR-MP: Granular Sound Measurements in Microgravity

Tina Gläsel, DLR-MP: Liquid-Solid Interfaces at High Temperatures

Jonathan Ónody, DLR-MP: Dense Microswimmer Systems in Model Porous Media

Julian Reichert, DLR-MP: Mode-Coupling Theory of Active Particles: Anisotropic and Sheared Systems

Patrick Fopp, DLR-MP: What the HÆL. . .

Ming Wei, DLR-MP: Solidification process of aluminum alloys: Phase-field study

Sandro Szabo, DLR-MP: Back to the 1960’s with the most toxic non-radioactive Element

4 Lecture Courses and Lectures

Thermophysikalische Eigenschaften der Schmelzen
RWTH Aachen, 2 SWS (WS 2016/17)
J. Brillo

Einführung in die Metallphysik
Ruhr-Universität Bochum, 2 SWS (WS 2016/17)
D. Holland-Moritz

Heterogene Gleichgewichte
RWTH Aachen, 2 SWS (WS 2016/17)
F. Kargl

Oberseminar Materialphysik im Weltraum
Ruhr-Universität Bochum, 2 SWS (WS 2016/17, WS 2017/18)
A. Meyer

Complex Systems and Fundamentals of Nonlinear Data Analysis
LMU München, 6 SWS (WS 2016/17)
Ch. Räth

Advanced Statistical Physics
Universität zu Köln, 4+2 SWS (WS 2016/17)
M. Sperl, W. T. Kranz

Theoretical Biophysics
Heinrich-Heine-Universität Düsseldorf, 4 SWS (WS 2016/17)
Th. Voigtmann

Einführung in die Röntgen- und Neutronenstreuung
Ruhr-Universität Bochum, 2 SWS (SS 2017)
D. Holland-Moritz

Introduction to Statistical Optics
Universität zu Köln, 2 SWS (SS 2017)
M. Sperl, P. Born

Physics of Granular Solids
DLR Köln, 2 SWS (P. Born)

Messmethoden in der Physik
Ruhr-Universität Bochum, 2 SWS (WS 2017/18)
D. Holland-Moritz

Heterogene Gleichgewichte
RWTH Aachen, 2 SWS (WS 2017/18)
F. Kargl

Statistical Mechanics of Disordered Systems
Heinrich-Heine-Universität Düsseldorf, 4 SWS (WS 2017/18)
Th. Voigtmann, J. Ónody

5 Graduations

Bachelor

- Janek Möller, *Entwicklung eines Prüf- und Messstandes fr die Kalibrierung optischer Systeme*, Hochschule für angewandte Wissenschaften München, March 2017 (supervisor J. Prell)
- Marc Geisthoff, *Improvement of a Granular Material Experiment under Microgravity using X-Rays*, FH Aachen, June 2017 (supervisor M. Sperl).
- Sebastian Wiese, *Morphologischer Dendriten-Übergang von Al-Ge Legierungen*, RWTH Aachen, August 2017 (supervisor F. Kargl).
- Stephanie Oppelt, *Messung der triboelektrischen und tribologischen Eigenschaften oberflächenbehandelter granularer Medien*, Hochschule Bonn-Rhein-Sieg, September 2017 (supervisor P. Born).

Diploma and Master

- Caspar Reinerth, *Concentration dependence of interdiffusion coefficient in liquid metals*, Universität Münster, January 2017 (supervisor A. Meyer).
- Rogerio Borges Ferreira, *Construction of a gas-powered fluidized bed for a parabolic flight campaign under reduced gravity*, FH Aachen, April 2017 (supervisor M. Sperl).
- Raphael Keßler, *Entwicklung eines raumflugfähigen Mikroschwimmermoduls zur Untersuchung des dreidimensionalen Phasenverhaltens selbstphoretischer Teilchen unter Schwerelosigkeit*, Universität Cottubs, July 2017 (supervisor Th. Voigtmann).
- Marcus Reinartz, *Examination of Morphological Transitions in the Al-Zn System using In-situ Real-time X-radiography*, Universität zu Köln, September 2017 (supervisor F. Kargl).
- Jeremy Reguette, *Investigaton on Layer-wise Deposition and Sintering of Lunar Simulant*, EEIGM, September 2017 (supervisor M. Sperl/M. Fateri).
- Celine Bernillon, *Flowability study of lunar regolith simulant*, EEIGM, September 2017 (supervisor M. Sperl/M. Fateri).
- Manel Vera Palou, *Solvent Cast 3D Printing for space Applications*, EEIGM, September 2017 (supervisor M. Sperl/M. Fateri).

- Fernando Gobartt, *Solvent Cast 3D printing of sustainable cellulosic-based composites for space application*, EEIGM, September 2017 (supervisor M. Sperl/M. Fateri).
- Oriane Garcia, *Microwave post-treatment using lunar simulant*, EEIGM, September 2017 (supervisor M. Sperl/M. Fateri).
- Miguel Álvarez Hausmann, *Study and characterisation of a new lunar regolith simulant-EAC-1*, EEIGM, September 2017 (supervisor M. Sperl/M. Fateri).

PhD Theses

- Isabell Jonas, *Thermophysical and structural properties of the equilibrium and undercooled melt of bulk metallic glasses investigated by electrostatic levitation*, Universität des Saarlandes, June 2017 (supervisor A. Meyer).
- Sebastian Pitikaris, *Local Mechanical Properties of Granular Media*, Universität zu Kön, June 2017 (supervisor M. Sperl).
- Maike Becker, *Solidification kinetics in Al-Cu and Al-Ge alloys investigated by in-situ X-ray radiography*, RWTH Aachen, September 2017 (supervisor F. Kargl).
- Ingo Laut, *Nonreciprocity and nonlinearity: Applications in complex plasmas and time series*, LMU München, November 2017 (supervisor G. Morfill/Ch. Räth)
- Christian Neumann, *Entwicklung eines elektrostatischen Levitators für den Einsatz in Mikrogravitation*, Universität des Saarlandes, December 2017 (supervisor A. Meyer).
- Alexander Liluashvili, *Mode-Coupling Theory of Active Brownian Particles*, Universität Düsseldorf, December 2017 (supervisor Th. Voigtmann).

Habilitation Theses

- Christoph Räth, *Decoding Complex Structures: Applications in Medical Physics, Plasma Physics and Astrophysics*, Ludwig-Maximilians-Universität München, November 2017.

6 Awards

- Jürgen Brillo, DLR Senior Scientist, June 2017

7 Fellows

Visiting fellows at the institute:

- Stefan Burggraf: Ruhr-Universität Bochum (2013–2018)
- Dr. Luis Fernando Elizondo-Aguilera: DLR-DAAD postdoctoral fellow (2015–2018)
- Janni Harju: DAAD internship (2017)
- Dr. Surabhi Jaiswal: DLR-DAAD postdoctoral fellow (2017–2018)
- Dr. Ali Kaouk: DLR-DAAD postdoctoral fellow (2016–2018)
- Toshiki Kondo: Osaka University, Japan (Jan/Feb 2017)
- Dr. Nishant Kumar: DLR-DAAD postdoctoral fellow (2016–2018)
- Alexandre Meurisse: DLR-DAAD PhD fellow (2015–2019)
- Dr. John Meyer: DLR-DAAD postdoctoral fellow (2016–2018)
- Dr. Ahmed Munawar: NUST, Pakistan (Jul 2017–Jan 2018)
- Syed Ali Raza Jafri: NUST, Pakistan (Aug/Sep 2017)
- Steven Parth: University of Alberta, Canada (May–Aug 2017)
- Ming Wei: Central Southern University, China (Oct 2017–Oct 2018)
- Nannan Zhang: DLR-DAAD PhD fellow (2017)
- Dandan Zhao: Northeastern University Shanghai (2016–2018)

8 Events and Campaigns

- International Space Station (ISS), PK-4 facility, February 2017: Campaign 4
- International Space Station (ISS), EML facility, February 2017: Commissioning of SCE (Sample Coupling Electronics).
- 30th DLR Parabolic Flight campaign, September 2017: TEMPUS experiment.
- International Space Station (ISS), EML facility, May 2017: Checkout Experiment (FCE-r) for Batch 2.
- International Space Station (ISS), EML Batch 2.1 experiments, June–July 2017.

- International Space Station (ISS), EML Batch 2.2 experiments, October–December 2017.
- Frequent measurement campaigns at Forschungsneutronenquelle Heinz-Maier-Leibnitz (FRM II), Garching, TU München: Neutron time-of-flight spectrometer ToF-ToF and neutron radiography beamline ANTARES.
- Frequent measurement campaigns at Institut Lauge-Langevin (ILL), Grenoble, France: High flux neutron diffractometer D20, neutron time-focussing time-of-flight spectrometer IN6, and small momentum transfer diffractometer D16.
- Frequent measurement campaigns at the European Synchrotron Radiation Facility (ESRF), Grenoble, France: Materials science beamline ID15.
- Measurement campaigns at Hasylab, DESY Hamburg: USAXS beamline BW4.

9 Workshops organized by the institute

European Space Science Committee (DLR-CP, 22–24 November 2017)

The European Space Sciences Committee (ESSC) is an independent committee under the European Science Foundation (ESF), as a means to give European space scientists an independent voice in the space sciences arena. The ESSC scope covers the whole spectrum of space sciences, from microgravity research to space physics, and from planetary sciences to astronomy and Earth sciences. ESSC has a unique position in Europe providing independent scientific advice on space science matters to the European Space Agency (ESA), the European Commission (EC), national space agencies, and other stakeholders and has become the reference body in Europe on space sciences matters.

Prof. Pascale Ehrenfreund, Chair of the Executive Board, DLR: The German Aerospace Centre and space sciences in Germany

Dr. Luigi Colangeli, Head of the Coordination Office for the Scientific Programme, ESA: ESA Mandatory Scientific Programme Update

Dr. David Parker, Director of Human Spaceflight and Robotic Exploration, ESA: ESA Human Spaceflight and Robotic Exploration Update

Dr. Mats Ljungqvist, Policy Officer, DG GROWTH, European Commission: European Commission Programme and outlook on FP9

Dr. Michael Moloney, Director, Space Studies Board: US Space Studies Board update

Prof. Karl-Heinz Glassmeier, TU Braunschweig: COSPAR Update

Dr. Marco Berg, Head of the human spaceflight department, OHB: The Dream Chaser for European Utilisation (DC4EU)

Dr. Hilde Stenuit, ICE Cubes business development: Space Applications IceCube

Dr. Maurice Borgeaud, Head of the ESA Earth Observation Department "Science, Applications and Climate", ESA: ESA Earth Observation

PK-4 Meeting (DLR-CP, 18/19 December 2017)

PK-4 is the present laboratory for complex plasma research on the ISS. The international science team meets once a year to discuss status, recent results and future experiments.

M. Pustylnik, DLR-CP: Status of the PK-4 project

S. Khrapak, DLR-CP: Model of particle charging in flowing collisional plasma

T. Antonova, DLR-CP: Particle charge in PK-4: DC discharge from ground and microgravity experiments

T. Hyde, Baylor University, Waco, Texas, USA: Self-Ordering in field-aligned strings

S. Usachev, Joint Institute for High Temperatures, Moscow, Russia: Spectroscopic diagnostics of the PK-4 dusty plasma

E. Thomas, Auburn University, USA: Particle heating at the onset of polarity switching: preliminary results and proposed flight experiments I

J. Williams, Wittenberg University, USA: Particle heating at the onset of polarity switching: preliminary results and proposed flight experiments II

B. Liu, Iowa University, USA: Characterization of Nonlinear Waves

S. Jaiswal, DLR-CP: Effect of discharge polarity reversal on the wave propagation in flowing complex plasma under microgravity condition

M. Schwabe, DLR-CP: Waves in a String Fluid

M. Rubin-Zuzic, DLR-CP: 3D structure of complex plasma obtained from PK-4 scans

V. Nosenko, DLR-CP: Laser-driven shear flows in 3D complex plasmas

M. Pustylnik, DLR-CP: New experiment ideas from DLR

10 Third-Party Funding

European Space Agency (ESA) – AO 1999, selected flight experiments

Microstructure formation in casting of technical alloys under diffusive and magnetically controlled convective conditions (MICAST)
L. Ratke, coordinator; G. Müller (D);
Y. Fautrelle (F); M. D. Dupony (F); A. Roosz (HUN);
G. Zimmermann (D); J. Lacaze (F)
rated *excellent*

Metastable Solidification of Composites: Novel Peritectic Structures and In-Situ Composites (METCOMP)
M. Kolbe, coordinator; G. Eggeler (D);
L. Granaszy (HUN); **D. M. Herlach**; A. Ludwig (A);
M. Rappaz (CH)
rated *excellent*

High Precision Thermophysical Property Data of Liquid Metals for Modelling of Industrial Solidification Processes (THERMOLAB)
H. J. Fecht, coordinator (D); L. Battezzati (I); **J. Brillo**;
A. Passerone (I); E. Ricci (I); S. Seetharaman (S);
R. Aune (S); J. Etay (F)
rated *outstanding*

Study and modelling of nucleation and phase selection phenomena in undercooled melts: Application to hard magnetic alloys of industrial relevance (MAGNEPHASE)
W. Löser, coordinator (D); L. Granasy (HUN);
R. Hermann (D); **D. Holland-Moritz**; **T. Volkmann**;
J. Fransaer (B); rated *very good*

Solidification along a Eutectic Path in Ternary Alloys (SETA)
S. Rex, coordinator (D); L. Froyen (B); G. Faivre (F);
H. Nguyen-Thi (F); **L. Ratke**
rated *excellent*

Thermophysical Properties of Liquid Metals for Industrial Process Design (ThermoProp)
H.-J. Fecht, coordinator (D); R. Wunderlich (D);
L. Battezzati (I); **J. Brillo**; J. Etay (F); E. Ricci (I);
S. Seetharaman (S)
consolidation of ESA MAP project AO 1999, 2004, and 2009 – rated *outstanding*

European Space Agency (ESA) – AO 2000, selected flight experiments

Investigations of thermophysical properties of Si in the melt and in the undercooled state under microgravity conditions (SEMITHERM)
K. Samwer, coordinator (D): B. Damaschke (D);
J. Brillo; E. Ricci (I); E. Arato (I); T. Hibiya (JPN);
W. von Ammon (D); T. Tsukuda (JPN);
T. Fuhiwara (JPN)
rated *very good*

Magnetohydro-dynamics of levitated drops
R. Wunderlich, coordinator (D); G. Gerbeth (D);
I. Egry; J. Priede (LV); J. Etay (F); Y. Fautrelle (F)
rated *very good*

European Space Agency (ESA) – AO 2004, selected flight experiments

In-situ X-ray Monitoring of Advanced Metallurgical Processes under Microgravity and Terrestrial Conditions (XRMON)
R. H. Mathiesen, coordinator (N);
G. Zimmermann (D): H. Nguyen-Thi (F); L. Froyen (F);
M. Kolbe/F. Kargl; C.-A. Gandin (F);
D. Browne (IRL); F. García-Moreno (D)
rated *excellent*

Chill Cooling for the Electro-Magnetic Levitator in Relation with Continuous Casting of Steel (CCEMLCC)
C.-A. Gandin, coordinator (F); **D. M. Herlach**;
T. Volkmann; V. Uhlenwinkel, H. Henein,
D. Juul Jensen (DK); M. Kallio, F. Costes,
M. Bobadilla
rated *excellent*

Non-equilibrium multiphase transformations: eutectic solidification, spinoidal decomposition and glass formation (MAGNEPHASE)
P. Galenko, coordinator; **D. M. Herlach**;
R. Parfeniev (RUS); B. Melekh (RUS);
M. Volkov (RUS); A. Ivanov (RUS)
rated *excellent*

Electrical Resistivity measurements of high temperature metallic melts (RESISTIVITY)
G. Lohöfer, coordinator; G. Pottlacher (A)
rated *excellent*

European Space Agency (ESA) – AO 2009, selected flight experiments

Thermophysical properties of liquid metallic alloys – modelling of industrial solidification processes and development of advanced products (THERMOLAB – ISS)
H.-J. Fecht, coordinator (D); L. Battezzati (I);
J. Brillo; A. Dommann (CH); U. Erb (CDN);
J. Etay (F); H. Fukuyama (JPN); T. Hibiya (JPN);
R. Hyers (USA); T. Ishikawa (JPN); J. Z. Jiang (CHN);
K. Kelton (USA); G. W. Lee (ROK); W. Lojkowski (PL);
I. Manna (IND); D. Matson (USA); S. Ozawa (JPN);
K. Pericleous (UK); E. Ricci (I); S. Seetharaman (S);
T. Tanaka (JPN); R. Valiev (RUS); M. Watanabe (JPN);
R. Wunderlich (D)

rated *outstanding*

Thermophysical properties and solidification behaviour of undercooled Ti-Zr-Ni liquids showing an icosahedral short-range order (ICOPROSOL)
D. Holland-Moritz, coordinator; R. Hyers (USA); K. Kelton (USA); **G. Lohöfer**
rated *excellent*

Gravity dependence of CET in peritectic TiAl alloys (GRADECET)
U. Hecht, coordinator (D); D. Daloz (F); L. Gránásy (HUN); A. Griesche (D); J. Lapin (SK); S. McFadden (IRL); **A. Meyer**; M. Rebow (PL); L. Sturz (D); G. Tegze (HUN); M. Zaloznik (F)
rated *excellent*

Thermophysical properties of liquid alloys under oxygen influence (OXYTHERM)
J. Brillo, coordinator; E. Arato (I); H. Fritze (D); H. Fujii (JPN); L. Hennet (F); G. Kaptay (HUN); R. Novakovic (I); S. Ozawa (JPN); E. Ricci (I); M. Watanabe (JPN)
rated *excellent*

Peritectic alloy rapid solidification with electromagnetic convection (PARSEC)
T. Volkmann, coordinator; J. Fransaer (B); R. Hyers (USA); M. Krivilev (RUS); W. Löser (D); D. Matson (USA); K. Pericleous (UK)
rated *excellent*

Liquid phase separation in metallic alloys (LIPHASE)
M. Kolbe, coordinator; L. Battezzati (I); **J. Brillo**; D. Chatain (F); S. Curiotto (F); J. Gao (CHN); H. Yasuda (JPN)
rated *excellent*

Compaction and Sound Transmission in Dense Granular Media (COMPGRAN)
M. Sperl, coordinator; R. Behringer (USA); E. Clement (F); S. Luding (NL); M. Schroeter (D)
rated *excellent*

Influence of diffusive and convective mass transport on microstructure formation in Al-based alloys (DIFFSOL)
A. Griesche, coordinator (D); H. Emmrich (D); **J. Horbach**; G. Kaptay (HUN); **A. Meyer**; B. Nestler (D); H. Nguyen-Thi (F); Y. Fautrelle (F); X. Ruiz (E); Z. Saghir (CDN); V. M. Shevtsova (B); R. Siquieri (D); **T. Voigtmann**; G. Zimmermann (D)
rated *very good*

Non-equilibrium solidification, modelling for microstructure engineering of industrial alloys (NEQUISOL III)
D. M. Herlach, coordinator; U. Fritsching (D); C.-A. Gandin (F); H. Henein (CDN); V. Uhlenwinkel (D)
rated *very good*

Liquid phase diffusion in semiconductors (LIPIDIS)
S. Dost, coordinator (CDN); B. Lent (CDN); T. Masaki (JPN); **A. Meyer**; **F. Kargl**; B. Nestler (D); Z. Saghir (CDN); A. Senchenkov (RUS); H. Struchtrup (CDN); D. Vizman (ROM); A. Croll (D); E. Dieguez (E); T. Duffar (F); A. Egorov (RUS)
rated *very good*

Gravitational effects on heat and mass transport phenomena in directional solidification of upgraded metallurgical silicon for photovoltaic applications (SISSI)
T. Duffar, coordinator (F); J. Friedrich, coordinator (D); J. Baruchel (F); M. Bellmann (N): S. Binetti (I); T. Carlberg (S); A. Croll (D); J. Derby (USA); E. Dieguez (E); S. Dost (CDN); F. Dupret (B); H. Emmerich (D); A.-J. Faber (NL); C.-A. Gandin (F); J.-P. Garandet (F); M. Gonik (RUS); **A. Meyer**; **F. Kargl**; K. Kakimoto (JPN); N. Mangelinck (F); W. Miller (D); B. Nestler (D)
rated *outstanding*

Soft Matter Dynamics
M. Sperl (coordinator), D. Langevin (F); R. Hohler (F); R. Miller (D); L. Liggieri (IT)
rated *excellent*

European Space Agency (ESA) – Microgravity Application Programme

Soft Matter Dynamics
M. Sperl; *various partners*

European Space Agency (ESA) – General Support Technology Programme

3D printing of a model building block for a lunar base outer shell
M. Sperl; DLR Solar Research and Materials Research

European Space Agency (ESA) – General Studies Programme

Moon Energy Storage and Generation (MESG)
M. Sperl; *partners from industry*

European Space Agency (ESA) – Networking/Partnering Initiative

Physical Properties of Powder-Based 3D-Printing in Space and on Ground
M. Sperl

ESA Topical Teams

Atomic Transport in Liquids and Semiconductors (ATLAS)
A. Griesche, coordinator (D); **A. Meyer**; J.-P. Garandet (F); Z. Saghir (CDN); W. Miller (D); W. Wołczyński (PL); A. Mialdun, D. Melnikov, I. Ryzhkov, V. Shevtsova, S. Van Vaerenbergh (B); J. Agren (S); J. Friedrich (D); F. Faupel (D); H. Emmerich (D); B. Nestler (D); G. Wilde (D)

Solidification of Containerless Undercooled Melts SOL–EML
D. M. Herlach (coordinator), **P. Galenko, D. Holland-Moritz, M .Kolbe, T. Volkmann**; J. Fransaer (B); G. Phanikumar (IND); Ch.-A. Gandin (F); J. Gao, L. Granasy (HUN); H. Henein (CDN); R. W. Hyers (USA); K. F. Kelton (USA); W. Löser (D); D. M. Matson, T. Okutani (JPN): K. Pericleous (UK); M. P. Volkov (RUS); H. Yasuda (JPN)

Space Grains
E. Falcon, coordinator (F); S. Aumaître (F); R. Behringer (USA); M. Berhanu (F); E. Clément (F); J. Crassous (F); D. Durian (USA); P. Evesque (F); S. Fauve (F); A. Garcimartin (E); Y. Garrabos (F); M. Hou (CHN); X. Jia (F); C. Lecoutre (F); F. Ludewig (B); S. Luding (NL); S. Merminod (F); E. Opsomer (B); D. Ozcodi (E); M. Schroeter (D); **M. Sperl**; R. Stannarius (D); N. Vandewalle (B); **P. Yu**

Complex Plasmas in Microgravity
H. Thomas, coordinator, **T. Antonova**; L. Boufendi (F); L. Couedel (F); C.-R. Du (CI); A. Fedoseev (RUS); V. Fortov (RUS); G. Ganguli (USA); J. Goree (USA); P. Hartmann (HUN); T. Hyde (USA); **S. Khrapak**; U. Konopka (USA); M. Kretschmer (D); A. Lipaev (RUS); B. Liu (USA); A. Melzer (D); V. Molotkov (RUS); V. Naumkin (RUS); **V. Nosenko**; O. Petrov (RUS); **M. Pustylnik**; **Ch. Räth**; T. Ramazanov (KZ); S. Ratynskaia (SE); M. Rosenberg (USA); **M. Rubin-Zuzic**; **M. Schwabe**; A. Sen (IN); G. Sukhinin (RUS); K. Takahashi (JP); M. Thoma (D); E. Thomas (USA); P. Tolias (SE); A. Usachev (RUS); J. Williams (USA); A. Zobnin (RUS)

ESA User Support

MSL-LGF and MSL-SQF Experiment Preparation and Operations Support
S. Steinbach

Support of TEMPUS/EML Parabolic flight and TEXUS campaigns
S. Schneider

FRC Support for Columbus Multi User Facilities, USOC Implementation and Operations, EML
S. Schneider

FRC Support for Columbus Multi User Facilities, USOC Implementation and Operations, MSL
S. Steinbach

FRC Support for Columbus Multi User Facilities, USOC Implementation and Operations, TEMPUS 24
D. Heuskin

FRC Support for Columbus Multi User Facilities, USOC Implementation and Operations, TEMPUS 25
S. Klein

PK-4 Experiment Preparation
contract from CADMOS, **H. Thomas**

PK-4 Sustaining Engineering
sub-contract from OHB, **H. Thomas**

European Union

RegoLight – Sintering Regolith with Solar Light
M. Sperl; Space Application Services (B); Liquifier Systems Group (A); Comex S.A. (F); Bollinger (A) (2015–2017)

Bundesministerium für Bildung und Forschung (BMBF)

Verbundvorhaben Magnetische Aktormaterialien mit reduziertem Gallium-Anteil (MAREGA), Teilvorhaben Thermophysikalische Eigenschaften Magnetischer Ga-reduzierter Formgedächtnislegierungen
J. Brillo (2016–2019)

Verbundvorhaben Klimaschutz, Teilvorhaben 2: Direkteinspritzventilentwicklung (MULTDIRIN)
D. Neuhaus (2016–2017)

DLR Space Administration / BMWi

Continuation of Plasma Research at DLR
Projects PK-4 and Ekoplasma, **H. Thomas**

Bavarian Ministry of Economic Affairs

Continuation of Plasma Research at DLR
Projects Ekoplasma, Ground based labs, theory and simulation; **H. Thomas**

Plasma-Decontamination of Space Equipment
H. Thomas (PI); G. Morfill (D); **M. Müller**; P. Rettberg (DLR-ME); M. Thoma (D); J. Zimmermann (D)

Deutsche Forschungsgemeinschaft (DFG)

Electrostatic levitation investigation of the temperature rheological and volumetric changes of Molten Zr-based bulk metallic glass forming alloys
A. Meyer; R. Busch, Universität Saarbrücken (2012–2015; renewed 2015–2018)

Active microrheology of dense microswimmer suspensions
Th. Voigtmann (2014–2017, renewed 2017-2019)

Presshärten von Rohren durch granulare Medien
P. Born, M. Sperl; A. E.Tekkaya, Universität Dortmund (2014–2017)

11 Author Index

Page numbers in **bold face** indicate corresponding authors. Page numbers in *italic type* indicate coauthors. Authors affiliated with the institute appear in **bold face**.

T. Antonova, *5*
M. Balter, *2*
C. Bechinger, *3*
M. Becker, *22*, **23**
I.V. Belova, *14*
J. C. Beltzung, *27*
P. Born, *3*, *28*, **29**, **30**
A. Börngen, *6*
D. Bräuer, **2**
R. Busch, *15*, *16*
J. Carmona-Reyes, *36*
L. Couedel, *48*
A. Cowley, *27*
C.-R. Du, *37*, *42*
J. Eckert, *18*
L. F. Elizondo Aguilera, **55**, **56**
M. Engelhardt, *2*, *4*
Z. Evenson, *12*, *13*
P. Fopp, **24**
V. E. Fortov, *37*, *42*, *43*
F. Frahsa, *31*
S. P. Friedburg, *6*
M. Fuchs, *31*
J. Gao, *19*
C. George, *6*
A.L. Greer, *18*
J. Haeberle, **28**
T. Hagl, *5*, *6*, *43*
W. Hembree, *15*, *16*
D. M. Herlach, *50*
D. Heuskin, *2*, *14*
D. Holland-Moritz, **12**, *13*
K. Holldack, *30*
W. Hornfeck, *24*
P. Huber, *6*, *43*
T. W. Hyde, *36*
B. Ignatzi, *14*
A. V. Ivlev, **34**, *37*
I. Jonas, *15*, **16**
F. Kargl, *14*, *22*, *23*, *24*
C. Karrasch, *19*, *20*
R. Kessler, **3**
S. A. Khrapak, *39*, **45**, **46**, **47**, **48**
B. Klumov, *45*, *48*
C. A. Knapek, **6**
R. Kobold, **18**, *24*
M. Kolbe, *22*, *23*, *24*, **25**, *27*
R. Kompaneets, *34*
K. Kosiba, *18*
H. Kou, *25*
W. T. Kranz, **31**, **32**
C. Kreischer, *19*, **20**, **21**
M. Kretschmer, *5*
N. Kryuchkov, *46*
U. Kühn, *18*
M. Lammel, *4*
I. Laut, *35*, **41**
J. Li, *25*
A. Liluashvili, **52**
A.M. Lipaev, *5*, *37*, *42*, *43*
G. Lohöfer, *2*, **11**
O. Lopez, *31*
W. Löser, *19*
C. Lozano, *3*
A. Meurisse, **27**
A. Meyer, *9*, *12*, *13*, *14*, *15*, *16*
H. Meyer, *57*
J. K. Meyer, *7*, **35**
D. P. Mohr, *6*
V.M. Molotkov, *5*, *37*, *42*, *43*
G. E. Morfill, *41*
A. Müller, *37*
G.E. Murch, *14*
V. N. Naumkin, *43*
D. Neuhaus, **8**
V. Nosenko, *5*, **7**, *35*, **36**, **37**, *41*
B. Nowak, *12*, **13**
J. Ónody, **53**
S. Pauly, *18*
H. Peng, *50*
J. G. Prell, *6*
K. Prochnow, *2*
M. Y. Pustylnik, **5**, **40**
C. Räth, *41*, *44*
J. Reichert, **54**
M. Rubin-Zuzic, *43*
A. Schella, *28*
T. Schilling, *51*, *57*
J. Schmitz, *2*, *4*, *29*
S. Schneider, *2*, **4**
M. Schröter, *28*
M. Schwabe, **42**, **43**, **44**
S. Scudino, *18*
I. L. Semenov, **38**, **39**, *40*
O. Shuleshova, *19*
D. Simons, *19*
E. Sondermann, **14**
M. Sperl, *27*, *28*, *29*, *31*, *32*
J. Strohmenger, *19*
Y. Tan, *25*
M.H. Thoma, *5*
H. M. Thomas, *5*, *6*, *7*, *35*, *36*, *37*, *39*, *40*, *41*, *42*, *43*, *45*
A.V. Usachev, *5*
P. V. Vinogradov, *43*
Th. Voigtmann, *3*, *12*, **50**, **51**, *52*, *53*, *54*, *55*, *56*, **57**
T. Volkmann, **19**, *20*, *21*
J. Wang, *25*

M. Wegener, *2*, **22**
S.T. Wiese, *23*
F. Yang, *9*, *12*, *13*, **15**
L. Yang, *42*
S. Yurchenko, *46*
E. Zähringer, *6*, *40*, *43*
J. Zhang, *42*
S. K. Zhdanov, *7*, *35*, *36*, *41*, *42*, *43*, *44*
S. Zimmermann, **9**
A. Zippelius, *31*
A.V. Zobnin, *5*

DLR at a glance

DLR is the national aeronautics and space research centre of the Federal Republic of Germany. Its extensive research and development work in aeronautics, space, energy, transport and security is integrated into national and international cooperative ventures. In addition to its own research, as Germany's space agency, DLR has been given responsibility by the federal government for the planning and implementation of the German space programme. DLR is also the umbrella organisation for the nation's largest project management agency.

DLR has approximately 8000 employees at 20 locations in Germany: Cologne (headquarters), Augsburg, Berlin, Bonn, Braunschweig, Bremen, Bremerhaven, Dresden, Goettingen, Hamburg, Jena, Juelich, Lampoldshausen, Neustrelitz, Oberpfaffenhofen, Oldenburg, Stade, Stuttgart, Trauen, and Weilheim. DLR also has offices in Brussels, Paris, Tokyo and Washington D.C.

Institute of Materials Physics in Space

Research at DLR's Institute of Materials Physics in Space is devoted to the exploration of the fundamental mechanisms that underly liquid properties and solidification processes. Through the absence of gravitationally driven phenomena, like convection and sedimentation, investigations in weightlessness provide well-defined experimental conditions. This enables accurate measurements that allow for a benchmarking of simulation and theory, as well as a parametrization and a further development of earth-bound experiments. Embedded in a closely associated and strong ground based program with simulation, theory and experiments, the institute's research in space comprises key experiments towards an understanding of the physical mechanisms involved. This in turn forms the basis for a quantitative description of solidification processes and a computer assisted materials design from the melt.

DLR **Deutsches Zentrum**
für Luft- und Raumfahrt e.V.
in der Helmholtz-Gemeinschaft

Institut für Materialphysik im Weltraum
51170 Köln

www.dlr.de/mp
e-mail: materialphysik@dlr.de